Physik-Department der
Technischen Universität München
Lehrstuhl für Experimentalphysik 4

The interplay of structure and microscopic dynamics in oxidic melts observed by means of inelastic neutron scattering

Florian Kargl

Vollständiger Abdruck der von der Fakultät für Physik der Technischen Universität München zur Erlangung des akademischen Grades eines

Doktors der Naturwissenschaften (Dr. rer. nat.)

genehmigten Dissertation.

Vorsitzender: Univ.-Prof. Dr. R. Netz

Prüfer der Dissertation:

1. Univ.-Prof. (komm. L.) Dr. A. Meyer
2. Univ.-Prof. Dr. P. Böni

Die Dissertation wurde am 29.11.2005 bei der Technischen Universität München eingereicht und durch die Fakultät für Physik am 11.1.2006 angenommen.

Contents

Zusammenfassung

Das Ziel dieser Arbeit ist, in oxidischen Schmelzen eine mikroskopische Erklärung für Massentransportgrößen und Relaxationsprozesse und deren Verbindung zur Struktur auf atomaren Längenskalen aufzuzeigen. Um diesen Zusammenhang zu verstehen, wird eine Reihe von Schmelzen bei Temperaturen bis zu 1600 K mittels inelastischer Neutronenstreuung untersucht. Alle untersuchten Systeme zeigen ein nichttriviales Verhalten der Viskosität mit der Zusammensetzung. Die Systeme gehören zur Klasse der schnellen Ionenleiter. Bis in die Schmelze ist die Ionendiffusion vom Massentransport entkoppelt. Das beobachtete Verhalten wird mittels inelastischer Neutronenstreuung, welche sowohl Zugang zur Struktur, als auch der Dynamik auf interatomaren Längenskalen im Bereich von Piko- bis Nanosekunden bietet, grundlegend erklärt.

In der vorliegenden Arbeit werden alkaliionenleitende Systeme auf SiO_2 Basis in Abhängigkeit von der Alkalikonzentration und für verschiedene Alkaliatome untersucht. Makroskopische Messungen der Viskosität zeigen, dass diese bei Zugabe von geringen Mengen an Alkalioxid zu reinem SiO_2 um Größenordnungen einbricht und bei weiterer Zugabe nur schwach abnimmt. In allen untersuchten Schmelzen ist die Alkaliionendiffusion um Größenordnungen vom Massentransport entkoppelt. Die Ergebnisse der Neutronenstreuung an binären Alkali- und ternären Mischalkalischmelzen bieten eine modellfreie Erklärung für das nichtlineare Verhalten der Viskosität mit der Zusammensetzung und die schnelle Ionendiffusion. Die Alkaliatome sind inhomogen im SiO_2 Netzwerk verteilt. Bei Zugabe von Alkalioxid zu SiO_2 bilden sich Perkolationskanäle aus, die in der statischen Struktur eingefroren sind. Die inhomogene Verteilung der Alkaliatome in Kanälen manifestiert sich zum einen in einem Prepeak im Strukturfaktor, der Abständen auf Längenskalen von 6 Å bis 8 Å entspricht: Die Messungen zeigen, dass die Position dieses Prepeaks unabhängig von der Alkalikonzentration ist. Wie sich aus einem Vergleich von Li, Na und K haltigen Schmelzen zeigt, variiert die Position jedoch mit der Größe der Alkaliatome. Wie erwartet ändert sich in den Mischalkalisystemen die Höhe und Position des Prepeaks kontinuierlich mit der Zusammensetzung zwischen den binären Äquivalenten gleicher totaler Alkalikonzentration. Zum anderen kann der in der Dichtekorrelationsfunktion auf einer zehn Pikosekundenzeitskala beobachtete strukturelle Relaxationsprozess eindeutig und ausschließlich der Selbstdiffusion der Alkaliatome zugeordnet werden. Die Umordnung der Kanäle und folglich der Zerfall der Korrelationen zwischen verschiedenen Alkaliatomen erfolgt dagegen auf der Zeitskala der Netzwerkbewegung.

Die Viskosität in einer binären Alkalisilikatschmelze hängt nur schwach von der SiO_2 Konzentration ab. Dagegen führt die Zugabe einer zweiten netzwerkbildenden Komponente Al_2O_3 zu einer binären Alkalisilikatschmelze zu einem starken Anstieg der Viskosität. Die Viskosität ist in Systemen, die gleiche Mengen an Al_2O_3 und Na_2O enthalten, um bis zu acht Größenordnungen höher als in der vergleichbaren binären Alkalisilikatschmelze. Allgemein gilt als verstanden, dass Al tetraedrische Koordination aufweist, also auf zu Si äquivalenten Plätzen gebunden ist und somit das SiO_2 Netzwerk repolymerisiert. Aus Ladungserhaltungsgründen sollte es dann zu einer Bindung von Na an Al kommen. Die Neutronenstreudaten zeigen, dass die Zugabe von Al_2O_3 zu einer Störung der Kanalstruk-

tur führt. Die Diffusion der Na Atome wird abhängig von der Al Konzentration um bis zu eine Größenordnung langsamer. In Übereinstimmung mit der Erklärung für die Zunahme der Viskosität nimmt der Prepeak im elastischen Strukturfaktor mit zunehmender Al_2O_3 Konzentration ab.

Um Zugang zum partiellen Strukturfaktor der Atome eines zweiten Netzwerkbildners zu erhalten, werden Neutronenstreuexperimente an eisenhaltigen Natriumsilikaten durchgeführt. Die Zugabe von Fe_2O_3 zu einer binären Natriumsilikatschmelze führt zu einer Zunahme der Viskosität um bis zu zwei Größenordnungen für gleiche Anteile von Na_2O und Fe_2O_3. Die Zunahme ist damit schwächer ausgeprägt als in den Aluminosilikatschmelzen. Es werden Eisensilikate mit geringer und hoher Eisenkonzentration untersucht. In den Eisensilikaten trägt eine stark ausgeprägte diffuse magnetische Komponente zum Streugesetz $S(q, \omega)$ bei, die durch die an Fe^{3+} lokalisierten fluktuierenden Elektronenspins verursacht wird. Unterhalb von 20 K bilden sich aufgrund von Spin-Spin Korrelationen Maxima im Strukturfaktor der Natriumeisensilikate aus. Es werden partielle Fe-Fe Strukturfaktoren durch Differenzbildung der mittels der Flugzeitmethode gemessenen elastischen Strukturfaktoren gewonnen. Die Richtigkeit der Analyse wird durch Messungen am Diffraktometer D7 des Instituts Laue-Langevin bestätigt. Hier kann mit Hilfe einer Polarisationsanalyse ausschließlich der magnetische Anteil an der Streuung abgeleitet werden. Der so ermittelte magnetische Strukturfaktor weist über einen weiten Fe Konzentrationsbereich einen Korrelationspeak an der Stelle des in binären Natriumsilikatschmelzen vorhandenen Prepeaks auf. Analog zum Prepeak in den binären Natriumsilikaten ist die Position dieses Peaks ebenfalls unabhängig von der Fe Konzentration. Das beobachtete Verhalten spiegelt die inhomogene Struktur von Perkolationskanälen für Na wieder.

Im zugänglichen Temperaturbereich sind die Viskositäten der untersuchten Silikatschmelzen größer als 10^2 Pa s. Um grundlegende Fragen zum Flüssig-Glas Übergang in Systemen mit entkoppelten Zeitskalen für die schnelle Na Ionendiffusion und die strukturelle Relaxation untersuchen zu können, wird SiO_2 durch B_2O_3 ersetzt. Viskositäten in Natriumboratschmelzen sind bereits bei 1100 K im Bereich von 10 Pa s. Bei Viskositäten im Bereich um die 10^2 Pa s wird typischerweise der von der Modenkopplungstheorie vorhergesagte Flüssig-Glas Übergang erwartet. In den mittels inelastischer Neutronenstreuung untersuchten binären Natriumboratschmelzen wird ein schneller Relaxationsprozess beobachtet. Dieser schnelle Relaxationsprozess kann konsistent mit dem universellen β Skalengesetz der Modenkopplungstheorie beschrieben werden. Die Zeitskala der β Relaxation und die Linienform ist unabhängig vom Impulsübertrag q. Das Plateau, welches den Übergang von struktureller zu schneller β Relaxation markiert, spiegelt den elastischen Strukturfaktor wieder. Die Amplitude der Relaxation weist eine ausgeprägte q Abhängigkeit auf, die ebenfalls den Strukturfaktor folgt. Die Quadrate der Amplituden der schnellen Relaxation gehorchen für ein festes q dem im Rahmen der Modenkopplungstheorie erwarteten Skalengesetz. Sie extrapolieren für verschiedene q zu derselben kritischen Temperatur T_c, welche den Flüssig-Glas Übergang markiert. Aus dem dargestellten Verhalten der Fitparameter mit q und T wird geschlossen, dass der beobachtete schnelle β Relaxationsprozess die schnelle Na Diffusion vorbereitet. Darüberhinaus findet sich in Natriumboratschmelzen kein Anzeichen für einen Prepeak im Strukturfaktor.

Summary

The work presented here was devoted to elucidate the interplay of microscopic dynamics and structure in oxidic melts up to 1600 K. Moreover, an explanation for mass transport properties and the origin of fast ion conduction shall be provided. In these melts macroscopic properties such as viscosity are largely divergent as it is their structure depending on temperature and composition. Fast ion diffusion is decoupled of mass transport up to the melt. Inelastic neutron scattering that allows to investigate the mutual interplay of structure and dynamics on inter-atomic lengthscales and in the range of picosecond to nanoseconds provides an explanation for this behaviour.

Fast alkali ion conductors based on SiO_2 are discussed comprising different amounts of alkali oxide and alkali oxide species. A drop in viscosity by several orders of magnitude is observed upon adding only minor amounts of alkali oxide to pure SiO_2. On further addition of alkali oxide the viscosity only weakly decreases. All investigated silicate melts exhibit by orders of magnitude decoupled timescales of mass transport and alkali ion diffusion. The inelastic neutron scattering results on binary and mixed alkali silicates explain model independently the viscosity concentration dependence and the fast ion diffusion. In the binary alkali silicate systems experimental evidence is provided for an inhomogeneous distribution of alkali ions in a network of percolation channels embedded in the static structure. A prepeak in the structure factor that reflects typical distances of channels of 6 Å to 8 Å is one signature of this inhomogeneous distribution. The position of the prepeak is independent of the alkali concentration. Its position only varies with the size of the modifier atoms. The latter is shown by comparison of Li, Na and K silicates. In mixed alkali systems the prepeak position and height continuously changes with concentration between the binary counterparts of similar alkali content. Moreover, the relaxation process observed in the density correlation function on a ten picosecond timescale is uniquely attributed to the self diffusion of the alkali ions. Channel reformation and thus alkali-alkali relaxation only takes place on the timescales of the network relaxation.

The viscosity in a binary sodium silicate melt only weakly depends on the SiO_2 concentration. In contrast to this behaviour adding a second network former such as Al_2O_3 to a binary alkali silicate melt drastically increases the viscosity. In systems comprising equal amounts of Na_2O and Al_2O_3 viscosity is higher by about eight orders of magnitude compared to the binary equivalent. It is well accepted, that aluminum is bound in tetrahedral coordination. It occupies places equivalent to Si, consequently it repolymerises the network. Aluminum in tetrahedral coordination is supposed to be charge balanced by Na. The neutron scattering investigations on ternary aluminosilicate melts reveals a disruption of the network of percolation channels. Na diffusion slows down by up to an order of magnitude depending on the total Al_2O_3 concentration. Supporting the explanation of the increase in viscosity the prepeak in the structure factor decreases upon raising the Al_2O_3 content.

Neutron scattering experiments performed on iron bearing sodium silicate glasses provide access to the partial Fe structure factor. Fe is also regarded as a network former.

Adding Fe_2O_3 to a binary sodium silicate melt leads to an increase in viscosity by up to two orders of magnitude in a melt containing equal amounts of Na_2O and Fe_2O_3. The increase in viscosity is less pronounced compared to the corresponding aluminosilicate melt. Iron bearing silicate glass of low and of high Fe_2O_3 content are subject of the experiments. The scattering law reveals a strong diffuse magnetic contribution. Fluctuating electron spins localised on Fe^{3+} yield this diffuse component. Below 20 K spin-spin correlations are reflected by maxima and minima in the structure factor. A partial Fe-Fe structure factor was derived by means of subtraction of two elastic structure factors obtained by time-of-flight spectroscopy for two different temperatures. The validity of this approach in analysing experimental data was proven by means of polarised neutron diffraction on D7 at the Institut Laue-Langevin. Only the magnetic scattering contribution was yielded by means of polarisation analysis. In the Fe-Fe structure factor a peak is observed at the position of the prepeak in the binary sodium silicate melts. Only the height but not the position of the peak is changed by varying the Fe concentration. The observed behaviour reflects the inhomogeneous structure of percolation channel for Na diffusion.

The viscosities of the investigated alkali silicate melts are in the accessible temperature range larger than 10^2 Pa s. The point of liquid to glass transition predicted by the mode coupling theory of the liquid to glass transition is typically observed for viscosities close around this value. In order to investigate the liquid to glass transition in systems that exhibit decoupled timescales of ion diffusion and structural relaxation SiO_2 is replaced for B_2O_3. The viscosity in sodium borates at a temperature of 1100 K is of the order of 10 Pa s. The inelastic neutron scattering investigations feature a fast relaxation process in the density correlation function. It can be consistently described by the universal β scaling functions of the mode coupling theory. The timescale and the lineshape of this fast β relaxation is independent the momentum transfer q. The Plateau reflecting the transition of the β to the structural relaxation is proportional to the elastic structure factor. The relaxation amplitude features a pronounced q dependence that also reflects the structure factor. The squared amplitudes obey the expected scaling behaviour with temperature T at fixed q. Independently of the particular q value the squared amplitudes extrapolate to the same critical temperature T_c that marks the point of liquid to glass transition. The observed q and T dependence of the fit parameter provide evidence that the Na diffusion is prepared by this fast β relaxation process. Moreover, no prepeak is observed in the elastic structure factor of sodium borate melts.

Chapter 1

Introduction

Besides their use for technical applications, silica based liquids, glasses and rocks are of great relevance for geological processes. These compounds are the second most abundant type of material occurring in nature. Using silica based materials in their glassy state is rather wide spread. In earlier times mostly used as jewellery or for vases, glasses were undergoing a great progress and are nowadays part of sophisticated technological applications. Among those are glass fiber guides, sensors or fuel cells.

Oxidic glasses and melts belong to the macroscopically most intensively investigated class of materials. A summary of a huge number of research works on binary silica based and non silica based liquids and glasses is given in [MaSS83, MaSS85]. Similar work exists on ternary and multicomponent glasses and melts. Furthermore, over the years numerous investigations were performed on ion diffusion in oxidic glasses and melts with an overview provided in [ZhSv03]. However, already for the most basic compositions only comprising two components, the network forming oxide and a modifier, a microscopic explanation for macroscopic behaviour depending on temperature and composition is still missing.

The aim of this work is to provide answers to fundamental questions on the interplay of structure and dynamics in oxidic glass formers. The investigations of binary and ternary silicate melts provide an explanation for the dependence of viscosity on concentration and the decoupling of ion diffusion and mass transport. Moreover, the liquid to glass transition is investigated in melts that feature decoupled timescales of structural relaxation.

1.1 Glass transition scenario

Much interest was drawn to the investigation of the glass transition in the early eighties. At that time the field of investigation of glass forming systems had been already declined in scientific interest. The upcoming of the mode coupling theory [BeGS84, Got91, Got92] provided new input from an academic point of view. This theory offering detailed predictions on the glass transition scenario based on microscopic quantities triggered numerous experiments that aimed to show a proof contradicting this theory [Got99].

In the early stages the investigations were restricted to systems featuring rather uncomplex transport properties despite their complex structure. Representatives of these materials are e. g. the molecular glass former orthoterphenyl [Tol01] and glycerol [WuHL94, WuPC95, WuCR96] that only feature one process of structural relaxation. For the in-

vestigation of the relaxation dynamics various experimental methods such as dielectric spectroscopy, light scattering and inelastic neutron scattering were applied.

From the beginning theoretical approaches were made to systems featuring different structural relaxation times for different components [BoTa87]. Interest was directed to find a description of the freezing of fluid particles in an arrested matrix. Theoretical work was mostly based on model systems comprising e. g. hard spheres or dumbbell molecules building the liquid component. One of the most recent theoretical approaches provided a phase diagram for a fluid consisting of hard spheres confined in a porous medium [Kra05]. The latter features certain similarities to hydrogen in a porous glassy matrix or to ion conducting glasses and melts. The authors claimed to be able to show that the dynamics that underlies the fluid particles on approaching the liquid to glass transition follows the scaling laws of the mode coupling theory.

An experimental proof of the validity of such models in systems featuring different timescales of structural relaxation is still missing. Oxidic melts being subject of this thesis feature decoupled timescales for ion and network transport as evidenced by macroscopic measurements. Owing to their excellent undercooling capabilities they serve as model system. In the SiO_2- as well as in the B_2O_3-based melts the microscopic origin of this decoupling has not yet been unambiguously explained. The present thesis will provide an answer for the alkali silicates that are discussed in detail in the following paragraph. Due to the overall higher viscosity at experimentally accessible temperatures characteristic features of the liquid to glass transition in the density correlation function cannot be experimentally studied in silicate melts.

We thus directed our focus answering this particular question to sodium borates that feature viscosities in the range of a few to several hundred Pa s at temperatures close above 1000 K. The sodium borates are shown to feature a mode coupling scenario upon supercooling. The experiments show that in these melts the structural relaxation of Na is prepared by a fast β relaxation process.

1.2 Silicate melts

Addition of a small amount of network modifying alkali atoms to SiO_2 results in a drop in viscosity for a given temperature by up to 15 orders of magnitude [MaSS83, KnDS94]. The viscosity is fairly insensitive to changes in the composition of these binary melts. It varies only within two orders of magnitude over a large alkali concentration range that is almost negligible compared to its strong decrease. Moreover, the transport of the network modifying alkali ions deep in the melt is still decoupled of the mass transport of the network forming component. Early models proposing a random distribution of the alkali atoms in the rather rigid Si-O matrix failed in describing the viscosity and transport behaviour [WaBi38, Zac31].

Simulation work was started on alkali silicates by Angell and coworkers [AnCT82]. They proposed the existence of diffusion pathways for the alkali ions. First experimental work following this approach was done by Greaves using EXAFS [Gre85]. The method is only sensitive to the short range environment of certain atoms. Consequently, modelling of the structure becomes inevitable.

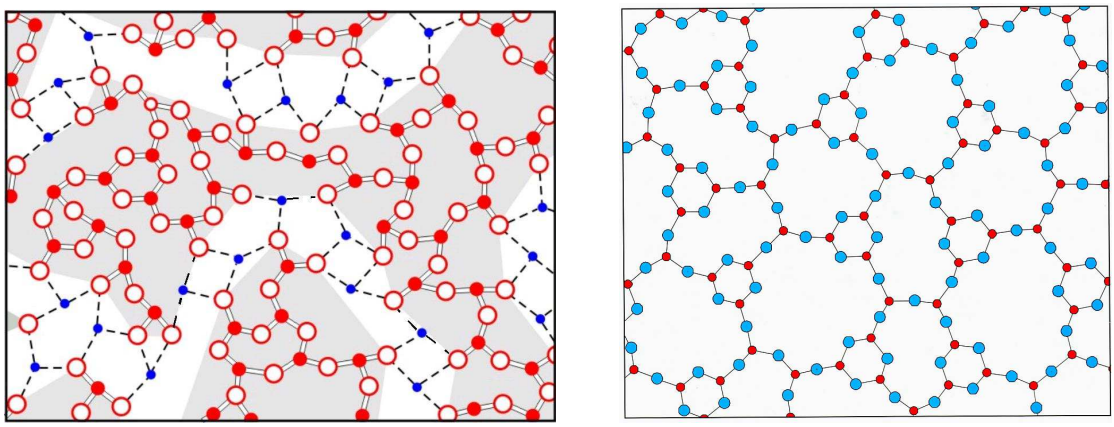

Figure 1.1: Models of oxidic melt structure. Left figure: Diffusion pathways for Na (blue) in the SiO matrix (red and white) are shown. The figure was provided by Greaves [Gre85]. Right figure: Schematic representation of the structure of pure boron oxide (red and blue, respectively) taken from [WrFH96]. It is composed of randomly oriented boroxol rings.

Increasing computer power opened up new possibilities for molecular dynamics (MD) simulation work. Especially the rather time consuming first principle approach has become possible for developing accurate potentials for their later use in molecular dynamics simulations. A detailed work on sodium silicates has been started by Horbach and Kob [HoKo99]. The work is based on a modified version of the potential presented in [vBKS90]. An adapted version of this potential has already been used in an earlier approach [OvSa98]. The simulation work provided evidence for a network of channels for fast alkali ion conduction that manifests itself in a prepeak in the structure factor below the first sharp diffraction peak of pure silica [HoKB02, HoKo99].

Typical timescales for relaxation process in these melts are in the picosecond to nanosecond range. Inelastic neutron scattering and molecular dynamics simulations provide access to these timescales. Both methods allow for space dependent investigation of the density correlation function on inter-atomic lengthscales. Thus the inelastic neutron scattering experiments performed in this thesis work can be compared to MD simulation data.

A prepeak was already reported by an inelastic neutron scattering experiment performed in our group on a sodium disilicate melt [MeDS02]. The prepeak was shown to emerge only in the melt with increasing temperature. The simulations found a qualitatively similar temperature dependence, but they did not provide a quantitative description. The neutron scattering work being subject of this thesis triggered MD simulation work on Na trisilicate that was performed in contrast to earlier studies at constant pressure and experimental densities [MeHK04]. Such a MD simulation even quantitatively reproduced the elastic structure factors found in our experiments. A snapshot of the simulation box shown in figure 1.2 clearly exhibits a network of Na percolation channels with the Na atoms represented by the blue spheres.

In addition, the simulation reveals a strongly pronounced separation of the timescales of relaxation given by the decay of the coherent and incoherent correlators. The latter is

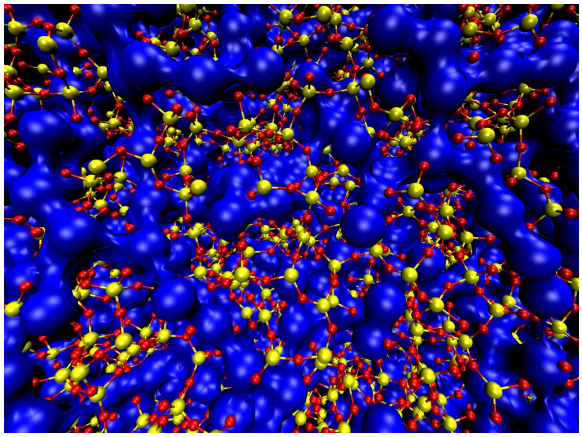

Figure 1.2: Snapshot of the simulation box of a molecular dynamics simulation performed by Horbach and coworkers on NS3 [MeHK04]. Na atoms are shown in blue with the size of the sphere reflecting the ionic radii. Depending on the distance different Na atoms are connected. The SiO network is represented in yellow and red, respectively. The size of the Si and O atoms is drawn smaller for clarity reasons. The covalent binding distance represented by the sticks is shown to the correct size.

shown in figure 1.3. The coherent Na correlator decays on the same timescale as the Si and O network correlators. The partial sodium structure factor $S_{NaNa}(q)$ is represented by the solid line. As expected the Na-Na relaxation times are in-phase with the structure factor.

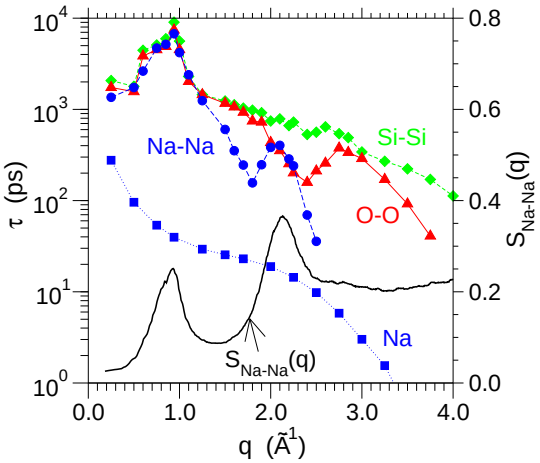

Figure 1.3: Overview of the relaxation times in sodium disilicate derived by means of MD simulation work for the different correlation functions [HoKB02]. The simulation was performed at 2100 K corresponding to $T_{exp} \simeq$ 1700 K. A strong decoupling of the relaxation time for the sodium self correlator and the coherent correlators is observed.

Such a decoupling of relaxation timescales is experimentally evidenced by our inelastic neutron scattering investigations for the alkali silicates that are subject of this thesis work. We show that the decoupling of timescales of self diffusion of the alkali ions of mass transport up to the melt is a general feature for alkali silicates.

Furthermore, the MD simulations on Na disilicate report a fast relaxation process that is according to the mode coupling theory a precursor of structural relaxation. Applying the universal scaling functions on the MD simulation data a critical temperature marking the point of liquid to glass transition was reported around 2100 K [HoKo02]. This is clearly above experimentally obtained temperatures.

Recently, an approach was started to perform a mode coupling theory calculation on silicate melts. The partial structure factors obtained by the MD simulation have been

used as input parameters for the theoretical work [VoHo05]. The authors were able to show that the decoupling of the decay of the self and pair correlators of the Na and the SiO matrix obtained by the MD simulation and experimentally proved in this thesis work can be qualitatively reproduced by the theory.

Furthermore ternary silicate melts comprising an additional network forming component were investigated. Our scientific interest was guided towards the ternary sodium aluminosilicates. Adding alumina to a binary sodium silicate melt leads to a decease in the viscosity by up to eight orders of magnitude in a melt comprising equal amounts of Na_2O and Al_2O_3 at fixed SiO_2 concentration. We provide evidence that addition of Al_2O_3 leads to a disruption of the channel network for fast alkali ion conduction. The fast alkali ion transport is hindered, what is evidenced by a decrease in the timescales of structural relaxation.

In literature attempts were always made to describe the dynamics of mobile ions in the framework of a unified model as shown e. g. in [FuRL98]. An overview of structural investigations on glasses and resulting models was presented in [Wri97]. The present work will demonstrate for boron oxide and silica based melts that not only the structure on atomic lengthscales is entirely different, but also their microscopic dynamics. Hence, a unified model will not be applicable.

1.3 Key questions in geoscience

A motivation why especially Al_2O_3 bearing melts are of interest is provided in the following paragraphs.

Silicate rock in its molten, glassy or crystalline state is the main ingredient in any geological process. Volcanic eruptions crucially depend on the composition of the magmatic melt. Small changes in melt composition can drastically increase or decrease the viscosity. Especially volatiles, e. g. water, carbon dioxide and sulfur, have a major impact on flow properties. For an overview on recent research in this field the interested reader is referred to results discussed in "Silicate Melt Workshops" [BoDR04, BoDR01] and to a recent review in mineralogy [StMD95]. To provide accurate modelling of geological processes physical parameters like the viscosity temperature or viscosity composition dependence are used as input parameters. A detailed knowledge of the microscopic origin of different relaxation processes and its relation to melt structure will thus allow to model e. g. volcanic processes with greater accuracy. It was shown in great detail that flow properties of magma determine whether a volcanic eruption is explosive or effusive [Din96].

The direct investigation of transport properties on a microscopic scale is not accessible in typical experiments performed so far. Inelastic neutron scattering provides a detailed answer on the interplay of structure and dynamics in these systems. A fundamental understanding of processes on microscopic time and lengthscales serves as necessary input for any simulation. Moreover, results on alkali silicate melts serve as basis for investigations on water bearing silicate glasses. First neutron scattering measurements as well as

simulations on these systems were performed in our group [Mul03, Poh05].

In geosciences the main focus is directed to be able to predict macroscopic behaviour of a multicomponent melt over a large temperature range by simply knowing its composition. A model achieving this task for a large number of Al_2O_3 and H_2O containing melts was presented in [HeDi96]. It is well suited for a rather restricted range of compositions and temperatures. It fails in predicting the compositional behaviour of the basic component of any natural occurring silicate melt as the binary alkali silicates. Sodium aluminosilicates subject to this thesis work are the most simple form of lava.

1.4 Outline of the present work

The present work comments on inelastic neutron scattering results obtained on binary and ternary silicate melts and boron oxide based melts. Chapter 2 explains the different steps of the sample preparation and characterisation. The theory relevant for the method of investigation and the analysis of the measured data is presented in chapter 3. Chapter 4 provides an overview of neutron scattering on oxidic melts. It briefly introduces the two scattering methods used for the investigation of oxidic melts and glasses. Relevant details of the setup and sample environment are noted. Finally, remarks on the reduction of the raw data are given. We start the discussion of the experimental results by presenting the boron oxide based melts in chapter 5. A central aspect is the analysis of relaxation processes in oxidic melts in the framework of the mode coupling theory. Chapter 6 presents the experimental work performed on the silica based samples. The first part is devoted to results on binary and mixed alkali silicate melts providing the background information to relaxation processes and structural information obtained by means of inelastic neutron scattering. The alkali atoms are shown to be inhomogeneously distributed in percolation channels embedded in the static structure. The last two sections discuss the investigation of two different ternary silicate melts and glasses. In the sodium aluminosilicates we focused on the impact of addition of Al_2O_3 on the channel structure. The investigations on Fe bearing silicate glasses was mainly guided by the possibility to investigate Fe-Fe correlations by means of magnetic neutron scattering. The partial Fe-Fe structure factors were obtained for systems comprising different total amounts of Fe_2O_3.

Chapter 2

Synthesis of oxidic glasses and melts

In the following sections the preparation and macroscopic characterisation of the investigated samples are discussed.

2.1 High temperature fusion

The samples were synthesized by high temperature fusion of reagent grade powders. We used for the synthesis of the silicates Na_2CO_3 (Merck 99.995%), K_2CO_3 (Merck 99.995%), SiO_2 (Alfa Aesar 99.995%), Al_2O_3 (Alfa Aesar 99.995%) and Fe_2O_3 (Alfa Aesar 99.99%) as precursor materials. In order to synthesize the ternary sodium aluminosilicate samples, fine SiO_2 and Al_2O_3 powder with comparable purity was used. For the latter amorphous SiO_2 and crystalline Al_2O_3 powder were milled in an agate mortar using ethanol as lubricant. Afterwards, the fine powder was dried and kept at 110 °C to prevent water absorption. Before the synthesis the milled powders were separately dried for one hour at 1000 °C. For the borate samples we used Na_2CO_3 (Merck 99.995%) and B_2O_3 (Alfa Aesar 99.99%) as precursor materials. The samples were used for light scattering experiments and as test material for the synthesis procedure. Neutron scattering investigations made use of enriched boronanhydrate $^{11}B_2O_3$ (Aldrich 99% ^{11}B enrichment). Not enriched boron oxide would contain 20% of the strong neutron absorber ^{10}B. For similar reasons we used a lithium disilicate sample enriched in ^{7}Li for the neutron scattering experiments. The latter sample was provided by Prof. Paul Heitjans, University of Hanover.

For the sample synthesis chemically inert Pt-cylinders were used to prevent the reaction between the melt and the container. We compared the weight of the raw materials and the synthesized sample materials after decarbonation and annealing. All samples were synthesized in the 10 g to 40 g sample material range. Thus, with the accuracy provided by the balance, uncertainties in the sample composition after annealing are in the per mille range. An accuracy in the per mille range is sufficient since no change in macroscopic parameters is observed for such a small change in composition.

Particular issues have to be considered during the process of synthesis of sodium aluminosilicate samples. They were synthesized in Pt-0.5%Au crucibles. On a Pt-Au surface wetting is reduced compared to a pure Pt surface. Thus the glass samples can easily be removed. Homogenisation of the Al_2O_3 containing samples was achieved by

stirring them under air for more than 24 h at 1450 °C. Synthesis of Al_2O_3 rich samples is a difficult issue due to their still rather high viscosity at the maximal temperatures of synthesis of 1450 °C. Na evaporation for these highly viscous melts cannot be excluded during the process of synthesis. Thus appropriate additional amounts of Na_2CO_3 have to be added prior to the synthesis. Macroscopic properties of these melts in the concentration range, where the ratio Na_2O/Al_2O_3 is larger than unity, depend strongly on the exact composition. Our aim was also to extend the analysis to the Al_2O_3 rich side. However, synthesis according to the method described above failed for samples containing more than 20 mol% Al_2O_3 on an absolute scale. Dissolution of Al_2O_3 is too slow at reasonable temperatures due to interdiffusion of alkali ions on the surface.

Name	Composition	T of synth. [°C]	Instrument
LS2	$^7Li_2O\,2\,SiO_2$	1350	IN6
NS1.5	$Na_2O\,1.5\,SiO_2$	1250	IN6
NS2	$Na_2O\,2\,SiO_2$	1250	IN5
NS3	$Na_2O\,3\,SiO_2$	1300	IN6
NS4	$Na_2O\,4\,SiO_2$	1325	IN6
KS2	$K_2O\,2\,SiO_2$	1300	IN6
KS3	$K_2O\,3\,SiO_2$	1300	IN6
NKS4	$Na_2O\,K_2O\,4\,SiO_2$	1250	IN6
NKS6	$Na_2O\,K_2O\,6\,SiO_2$	1250	IN6
NAS4	$Na_2O\,Al_2O_3\,4\,SiO_2$	1400	IN6
NAS6	$Na_2O\,Al_2O_3\,6\,SiO_2$	1450	IN6
N3AS8	$3\,Na_2O\,Al_2O_3\,8\,SiO_2$	1450	IN6
N3AS12	$3\,Na_2O\,Al_2O_3\,12\,SiO_2$	1450	IN6
N2FS6	$2\,Na_2O\,Fe_2O_3\,6\,SiO_2$	1100 - 1250	IN6, D7
N5FS12	$5\,Na_2O\,Fe_2O_3\,12\,SiO_2$	1100 - 1250	IN6

Table 2.1: Sample abbreviation for silica based melts, composition, synthesis temperature and neutron scattering instruments the samples were measured on. The measurements on silica based glasses and melts subject of analysis in this thesis work were exclusively performed at ILL. A list of the different instrumental setups used for the experiments can be found in appendix B.

In the binary compositions self diffusion of the alkali components is fast enough at 1200 °C to 1400 °C in the melt to obtain bubble free and homogeneous melts by simply annealing the samples for 12 hours. Potassium silicate samples are strongly hygroscopic. Fine powder as it is was used for filling the sample holders of neutron scattering experiments can only be prepared directly before filling. Only small amounts can be filled to the sample container during each step to allow for water removal during heating.

The iron bearing sodium silicate samples were synthesised via mixing the appropriate milled binary sodium silicate glass with Fe_2O_3. Synthesis of Fe bearing melts in a Pt container leads to diffusion of Fe in the container. Thus before synthesising the sample used for the experiments the Pt cylinder was preloaded with iron. $2\,Na_2O - Fe_2O_3 - 6\,SiO_2$ and $5\,Na_2O - Fe_2O_3 - 12\,SiO_2$ were synthesised at 1250 °C and at 1100 °C, respectively. The iron rich sample was annealed for 12 h at the temperature of synthesis. The sample

containing less iron was annealed for 16 h at 1250 °C.

Table 2.1 gives an overview of the temperatures of synthesis for the different silica based compositions and the corresponding neutron scattering instruments used for the experiments.

Sodium borate glasses were synthesized at temperatures below 1000 °C. The viscosity in these materials is substantially lower compared to sodium silicates at similar temperatures. In sodium containing borate glasses a substantial loss of Na was observed at temperatures exceeding 1000 °C. Homogeneous and dry glasses were obtained by annealing the samples for 6 hours at 950 °C. Before mixing the Na_2CO_3 and the B_2O_3 powders, B_2O_3 was dehydrated at 1020 °C for 12 hours. The obtained glass was crushed to fine powder, in order to fill a sample holder. The compositions of sodium borate glasses synthesized during this thesis work are listed in Table 2.2.

Name	Composition	T of synth. [°C]	Instrument
11B2O3	$^{11}B_2O_3$	1000	HFBS (NIST)
NB2	$Na_2O\,2\,^{11}B_2O_3$	900	HFBS (NIST), IN6 (ILL), IN5 (ILL)
NB4	$Na_2O\,4\,^{11}B_2O_3$	950	HFBS (NIST), DCS (NIST)

Table 2.2: Sample abbreviation for boron oxide based melts, composition and neutron scattering instruments the samples were measured on. A list of the different instrumental setups used for the experiments can be found in appendix B.

The synthesized melts were poured on a stainless steel plate. We obtained transparent and homogeneous glasses. Only NAS6 and N2FS6 were quenched in the Pt cylinder. The viscosity in the latter two samples was at reasonable temperatures too high to allow for enough flow. In lithium disilicate, despite of being fully transparent, the cooling rate was too small, in order to obtain a completely amorphous sample. The LS2 glass features small Bragg peaks in addition to the smooth liquid-like structure factor. This indicates partial crystallinity of the sample or a phase separation as it is reported for lithium silicate glasses [MaMK91].

For the high temperature neutron scattering experiments the samples were contained in hollow cylinders providing an annular sample geometry. The annular Pt cylinders were filled in steps with powder. A typical amount of 0.2 g to 0.5 g was filled for each step. The cylinder was reheated between each filling step to the synthesis temperature and kept for about 15 minutes at this temperature. As soon as half of the sample height was reached the sample was annealed between 2 and 4 hours. After the final height had been reached, the sample cylinder was kept for 12 h at the synthesis temperature. After annealing the cylinder was quenched on air to room temperature. The main aim of the slow filling procedure was to remove air bubbles from the melt. Moreover, only 65% of the total height of the container was filled by sample material owing to its temperature dependent density. A decrease in the sample density of up to 20% compared to room temperature together with the low compressibility as well as the existence of air bubbles may result in the breaking of a gas tight sealed container during heating.

Iron bearing silicate glasses were also studied at low temperatures using a standard ILL orange cryostat. For this purpose glass disks were prepared in a Pt-0.5%Au mould. The latter is shown in figure 2.1.

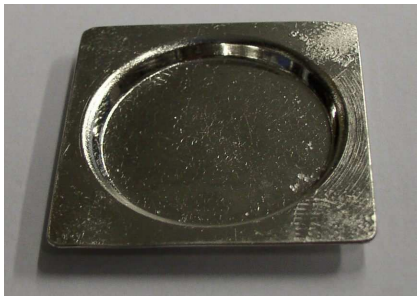

Figure 2.1: Pt-0.5%Au mould used for the preparation of glass disks with 33 mm diameter and a thickness of up to 2 mm. The surface is polished prior to the sample preparation.

2.2 Sample characterisation

The synthesized samples were characterised by means of differential scanning calorimetry. For the determination of the glass transition temperatures a STA1500 (Rheometric Scientific) was used. The STA was calibrated prior to the experiments. Calibration included an empty furnace measurement, an empty can measurement, a measurement of sapphire as reference and the measurement of melt standards for temperature calibration. A typical heat flow curve as obtained from the measurements on a glass sample is shown in Fig. 2.2.

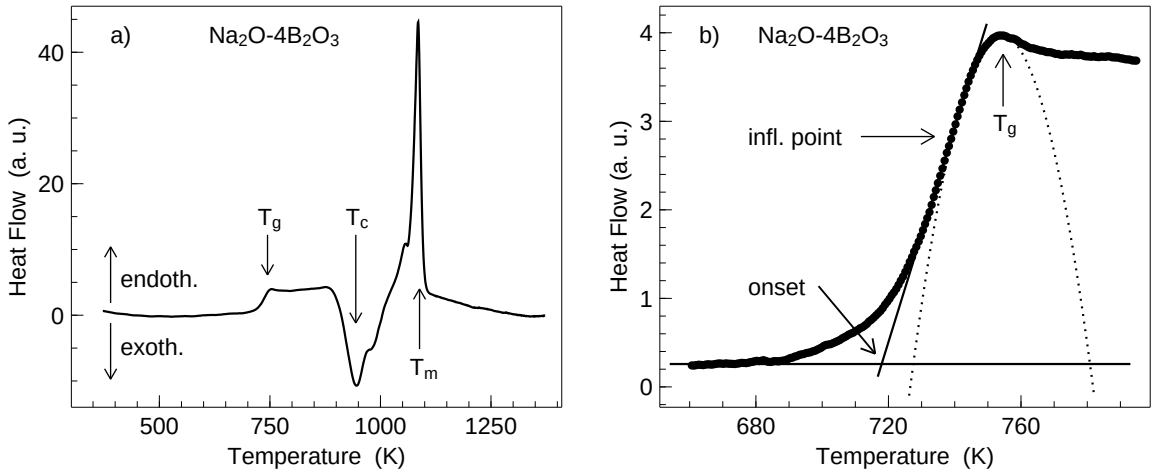

Figure 2.2: Heat flow curve for NB4 obtained by differential scanning calorimetry (DSC) measurements. The experiment was performed under constant He gas flow. The heating rate is 20 K/min. A baseline is subtracted. a) The glass transition temperature T_g, the temperature of crystallisation T_K and the melting temperature T_m are indicated by corresponding arrows. b) Enlarged heat flow curve close around the calorimetric glass transition. Calorimetric glass transition temperatures as obtained from the different methods described in the text are indicated by arrows. Data presented in table 2.3 was obtained by fitting of a parabola to the peak maximum (dashed line).

The calorimetric glass transition temperature is characterised by an excess heat flow into the sample. Endothermic processes lead to positive heat flow. The calorimetric glass transition temperatures T_g depend on the heating rate owing to the fact that the calorimetric glass transition is a dynamical transition and not a conventional first or second order transition. Moreover, T_g depends on the procedure of data analysis. Three different possibilities are accepted to determine T_g. The glass transition temperature can be taken from the onset, as the inflection point or as the maximum of the excess signal in the heat flow curve. Depending on which method is used a variation of T_g up to 40 K is achieved. A comparison with literature data presented in [Kar02] has shown that most of the literature data are taken from the onset of the excess heat flow. In this study the glass transition temperature is obtained by determining the maximum of the excess heat flow. Taking this offset into account the measured glass transition temperatures were compared with literature values.

The glass transition temperatures obtained for the synthesized glasses by means of the peak method are shown in table 2.3. The determined glass transition temperatures for the binary silicate samples as well as for the sodium borates correspond to data presented in literature [MaSS83, MaSS85].

In two of the sodium aluminosilicate glasses no glass transition temperature was determined by our experiments. The excess heat flow in these samples is too small to be experimentally resolved. Glass transition temperatures for those melts can be measured by using a micropenetration apparatus. Using such an experimental setup the viscosity can be determined as presented in literature [RoPM01, Web05]. Based on these experiments the calorimetric glass transition temperature is determined as the point at which the viscosity reaches 10^{12} Pa s.

Sample	T_g [K]	Sample	T_g [K]	Sample	T_g [K]	Sample	T_g [K]
NS1.5	730	KS2	802	NAS4	1142	N2FS6	791
NS2	768	KS3	841	NAS6	—	N5FS12	778
NS3	788	NKS4	738	N2AS3	900	$^{11}B_2O_3$	518
NS4	790	NKS6	735	N3AS8	—	NB2	748
LS2	773	NAS2	1133	N3AS12	853	NB4	753

Table 2.3: Glass transition temperatures T_g obtained by means of differential scanning calorimetry using a heating rate of 20 K/min. The temperatures were determined from the heat flow signal. The maximum of the excess in the heat flow was used to determine T_g. The error is of the order of about 2 K with respect to the accuracy of the temperature measurement.

For sodium aluminosilicates - as mentioned earlier - macroscopic properties depend strongly on the Al_2O_3 content. Thus a careful synthesis of the sample is necessary. The purity of the precursor material is a decisive parameter for the quality of all samples.

Besides the determination of the glass transition temperatures we performed annealing experiments. The main aim of these experiments was to probe the undercooling capabilities of the samples. For this purpose the temperature of crystallisation and melting are determined. Especially sodium borate glasses were carefully investigated since these

samples were subject to investigation in the undercooled liquid region. For a given temperature in the supercooled liquid region we determined the timespan one can keep a sample cooled from the equilibrium melt to this temperature before crystallisation sets in. The investigations show that undercooling by about one third of $T_m - T_K$ below T_m is reasonable for our experiments which is about 100 K below the liquidus. At this temperature the sample is stable of about one hour before crystallisation sets in. This is a reasonable value for any neutron scattering experiment. In order to remelt a partially or completely crystalline sample within a short period of time, a temperature of at least 100 °C above the liquidus shall be used.

Chapter 3

Theory

The first section of this chapter comprises a brief introduction to the basic theory of neutron scattering. The second part provides an overview of the central issues of the mode coupling theory of the liquid to glass transition based on the work of Götze and coworkers. Moreover, the universal scaling functions that allow to describe the density correlation function of a glass forming melt are presented. We provide a detailed explanation of the constraints implied by the theory to describe experimental data using this universal scaling functions as fit functions. Mode coupling theory is only applied to describe the data that is discussed in chapter 5. The last section is devoted to an overview of different models used for the interpretation of a decay in the density correlation function. The latter can be attributed to a structural relaxation or to diffusion of particles.

3.1 Neutron scattering

Besides basic formula for neutron scattering (see 3.1.1) correlation functions used to describe the dynamics of a many particle system are discussed (see 3.1.2). The relationship of the theoretical quantities to neutron scattering experiments is provided. Moreover, some general remarks on the investigations on liquids and amorphous systems by means of neutron scattering are presented in the last subsection.

3.1.1 Basic concepts

The double differential scattering cross section of a scattering process counts the number of particles scattered into a solid angle $d\Omega$ in an energy interval $[E, E + dE]$.

According to first order perturbation theory the partial double differential cross section is given by

$$\left(\frac{d^2\sigma}{d\Omega\, dE_f}\right)_{\lambda\to\lambda'} = \frac{k_f}{k_i}\ \left(\frac{m_N}{2\pi\hbar^2}\right)^2\ |\langle\vec{k}_f\lambda'|V|\vec{k}_i\lambda\rangle|^2\ \ \delta(E_\lambda - E_{\lambda'} + E_i - E_f)\,. \tag{3.1}$$

The matrix element $\langle\vec{k}_f\lambda|V|\lambda\vec{k}_i\rangle$ gives the probability to scatter a neutron in initial state $\vec{k}_i$ on a system of nuclei in state λ to its corresponding final states marked by $\vec{k}_f$ and λ'. The averaging is done over the states $\vec{k}_i$ and $\vec{k}_f$. The interaction between the neutron and

the system of nuclei is mediated by the potential V. Energy conservation is ensured by the δ function.

To evaluate (3.1) an appropriate description of the potential V has to be used. Starting from the calculation of the cross section for a single fixed nucleus the Fermi pseudopotential $V(\vec{x}_j) = 2\pi\hbar^2/m_N \cdot b_j\delta(\vec{x}_j)$ is derived. b_j denotes the scattering length for a single fixed nucleus and $\vec{x}_j$ the difference in the position of the neutron and the jth nucleus. The pseudopotential is of short range order compared to the wavelength of the scattered particle. This only holds true for nuclear scattering, whereas for magnetic scattering the potential is not short ranged but rather weak. Thus the Born approximation is also valid. However, for the latter type of scattering a form factor given by the electron shell has to be taken into account. The form factor leads to a decrease of the scattered intensity with increasing q. Substitution of the δ-function in (3.1) by its integral representation using $\hbar\omega = E_i - E_f$ for the energy transfer to the neutrons[1] yields

$$\left(\frac{d^2\sigma}{d\Omega\, dE_f}\right)_{\lambda\to\lambda'} = \frac{k_f}{k_i}\frac{1}{2\pi\hbar}\sum_{j\,j'} b_{j'}b_j \int_{-\infty}^{\infty} dt\, e^{-i\omega t}\langle\lambda|e^{-i\vec{q}\cdot\vec{R}_{j'}}|\lambda'\rangle\langle\lambda'|e^{iHt/\hbar}e^{i\vec{q}\cdot\vec{R}_j}e^{-iHt/\hbar}|\lambda\rangle \tag{3.2}$$

assuming that the scattering amplitudes b_j and $b_{j'}$ are real numbers. The exponential terms containing the energy changes of the system of the nuclei E_λ and $E_{\lambda'}$ were reformulated by using the relation $e^{iHt/\hbar}|\lambda\rangle = e^{iE_\lambda t/\hbar}|\lambda\rangle$. H is the Hamiltonian of the scattering system.

To obtain the double differential cross section a summation over the final and initial states λ and λ' has to be carried out. Using the closure relation for a pair of operators and the Heisenberg description of an operator given by $A(t) = e^{iHt/\hbar}Ae^{-iHt/\hbar}$ the double differential cross section reads

$$\frac{d^2\sigma}{d\Omega\, dE_f} = \frac{k_f}{k_i}\frac{1}{2\pi\hbar}\sum_{j\,j'} b_{j'}b_j \int_{-\infty}^{\infty} dt\, e^{-i\omega t}\sum_{\lambda} p_\lambda\langle\lambda|e^{-i\vec{q}\cdot\vec{R}_{j'}(0)}\; e^{i\vec{q}\cdot\vec{R}_j(t)}|\lambda\rangle\,. \tag{3.3}$$

Summation over the operators weighted by the statistical distribution of the states p_λ that is defined by a Boltzmann weighting factor represents the thermal or ensemble average over the states λ which may be denoted by $\langle e^{-i\vec{q}\cdot\vec{R}_{j'}(0)}e^{i\vec{q}\cdot\vec{R}_j(t)}\rangle$.

The scattering law $S(q,\omega)$ is defined via

$$S(\vec{q},\omega) = \frac{1}{2\pi\hbar}\int_{-\infty}^{\infty}\frac{1}{N}\sum_{j\,j'}\langle e^{-i\vec{q}\cdot\vec{R}_{j'}(0)}\, e^{i\vec{q}\cdot\vec{R}_j(t)}\rangle\, e^{-i\omega t}\mathrm{d}t\,. \tag{3.4}$$

Since the scattering law is an odd function, the process of neutron energy loss and of neutron energy gain are not equally probable. Therefore, it depends on temperature

$$S(q,-\omega) = e^{-\hbar\omega/k_BT}S(q,\omega)\,. \tag{3.5}$$

[1]The energy transfer of the neutron is presented according to its conventional definition. A positive sign denotes neutron energy loss, a negative sign neutron energy gain. During the discussion of the experimental data the sign convention is for convenience reasons contrarily used. We note that we discuss only the neutron energy gain side.

The latter equation is known as the principle of detailed balance. It is shown for an isotropic scatterer for which only the magnitude q of the vector $\vec{q}$ is relevant and not its orientation. Neutron energy gain is reduced by the exponential prefactor compared to neutron energy loss. The probability for the system of nuclei to be initially in the higher energy state is lowered by this prefactor compared to being initially in the lower energy state.

3.1.2 Correlation functions

In the following we define correlation functions and discuss their relation to the scattering law as it is measured in a neutron scattering experiment. Moreover, the relation of the autocorrelation function for a multi-particle system to the double differential cross section is presented. For a detailed description the reader is referred to van Hove [Hov54] and Squires [Squ96].

In general, a correlation function is defined as the ensemble average $\langle A\,|B\rangle$ over two operators A and B. We define the operators A and B as the deviation of the operator at a given time t from its equilibrium position $\langle A\rangle$. The autocorrelation of an operator yields $\langle A|A\rangle$.

The following discussion is restricted on the particle density operator $\rho(\vec{r},t)$ and its spatial Fourier transform $\rho(\vec{q},t)$. The autocorrelation function of these dynamical variables is discussed.

Van Hove introduced the particle density operator

$$\rho(\vec{r},t) = \sum_j \delta(\vec{r} - \vec{R}_j(t))\,, \tag{3.6}$$

where $\vec{r}$ defines the position of the neutron and $\vec{R}_j$ the position of the jth nucleus. The time-dependent pair distribution function $G(\vec{r},t)$ is obtained by

$$G(\vec{r},t) = \frac{1}{N}\int d\vec{r}\,'\,\langle\rho(\vec{r}\,',0)\rho(\vec{r}\,'+\vec{r},t)\rangle\,, \tag{3.7}$$

with N denoting the total number of nuclei. It represents the ensemble average of the density correlation function at time $t = 0$ and a time $t > 0$ different from zero.

The scattering law $S(\vec{q},\omega)$ that is directly proportional to the double differential cross section is the space and time Fourier transform of the pair distribution function $G(\vec{r},t)$ and reads

$$S(\vec{q},\omega) = \frac{1}{2\pi\hbar}\int d\vec{r}\,dt\; G(\vec{r},t)\,e^{-i\omega t}\,e^{i\vec{q}\cdot\vec{r}}\,. \tag{3.8}$$

It describes the frequency and momentum spectrum of the dynamical variable $G(\vec{r},t)$.

Owing to the autocorrelation function of the density operator the pair distribution function can be split into two parts. The first one ($G_s(\vec{r},t)$) correlates a particular particle which is at time zero at position $\vec{r}$ to its position $\vec{r}\,'$ at a time t different from zero yielding

$$G_s(\vec{r},t) = \frac{1}{N}\int d\vec{r}\,'\,\sum_j\langle\delta(\vec{r}\,' - R_j(0))\,\delta(\vec{r}\,'+\vec{r}-R_j(t))\rangle\,. \tag{3.9}$$

Consequently, the pair part of the correlation function ($G_p(\vec{r},t)$) would determine the probability to find a particle including the same particle at position $\vec{r}\,'$ at a later time t, if a particle was located at position $\vec{r}$ at time $t=0$, yielding

$$G_p(\vec{r},t) = \frac{1}{N}\int d\vec{r}\,' \sum_{j\,j'} \langle \delta(\vec{r}\,' - R'_j(0))\,\delta(\vec{r}\,' + \vec{r} - R_j(t))\rangle\,. \tag{3.10}$$

Space Fourier transformation of the pair correlation function $S(\vec{q},t) \propto \int d\vec{r}\; G(\vec{r},t)\, e^{i\vec{q}\cdot\vec{r}}$ or energy Fourier transformation of the scattering law $S(\vec{q},t) \propto \int d\omega\; S(\vec{q},\omega)\, e^{i\omega t}$ results in the intermediate scattering function $S(\vec{q},t)$. In the following chapters this function is referred to as density correlation function. For isotropic systems the vector $\vec{q}$ is replaced by its magnitude q. We define the normalized density correlation function by

$$\Phi(q,t) = \frac{\langle \rho^*(q,0)\rho(q,t)\rangle}{\langle \rho^*(q,0)\rho(q,0)\rangle}\,, \tag{3.11}$$

where the denominator is equivalent to the static structure factor $S(q) = \langle \rho_q^*(0)\rho_q(0)\rangle$. The density correlation function is normalized to unity for $t=0$ according to its definition. However, we have to point out that our discussions are based on the density correlation function $S(q,t)$ as it is obtained by a measurement. Thus it is not normalized to unity by means of the static structure factor. In a time-of-flight experiment using long wavelength neutrons no static structure factor can be obtained, since only part of the phonon spectrum is accessible in the dynamical range provided by the instrument. The density correlation function provides the momentum spectrum of the decay of the density correlator in time.

3.1.3 Neutron scattering on liquids and amorphous systems

Liquids and amorphous systems are characterised by the absence of long range order, i. e. the periodic repetition of one particular unit cell. Consequently, the different nuclei are not fixed on distinct lattice positions as in a crystal. Thus selection rules like for single crystals according to Bragg's law $\vec{G} = \vec{q}$ does not apply. $\vec{G}$ denotes a reciprocal lattice vector and $\vec{q}$ the scattering vector. Consequently, in liquids no narrow Bragg reflections are observed compared to a polycrystalline powder in the static structure factor.

The static structure factor $S(q)$ is obtained from the scattering law $S(q,\omega)$ using

$$S(q) = \int_{-\infty}^{\infty} S(q,\omega)\, d\omega\,. \tag{3.12}$$

A neutron diffraction experiment performed at low temperatures with a large enough incident neutron energy measures $S(q)$.

Despite of the disorder, characteristic length scales for nearest neighbour distances prevail. One observes broad maxima and minima in the structure factor at larger momentum transfers reflecting typical nearest neighbour distances in case of a coherent scatterer. In addition, certain liquids may show additional order on intermediate length scales, resulting from the repetition of particular bonding distances in the system. For example,

amorphous SiO_2 shows a first maximum around 1.6 $Å^{-1}$ in the structure factor below momentum transfers reflecting typical nearest neighbour distances [PrCa87, Ell91]. Data of a recent experiment at D20 on amorphous SiO_2 powder is shown in figure 6.11 [Poh05].

Incoherent scattering gives only rise to a constant in the static structure factor. For an one component and purely incoherent scatterer it can be shown that $S(q)$ equals unity independent of q. In case of an one component and purely coherent scatterer $S(q) \propto \kappa_T$ in the limit $q \to 0$ with κ_T denoting the isothermal compressibility. $S(0)$ can be estimated from literature data using the density ρ and κ_T at a given temperature. For the estimation the relation

$$S(0) = \rho N_A \kappa_T k_B T / A_m \tag{3.13}$$

with the Avogadro constant N_A and the molar mass A_m was employed. Using tabulated isothermal compressibilities and densities at various temperatures and compositions [MaSS83, MaSS85] the contribution to the structure factor is estimated for the investigated oxidic melts to be below 0.1 on an absolute scale. In the limit $q \to \infty$ the structure factor also approaches unity for coherent scattering.

The samples investigated in this work are mixtures of at least three different atoms with varying coherent and incoherent cross sections. Thus the behaviour of the structure factor is complex and particular features cannot be easily explained. However, the expected behaviour at small and large momentum transfers limiting the experimentally accessible range can be discussed. In amorphous SiO_2 a minor incoherent contribution arises only owing to the fact that SiO_2 is a mixture of two different sorts of atoms. The flat background visible at small q is dominated by the compressibility. At intermediate q coherent scattering reflected by maxima and minima in the structure factor dominates the scattering. The $S(q) = 1$ limit even not applies in amorphous SiO_2 and more generally speaking in all oxidic glasses and melts up to 18 $Å^{-1}$ as shown in a neutron diffraction measurement on amorphous SiO_2 [PrCa87]. It is only approximately valid for momentum transfers well exceeding q of 20 $Å^{-1}$ in oxidic melts [StHI01].

In our experiments the experimentally chosen wavelength yields a restriction to momentum transfers close above the first sharp diffraction peak around 1.7 $Å^{-1}$ to 2.1 $Å^{-1}$. Two regions can be distinguished in the structure factor. At small q values the structure factor is flat featuring no distinct correlation peaks. In this range incoherent scattering and a contribution due to the compressibility contribute to the signal. At larger q values coherent scattering dominates the spectra.

In the alkali silicates incoherent scattering on Na as the only species exhibiting an incoherent cross section different from zero[2] gives the dominant contribution to the incoherent scattering signal at small wavenumbers. Thus the Na self correlation is probed at small wavenumbers. At larger wavenumbers coherent scattering on the network components Si and O dominate the spectra. Here incoherent scattering on Na gives only a minor contribution to the overall signal. The same holds for silicates containing Li and K. For the latter two we note that the incoherent cross sections are reduced by a factor of approximately two and six compared to Na.

In sodium borates both Na and B have an incoherent cross section different from zero.

[2]compare table A.1 summing up the scattering cross sections.

The incoherent cross section of B is a factor of eight smaller than the incoherent cross section of Na. Hence, the sodium diborate sample is characterised by a ratio of the incoherent cross sections of Na to ^{11}B of approximately four to one. Consequently incoherent scattering at small wavenumbers is still dominated by scattering on Na.

In a time-of-flight measurement the static structure factor $S(q)$ is not accessible for two reasons. At larger temperatures the Debye-Waller factor f_q is different from unity. Kinematic restrictions on the accessible energy and momentum transfer range for $S(q,\omega)$ do not allow for a proper integration.

A neutron time-of-flight experiment directly probes the elastic structure factor $S_{el}(q)$. The latter is defined as the scattering law at energy transfer $\hbar\omega$ equal to zero and is thus a well defined quantity.. To derive an elastic structure factor in melts at high temperatures is an advantage compared to measurements of the static structure factor. Corrections due to multi-phonon scattering that gives substantial contributions to the scattering law at energy transfers different from zero and increase in strength with increasing wavevector have not to be applied. With respect to the instrumental setup the energy resolution of the instrument is finite. The elastic structure factor is obtained via integration of $S(q,\omega)$ over the energy resolution function $R(q,\omega)$

$$S_{el}(q) = \int_{R(q,\omega)} S(q,\omega)\, d\omega\,. \tag{3.14}$$

The elastic structure factor well approximates to be equal to the static structure factor multiplied with the Debye-Waller factor

$$S_{el}(q) = f_q \cdot S(q)\,. \tag{3.15}$$

3.2 Mode coupling theory for viscous liquids

Universal predictions of the dynamics and its relation to the structure are given by the mode coupling theory (MCT) on approaching the point of liquid to glass transition. Fits with the universal scaling functions of the theory have been found to be in qualitative and in some cases even quantitative agreement with experimental or MD simulation data. An overview of the analysis of MD simulation data on supercooled liquids in the framework of the mode coupling theory is shown in [Kob99]. Especially the limits of the theory and corrections to its simple form are discussed. In this study simulation work on H_2O, SiO_2 and a binary Lenard Jones mixture that well reproduces the predictions given by the theory are discussed. Dense metallic liquids that are close to the ideal case of a dense liquid consisting of hard spheres were studied by means of inelastic neutron scattering [Mey02]. The measured density correlation function in the latter case is described by the universal scaling functions predicted by the MCT. For a recent and more detailed summary of the application of the mode coupling equations on experimental data the reader is referred to [Got99].

In the following subsections a short discussion on the basic concepts as well as the universal scaling functions used as fit formula to describe experimental data obtained for sodium borates are presented. A more detailed discussion of the universal scaling laws and MCT can be found in [Got90a, Got90b, Got91] and references given herein.

3.2.1 Basic concepts and results

The dynamics of a fluid can be described by the generalized form of the Langevin equation obtained by the Mori-Zwanzig projection formalism

$$\ddot{\Phi}_q(t) + \Omega_q^2 \Phi_q(t) + \nu_q \dot{\Phi}_q(t) + \Omega_q^2 \int_0^t dt'\, m_q(t-t')\dot{\Phi}_q(t') = 0 \tag{3.16}$$

The first two terms are similar to the differential equation of a harmonic oscillator with a characteristic frequency Ω_q. The term $\nu_q \dot{\Phi}_q(t)$ describes a driving force comparable to a friction force of the damped harmonic oscillator. The integral term contains a memory kernel $m_q(t)$ that couples the force to a velocity at earlier times. Thus the dynamics of the system, namely the density fluctuations, at time t is determined by the state of the system at an earlier time t'. The central issue is to find an appropriate description of the memory kernel, since there is no exact solution available for the latter. Within mode coupling theory the memory kernel is described by a sum over coupling constants relating the density correlators at different moments and times. The coupling constants are shown to be determined by summation of products of structure factors and correlators [Got91]. Respecting mode coupling theory the simplest form of coupling that includes already a singularity marking the liquid to glass transition is given by the coupling of two density correlators with their corresponding structure factors. The dynamics of a system is entirely determined by its structure. The theory provides detailed predictions of the dynamics based on a microscopic quantity, the partial structure factors. However, calculating absolute values of macroscopic parameters like the viscosity and density only from this microscopic description is still not directly achieved.

The dynamics in dense hard sphere liquids was successfully described within the framework of the mode coupling theory of the liquid to glass transition. A number of systems to which the mode coupling theory was successfully applied are comprised in [Got99] and the references cited therein. Developed for hard sphere systems mode coupling theory was also applied successfully to molecular glass forming liquids like orthoterphenyl (OTP) [RiDP88, WuHL94, Tol01]. Molecular glass formers including OTP have e. g. been subject of light scattering experiments and some thesis works performed at the Institute E13 [Gol01, Wie03]. Still recognized as hard sphere liquid, the inherent complex structure of OTP plays no role for freezing of the structural relaxation.

Despite the structural complexity of these systems, they only feature a single structural relaxation time. Scaling laws calculated within the mode coupling theory describe the microscopic dynamics on approaching the point of liquid to glass transition. The latter occurs when the system changes from an ergodic liquid like state to a non ergodic glassy state. In reality, ergodicity in the glass phase is restored by hopping events. Thus transport properties on a microscopic scale change from viscous flow to solid like hopping.

A schematic overview of different relaxation processes in a viscous liquid is presented in figure 3.1. In a microscopic picture these long range motions of molecules or atoms are reflected in a decay of the correlation function. The characteristic time scale of this decay, τ_α, increases upon approaching the transition. In the glass state the long time dynamics

is frozen. Thus no α relaxation process is observed. The α relaxation process is described by a stretched exponential function (see section 3.3 for details). The stretching exponent depends on the experimental method used for the investigation, but shall not depend on temperature. Mode coupling theory shows that time temperature superposition shall hold for the α relaxation that means that independent of changes in temperature the α relaxation process rescaled by relaxation time and amplitude fall on top of a single master curve. Dense viscous liquids feature not only a structural relaxation, but also a secondary relaxation process. This so called fast β relaxation process can be visualized by a rattling motion of the atom or molecule in the cage formed by its neighbours. In order to escape from this cage, the neighbours of the particle have to move. Consequently, the correlator decays on the timescales of the α-relaxation. The fast β relaxation process is represented by the power law decay which is the transient between the regime of vibrations and the α relaxation.

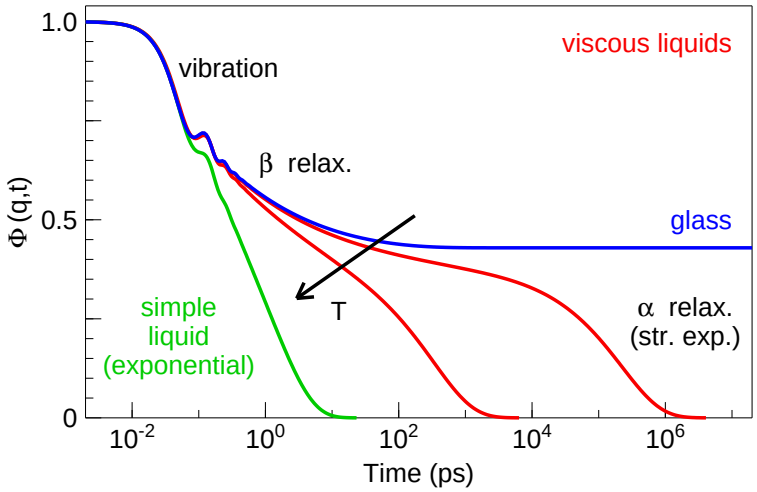

Figure 3.1: Schematic representation of the density correlation function in viscous liquids (red curves) and in a simple liquid (green curve) calculated by Götze and coworkers. The characteristic density correlation function for an ideal glass state is represented by the blue curve. Simple liquids feature two decays: A decay at short times due to vibrations and a single exponential decay characteristic for the diffusion of a single particle. In viscous liquids the behaviour is different. A detailed discussion is provided in the text.

3.2.2 Scaling laws

In the following the calculated asymptotic scaling laws of the mode coupling theory presented in [Got90a, Got90b] are discussed. These scaling laws are applied later to the sodium borate systems which feature a fast relaxation process in the density correlation function. This fast relaxation is a transient between the short time regime of vibrations and the long time α relaxation regime. Even in the melt our sample is heterogeneous with respect to the α relaxation for the different components[3].

[3]For a visualization of this decoupling of timescales of structural relaxation the reader is referred to section 6.1, in particular to figure 6.2. The figure shows how the different α relaxation processes manifest

The universal scaling function that describes the density correlation function according to the theory reads

$$S_q(t) = f_q + h_q g_\lambda(t/t_\sigma)\,. \tag{3.17}$$

This theoretical description of the density correlation function in the framework of the mode coupling theory comprises four parameters, f_q, h_q, t_σ, and λ. g denotes the scaling function that depends on λ and t_σ. Three of these four parameters obey scaling laws predicted by the theory. The different parameters are discussed in the following paragraphs. With respect to (3.17) the first parameter f_q is named the non ergodicity parameter, also called the plateau value. Ideally at the critical temperature T_c the equation

$$S_q \overset{t\to\infty}{=} f_q \tag{3.18}$$

is valid. T_c marks the point of the transition ergodic to non ergodic. In the liquid state f_q is the value of $S(q,t)$ between the β and the α relaxation regime. For a coherent scatterer f_q corresponds to the Debye-Waller factor. For an incoherent scatterer it is the Lamb Mößbauer factor. In one component liquids it can directly be read off as the value of the plateau between the microscopic transient in the sub picosecond range and the α relaxation. f_q is proportional to the elastic structure factor. The second control parameter in (3.17) is the wavevector dependent critical amplitude h_q of the fast relaxation process. In first approximation it is in antiphase to the structure factor. For a purely incoherent scatterer h_q is expected to increase with raising wavevector. For a coherent scatterer h_q features maxima and minima in antiphase to the non ergodicity parameter. The mode coupling theory predicts a scaling of h_q^2 with temperature

$$h_q^2 \propto (T - T_c)\,. \tag{3.19}$$

At the critical temperature T_c structural arrest ideally occurs. However, in real systems already close above this temperature hopping processes set in yielding further structural relaxation. Consequently, τ_α, the time scale of the α relaxation, diverges not to infinity. The α relaxation timescales follow at temperatures $T \ll T_c$ an Arrhenius law. The remaining two control parameters t_σ and λ determine the transition from the β to the α regime and the lineshape of $S(q,t)$ close around t_σ, respectively. The lineshape parameter is a system-dependent, but wavevector- and temperature-independent quantity according to the theory. t_σ is expected not to depend on q, but to follow the relation

$$t_\sigma^{-2a} \propto (T - T_c)\,. \tag{3.20}$$

T_c is the same critical temperature as obtained by (3.19).

As stated earlier the scaling function g_λ depends only on the transition time and the lineshape parameter. For the fit to the measured data we use the scaling approximations for g_λ presented in [Got90a]. According to mode coupling theory two relaxation regimes can be distinguished. The first one describes the α relaxation process roughly for times

themselves in the measured density correlation function.

$t > t_\sigma$. The β relaxation regime applies for $t < t_\sigma$. In the α regime close to t_σ $S(q,t)$ can be described by the asymptotic scaling law

$$g_b(t) = -Bt^b + (B_1/B)t^b \,. \tag{3.21}$$

In the short time limit $S(q,t)$ yields the asymptotic behaviour of

$$g_n(t) = t^{-a} - A_1 t^a + A_2 t^{3a} - A_3 t^{5a} + ... + (-1)^n A_n t^{(2n-1)a} \,. \tag{3.22}$$

It was shown that the latter formula does converge. An accuracy of about 1% is given by a cutoff after the term t^{5a}. The critical exponents a and b of (3.21) and (3.22) depend on λ following the transcendental equation

$$\Gamma(1-a)^2/\Gamma(1-2a) = \lambda = \Gamma(1+b)^2/\Gamma(1+2b) \,. \tag{3.23}$$

The coefficients B_1, A_1, A_2 and A_3 can be numerically calculated. They depend only on the lineshape parameter λ in a nontrivial way. The parameter B is obtained by solving the scaling equation using a regular for g_λ. For different λ the corresponding expansion parameters are tabulated in [Got90a]. The time t in the expansion formulas (3.21) and (3.22) corresponds to the time measured experimentally rescaled with the transition time t_σ. In [Got90a] the time t^* was calculated. For this time the function $g_\lambda(t)$ does vanish. Thus the two asymptotes $g_b(t)$ and $g_n(t)$ cancel out each other. t^* was numerically calculated and also depends on λ. In the fit to the data t^* is used as the crossover time from the short time scaling law $g_n(t)$ to the long time scaling law $g_b(t)$. The long time scaling law (3.21) describes the onset of the α relaxation and is often referred to as van Schweidler law.

Mode coupling theory makes predictions about the behaviour of the fit parameters in (3.17) on a change of external parameters. A fit of (3.17) to measured data that are not normalized by means of the static structure factor $S(q)$ yields f_q being proportional to the elastic structure factor $S_{el}(q)$. h_q is expected to increase with increasing momentum transfer. Moreover, it shall feature maxima at the same position as the structure factor if coherent scattering contributes to the β relaxation. The temperature dependence of h_q and t_σ is given by scaling equations provided by the theory. For a standard type-B glass former[4] the scaling laws (3.20) and (3.19) hold true.

The scaling equations are only valid close to the glass transition temperature T_c for ideal systems. For systems where hopping sets in at lower temperature still close above the ideal glass transition temperature T_c one might also expect corrections. However, the necessary corrections can only be calculated by knowing the detailed behaviour of the system under investigation. In case of the multicomponent ion conductors this calculation is rather complex and was not subject of this thesis work. Results obtained by the data analysis are affected too close and too far away from the critical temperature marking the glass transition.

The quantity characterising the relaxation behaviour of an ideal system beyond T_c is

[4]For a proper definition of type-B and type-A glass formers the reader is referred to [Got91].

the structural relaxation time τ_α. Within the theory the latter is shown to obey the scaling equation

$$\tau_\alpha = A \cdot (T - T_c)^{-\gamma} \tag{3.24}$$

with $\gamma = 1/2a + 1/2b$ dependent on the line shape parameter λ via (3.23). The equation exactly reflects the diverging behaviour of the timescale of structural relaxation.

3.3 Structural relaxation in disordered systems

To describe the diffusion that means the long range motion of atoms one can start from Ficks law of diffusion that reads

$$\frac{\partial \rho(\vec{r}, t)}{\partial t} = D\nabla^2 \rho(\vec{r}, t)\,. \tag{3.25}$$

We recall that $\rho(\vec{r}, t)$ is the density of atoms at point $\vec{r}$ at time t. In simple one component and not dense liquids, e. g. Na, Rb and Ar, the transport of atoms can be readily identified. The solution of Ficks law of diffusion is given by a simple exponential decay in the density correlation function. The scattering law – the Fourier transform of the density correlation function – is thus a single Lorentzian function. For a purely incoherent scatterer the relaxation rate follows a q^2 dependence at small momentum transfer values. At large values of momentum transfer the relaxation rate bends over to the regime of free flight. At intermediate wavenumbers D may show a non trivial q dependence. In the diffusive regime the relaxation time is related to the self diffusion constant via

$$D = 1/(q^2 \tau_\alpha)\,. \tag{3.26}$$

The latter always holds in the limit $q \to 0$. Coherent correlators are supposed to decay with a single exponential function. However, the relaxation times feature a dependence on q which shows oscillations in phase with the structure factor. Measurements on liquid Argon [SkRO72] and liquid Neon (reference in [CoLo75]) clearly reflect this behaviour.

In viscous liquids comprising different components the scenario is more complicated. It was shown in the previous section that the α relaxation leads not to a single exponential decay. Rather a stretched exponential behaviour is observed. It was shown that the solution of the mode coupling equations for large wavenumbers yield stretched exponential behaviour [Fuc94].

Stretched exponential decay means that the correlator decays less quickly compared to a simple exponential relaxation. The behaviour is most pronounced in the onset of the decay of the correlator. In order to describe such a decay, a stretched exponential function

$$S(q, t) = a \cdot \exp\{-(t/\tau_q)^\beta\} \tag{3.27}$$

shall be used. Apart from the explanation provided in the framework of the mode coupling theory only for particular cases the stretching exponent has a physical meaning. The latter is true for relaxation in fractal geometry, where the stretching exponent can be related to the fractal dimension. For a detailed description the reader is referred to chapter 5 in [RiBl94] and references given therein.

The stretching can be understood in the distribution of rates originating from a distribution of energy barriers. However, this picture shall be only used to visualize the meaning of such a stretching.

Whether the relaxation observed in the experiments is diffusive or not, can be justified in the framework of the Gaussian approximation. The self correlation function $\Phi(q,t)$ that is normalised to unity for $t = 0$ is related to the mean square displacement $\langle r^2(t)\rangle$ of the particle [BoYi91].

$$\frac{-\ln \Phi(q,t)}{q^2} = \langle r^2(t)\rangle \,. \tag{3.28}$$

The formula is valid in the limes $q \to 0$. For simple diffusive behaviour the mean square displacement shall linearly vary with time. Its slope corresponds to the diffusion constant. If the picture of simple diffusive motion does hold true, the mean square displacements shall merge to a single master curve over a distinct wavenumber range. Deviations from this behaviour are expected for a stretched decay of the correlation function. In the limit of large times no distinct difference between a linear and a power law behaviour can be detected. A fit in this linear region will reveal the diffusion constant D.

In metallic glass formers based on Ni the self motion of Ni was obtained by means of neutron time-of-flight spectroscopy [Mey02] with the self correlation functions revealing stretched behaviour. Mean relaxation times follow a q^2 dependence indicating simple diffusive motion up to the largest wavenumbers. In the metallic liquids the first maximum in the structure factor corresponding to nearest neighbour distances of the atoms is well beyond the accessible momentum transfer range. Scattering was entirely incoherent. To determine D from a fit of (3.27) to the measured $S(q,t)$, the following relation

$$\langle \tau_q \rangle = \int_0^\infty dt\, e^{-(t/\tau_q)^\beta} = \frac{\tau_q}{\beta} \cdot \Gamma\left(\frac{1}{\beta}\right) \tag{3.29}$$

was used. Γ denominates the well known Gamma function. The relaxation time τ introduced in (3.27) depends on the stretching exponent β. The latter is not necessarily constant with q. In a number of experiments it has been shown that the mean relaxation time $\langle\tau\rangle$ calculated according to (3.29) allows for an accurate description and is independent of the stretching exponent. It corresponds to the area under the stretched exponential curve. Using the equation (3.29) one suggests a similarity to a simple exponential decay. For the latter it can be shown that the area under the curve equals to $1/Dq^2$. This corresponds to the relaxation time τ. For q values much larger than zero the relaxation rate is proportional to Dq. Moreover as shown by the MCT D is proportional to $1/S_q$. Coherent scattering that contributes maxima and minima to the partial structure factors will lead to oscillations of $\langle\tau\rangle$.

In a frozen environment transport of mobile ions was shown to be governed by hopping motions in several experiments. This motion was also described within the framework of the hopping model [FuHo90].

The hopping model belongs to the similar approach as shown by other models that have been developed to describe diffusion in low dimensions. In particular, the scattering law $S(q,\omega)$ corresponding to diffusion restricted to a spherical potential is presented

in [VoDi80]. This model was successfully applied to a number of hydrogen containing systems. They feature hydrogen motion restricted in space by the surrounding framework. The latter could for example be a porous glass structure as investigated in [ZaBC99].

In case of a hopping transport a typical lengthscale for the hopping motion will become accessible. It marks the point of the deviation of the mean square displacement of the long time linear behaviour to the region of vibrations. A more rigorous test, whether the motion is of diffusive nature, is the time dependence of the velocity autocorrelation function. The latter is proportional to the second time derivative of the mean square displacement and it shall become zero for diffusive behaviour.

However, typical accuracies of a few percent obtained in experiments do not allow for a proper determination of the velocity autocorrelation function. Double differentiating measured data leads to substantial noise yielding an ambiguous explanation.

In systems featuring hopping motion relaxation timescales derived from the self correlation function of the moving particle feature a characteristic q dependence with maxima and minima over a sufficiently large q range. A similar argument holds for the amplitude of relaxation. The characteristic lengthscale for hopping between rather distinct positions can be derived from a fit on the measured relaxation rates or amplitudes by applying the fit functions provided by the model.

The simplest possible relation between D, τ and the characteristic hopping length l is provided in the jump diffusion model [Ege92] by

$$1/\langle\tau_q\rangle = 1/\tau_0 \cdot \frac{q^2 l^2}{1 + q^2 l^2} \,. \tag{3.30}$$

This model assumes a characteristic waiting time τ_0. As it is elapsed, the particle overcomes the energy barrier and is subject to a hop of characteristic length l. The characteristic diffusion constant D is given by

$$D = l^2/\tau_0 \,. \tag{3.31}$$

(3.30) essentially describes an increase of the relaxation rate according to a q^2 law of simple diffusion in the limit of small q. The derived diffusion constant can be compared to the diffusion constant derived from a simple Dq^2 fit on the measured relaxation rates. At larger q the relaxation rate deviates from the q^2 increase bending over to the limiting value of $1/\tau_0$. Function (3.30) is applied to fit the relaxation rates of sodium disilicate (see section 6.1.2).

Chapter 4

Experimental methods

Inelastic neutron scattering is used to investigate the structure and dynamical behaviour of oxidic melts. Neutron time-of-flight spectroscopy and neutron backscattering provide access to the dynamics on different timescales. The basics and the peculiar advantages of each technique are discussed in section 4.1. Section 4.2 is devoted to the presentation of the setup used for the investigations of oxidic melts and glasses for these instruments. Afterwards, the analysis of neutron data is explained (section 4.3).

4.1 Neutron scattering methods

Neutron scattering is a highly versatile method in studying relaxation phenomena on a microscopic level. With the use of different instruments a range of picoseconds to nanoseconds in time and lengthscales of inter-atomic distances to several tens of Angstroms is covered.

Before the two neutron scattering methods used for our investigations are briefly discussed, an overview of the sample environments is presented. The first paragraph commenting on the instruments is devoted to neutron time-of-flight spectroscopy. In the second paragraph some important points of the neutron backscattering technique are noted.

4.1.1 Sample environment

For the high temperature neutron scattering experiments we used Pt hollow cylinders providing an annular sample geometry (see figure 4.1). To cover the neutron beam an outer diameter of 23 mm and a sample height of 30 mm was chosen. The sample thickness of 1.25 mm results in a scattering power varying for our samples and the incident neutron wavelength used in the range of 5% to 8% only. Hence, multiple scattering is decreased down to a minor event.

Neutron scattering measurements were performed using high temperature furnaces provided by the ILL and NIST, respectively. The furnaces were operated under vacuum. The heating element and heat shielding consists of Nb. The sample holder was closed by pressing the inner and outer wall of the holder tightly together. Further sealing of the sample was provided by a Pt foil bent around the upper part of the container. The foil

Figure 4.1: Platinum hollow cylinder used for the inelastic neutron scattering experiments. It provides an annular sample geometry with the following dimensions: cylinder height 50 mm, sample height up to 30 mm, sample thickness 1.25 mm, wall thickness 0.3 mm and outer diameter 23 mm. The container is sealed by bringing the inner and outer Pt cylinder in close contact. The sample holder is further shielded by a Pt foil. The latter is self-welding at elevated temperatures during the experiment.

was fixed by the Nb disks used to hold the Pt container. Self-welding of Pt sets in at high temperatures. Due to the careful sealing process the sample remains stable in the Pt container, though oxidic melts feature a low surface tension under vacuum on a Pt surface. As experienced during the first experiments sample material lost from the container tends to react with Nb and in particular with the heating elements of the furnace. In one of our experiments a reaction of boron oxide with Nb and the Pt container lead to a complete removal of the sample holder.

The low temperature experiments on the iron bearing silicates were performed in a standard ILL Orange cryostat. Using an annular sample geometry without a sample holder that yields a scattering power below 10% is not possible for the glasses.

Consequently, we used a flat plate geometry for the experiments on IN6. Preparing glass disks from the melt yielded samples with 33 mm diameter and a thickness of about 1 mm. Hence the samples exhibit a scattering power of $\lesssim 5\%$. An aluminum frame shielded by Cd was used as sample holder yielding a container free experiment. The sample was oriented with an angle of 135° to the incoming neutron beam. Hence, the experiment was only performed in transmission geometry. Corrections imposed on the data analysis are reduced as well. The sample geometry chosen for N2FS6 measured on the polarized neutron diffractometer D7 was a glass rod consisting of four separate cylinders. The cylinders were contained in a thin Al foil. The total sample height was 28 mm with an outer diameter of 16 mm. This corresponds to a scattering power of approximately 25%. Since we were only interested in magnetic scattering contributions, the scattering power of the sample asks not for major corrections during the data analysis due to multiple scattering. The latter would clearly be an issue for a time-of-flight experiment on a similar sample geometry addressing quasielastic scattering.

4.1.2 Time-of-Flight spectroscopy

Neutron time-of-flight spectroscopy simultaneously determines the energy and momentum transfer a neutron experiences during the scattering process on the sample. Effectively it measures the scattering law $S(q, \omega)$ in a kinematically restricted subspace of the q and ω plane. At a steady state source (neutrons by fission) the originally white neutron beam with a Maxwellian velocity distribution is pulsed and monochromated. This is either done by a system of choppers (e. g. IN5 at ILL, DCS at NIST, TOFTOF at FRM-II) or by a combination of a crystal monochromator and choppers (e. g. IN6 at ILL). Only

IN6 and the new IN5 spectrometer were the most powerful instruments providing high enough neutron flux and an outstanding low background to allow for a quasielastic neutron scattering study of oxidic melts[1].

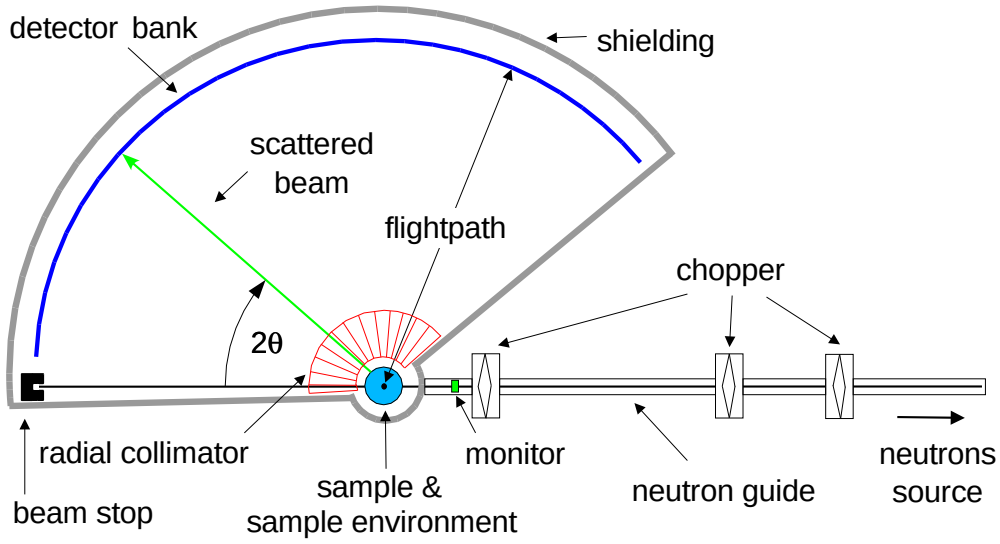

Figure 4.2: Schematic view of a chopper monochromated time-of-flight spectrometer, as IN5 (ILL) or TOFTOF (FRM-II).

The monochromatic neutron pulse enters the sample chamber and is scattered on the sample and its environment. The sample environment, which could be e. g. a furnace or a cryostat, is mapped out by means of a radial collimator. The latter is either mounted in the sample chamber or behind the entrance window to the secondary spectrometer. It consists of radially oriented thin blades that are coated with a neutron absorber (typically GdO_2). The number of blades is chosen according to the solid angle an instrument covers and to the suggested radius of acceptance. The latter means the maximal distance of the point at which the scattered neutrons are transmitted to the detectors of the center of the radial collimator. Typical radii of acceptance for the radial collimators of IN6 and DCS are of the order of 2.5 cm. Consequently, an appropriate sample size has to be chosen. The sample geometries chosen for our experiments that have a radius that is two to three times less than the radius of acceptance provide maximal neutron intensity at the detectors. Divergence of the incoming neutron beam is only a major issue if the sample dimensions are of the order of the radius of acceptance. Ideally, only neutrons scattered at the sample shall be transmitted. The efficiency of the radial collimator is connected to the scattering angle. At small angles close to the forward scattering scenario the radial collimator is relatively inefficient. The radial collimator is moved continuously around the sample. This prevents shadowing peculiar detectors which would yield strongly different intensity at the detectors. The sample must be ideally placed in the center of the sample

[1]The TOFTOF spectrometer even providing higher flux at a comparable or even lower background level compared to IN6 came only recently into operation.

box that coincides with the center of the circle described by the secondary spectrometer. A offset of a few millimeters would lead to an error in the 5 % to 10 % range as evidenced in the measurement performed at DCS in 2003 [2]. Additionally, the sample shall not exceed the horizontal beam dimensions. Especially for a non homogeneous horizontal flux distribution one might end up with an error in the range of 20 % after applying the necessary corrections.

The neutrons scattered on the sample cover the distance between the sample and the detectors until they are detected. The energy of a detected neutron is determined via the time it needed to approach the detectors after being scattered on the sample. The time divided by the flightpath gives the time-of-flight that is used in the further discussion. It is denoted by ToF. It corresponds to the inverse of the neutron velocity v in units of [ms/m]. The velocity of the neutrons acts as intrinsic property for that purpose. The wavelength of the incident neutrons and thus their energy and velocity is well known. The energy of a neutron is given by

$$E = \hbar^2 k^2 / 2 m_N \,, \tag{4.1}$$

where k denotes the absolute value of the wave number and m_N the neutron mass. Consequently, the energy E of a neutron, its velocity v and wavelength λ are related via

$$\begin{aligned} E_{[\mathrm{meV}]} &= 81.805 / \lambda^2_{[\mathrm{Å}^2]} \\ v_{[\mathrm{m/s}]} &= 3956 / \lambda_{[\mathrm{Å}]} \,. \end{aligned} \tag{4.2}$$

For convenience also the conversion of energy between different types of presentation used in literature is noted

$$4.13\,\mathrm{meV} \mathrel{\widehat{=}} 1\,\mathrm{THz} \mathrel{\widehat{=}} 8.1\,\mathrm{cm}^{-1} \,. \tag{4.3}$$

The velocities of the detected neutrons are in the range of several hundred to about 4000 m s^{-1}. With typical flightpaths in the order of 2.5 m (IN6) to 4 m (IN5) the time to approach the detectors is in the range of milliseconds. FWHM of the energy resolution function is of the order of several tens of microseconds. The energy resolution of a time-of-flight instrument depends on a number of parameters. In the following we go not very much into detail, we only provide some rules of thumb. Besides the neutron pulse width that is determined by the chopper velocity, the flightpath is one of the parameters which determines the maximal achievable energy resolution. We note the shorter the flightpath the lower is the maximal achievable energy resolution. However the advantage of a shorter flightpath is that a larger solid angle is covered by the detectors which leads to a larger number of neutrons detected per time interval for the same incident neutron intensity. Besides the flightpath, the sample dimensions, e. g. the diameter in case of an annular sample, contribute to the resolution. The larger the sample the worse the resolution. Finally, the detector thickness also contributes to the energy resolution. The latter two contribute via an uncertainty in the length of the flightpath between scattering and detection of the neutron. Depending on the neutron velocity a flightpath difference of the order of 1 cm corresponds to a timeshift of the order of tens of microseconds.

[2] At DCS the center of the sample box and the horizontal center of the beam were off by ~ 6 mm. This lead to significant deviations of the measured intensity at intermediate scattering angles.

Neutrons that are elastically scattered at the sample experience no energy transfer. They arrive at the detectors after the time given by the incident neutron velocity and the sample detector distance. Inelastically scattered neutrons are counted either earlier or at a later time, depending on whether they have gained or lost energy during the scattering process. The detection process itself is continuous in time. The time interval between two neutron pulses is split in equidistant time intervals. Neutrons that are slower than the time between two neutron pulses are counted among neutrons of the next pulse. This problem is named frame overlap, while the time between two pulses is referred to as frame. This overlap cannot be completely suppressed, since the neutrons loosing energy during the scattering process can be infinitely slow. However, to prevent neutrons which have gained energy from overlapping with neutrons which are elastically scattered, an additional chopper is used. This chopper rotated at a fraction of the speed of the main chopper removes a defined number of pulses. Consequently, the frame is extended at the expense of intensity.

A sufficient separation of the frames is important to allow for a correct analysis of processes connected to small energy transfers. Stochastic scattering of the neutrons on diffusing constituents of the sample gives rise to additional scattering intensity around the elastic line. This scattering intensity is referred to in literature as quasielastic contribution to the scattering signal. It contains information of relaxation processes in the sample.

Typical energy resolutions provided by a time-of-flight instrument are in the order of 10 μeV to several 100 μeV FWHM. For inelastic scattering energy transfers up to several 100 meV can be probed.

Not only the energy transfer to the neutron is measured, but also the momentum transfer. The momentum transfer $\vec{q}$ to a neutron scattered at the sample is given by

$$\vec{q} = \vec{k}_i - \vec{k}_f \tag{4.4}$$

with $\vec{k}_i$ and $\vec{k}_f$ denoting the wavevector of the incident and the scattered neutron, respectively. This reduces in case of an isotropic scatterer to

$$q = \sqrt{k_i^2 + k_f^2 - 2k_i k_f \cos(2\theta)}\,, \tag{4.5}$$

where the norm of the wavevector is only dependent on k_i, k_f as well as the scattering angle 2θ. Using for elastic scattering

$$k_i = k_f = k = 2\pi/\lambda \tag{4.6}$$

with the wavelength λ, (4.5) reduces to

$$q = 4\pi/\lambda \ \sin\theta\,. \tag{4.7}$$

4.1.3 Neutron backscattering

The neutron backscattering technique is similar to time-of-flight spectroscopy respecting the measured physical quantity, the scattering law $S(q,\omega)$. However, the energy range

for which this quantity is determined is substantially different. Typical energy transfers are in the range of several 10 μeV with energy resolutions of around 1 μeV (FWHM). In neutron backscattering the Bragg condition

$$n\lambda = 2d \sin\theta \tag{4.8}$$

determines the uncertainty in wavelength $\Delta\lambda$ by

$$\Delta\lambda = \frac{\partial\lambda}{\partial d}\Delta d + \frac{\partial\lambda}{\partial\theta}\Delta\theta = \lambda\left(\frac{\Delta d}{d} + \frac{\Delta\theta}{\tan\theta}\right) . \tag{4.9}$$

The mosaicity of the crystal is given by Δd and the beam divergence by $\Delta\theta$. Ideally, for the backscattering condition $\theta = 90°$ only the mosaicity of the crystal determines the spread of the wavelength and thus the energy resolution. The backscattering principle is used for the monochromatisation of the incident beam as well as for analyzing the scattered neutrons. The energy transfer in the 10 μeV range is obtained by a variation of the incident neutron energy with the monochromator mounted on a Doppler drive. On the high flux backscattering spectrometer HFBS at NIST (Maryland, USA) the (111) reflection of perfect Si single crystals is used providing a wavelength of 6.27 Å.

Neutron backscattering is a highly intensity limited technique. The neutrons have to cross the sample twice before they are detected. The Pt cylinder used in our experiments is a strong absorber (64% transmission for one way) for the incident neutrons of 6.27 Å used at the HFBS. The peculiar design of the HFBS using a phase space transform chopper allows for higher neutron flux compared to conventional backscattering spectrometers at the expense of beam divergence. The latter only minor affects the energy resolution. Using the 36 μeV maximum energy transfer setup the energy resolution of the instrument was $\approx 1\mu$eV (FWHM). This gives access to processes on timescales in the range of ≈ 200 ps to ≈ 10 ns. A detailed description of the instrument can be found in [MeDG03].

For neutron backscattering a special designed furnace has to be used. It is different from standard ILL or Oxford instruments furnaces with respect to the diameter of the outer furnace wall. The detectors in a neutron backscattering instrument are positioned close to the sample. Thus typical diameters of the outer furnace wall are of the order of 20 cm. This leads to a more limited temperature range accessible with the furnace. However, temperatures of up to 1600 K used in the experiments can be reached [MeDS02].

4.2 Instrumental setup

In this section some remarks on the time-of-flight and backscattering instruments used for our investigations are noted. The main reasons for only performing our time-of-flight measurements at ILL and the neutron backscattering measurement at NIST are explained. The main part of this section will be devoted to the discussion of the setup used for the experiments.

The time-of-flight experiments were mainly performed on the IN6 spectrometer at ILL.

It provides access to timescales and momentum transfers shown in appendix B. The IN6 spectrometer was chosen due to its extremely low background level and the largest possible neutron flux on the sample. Both requirements were indispensable, since the investigated samples are rather weak scatterers. Moreover, the investigations at temperatures of 1600 K can only be performed over a limited timespan.

The IN5 spectrometer was chosen for the measurement of NS2. It provides access to lower momentum transfer values and longer timescales due to a longer incident neutron wavelength compared to IN6. In order to show that the assumptions made for the data measured at IN6 at small wavenumbers are physically reasonable, such an experiment was inevitable.

Neutron backscattering on oxidic melts was performed on the HFBS spectrometer at NIST. Owing to its design the HFBS is the only backscattering instrument currently into operation that provides the highest possible neutron flux. Only this instrument allows for reasonable statistical data quality within twelve hour runs at a given temperature. Measuring at four to six spectra in the melt, the maximum time stability of the sample holder at high temperatures is reached.

In the experiments focusing on relaxation dynamics we exclusively used an incident neutron wavelength larger than 4.8 Å. This corresponds to energies lower than $\simeq 3.5$ meV. The main advantage is that neither the first Bragg peak of the Pt container nor of the sample environment (Aluminum and Niobium) is excited. Thus elastic scattering of the sample environment and of the Pt cylinder is incoherent.

The incoherent cross section of the Pt cylinder is approximately a factor of 12 lower than the incoherent cross section of Na. The wall thickness of the Pt cylinder is $\simeq 0.3$ mm which is about a factor of two smaller than the thickness of the sample. However, the number density of scatterers in Pt is a factor of 5 larger than the number density of Na scatterers in sodium silicates. Hence, elastic scattering on the sample container at small momentum transfers is approximately a factor of five smaller than elastic scattering on only the sample. As shown in figure 4.3 the calculation agrees with the measured data. In this figure the elastic contributions of the sample and the container and of only the container are compared. At larger wavenumbers coherent scattering on the sample contributes substantially to the signal. Thus we observe up to a factor 50 in difference in both signals.

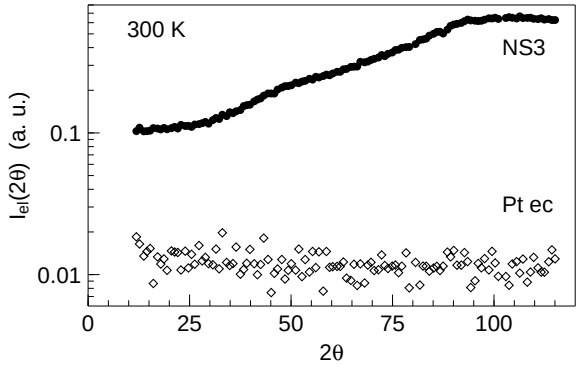

Figure 4.3: Elastic intensity of NS3 comprising combined scattering contributions of NS3 and the Pt can and elastic scattering of only the empty Pt can (Pt ec). The data were measured on IN6 at 300 K. The curves were obtained by means of summation of $I(2\theta, ToF)$ over the elastic line.

For the investigation of a quasielastic signal not only the ratio of elastic scattering,

but also the ratio of the sample and empty can intensity around the elastic line is crucial. Figure 4.4 shows the as measured intensity for NS3 contained in the sample holder and the intensity of the Pt empty can. The presented data were measured at room temperature and at 1600 K marking the typical temperature range of the experiments. As mentioned earlier the room temperature measurements serve as instrumental resolution function. In the left figure 4.4 a) the region around the elastic line is enlarged. Scattering on the Pt empty can is by at least one order of magnitude lower in the energy and temperature range of interest. Elastic contributions of the Pt container and the background level remain almost constant at low and at high temperatures. The elastic peak intensity decreases only with the Debye-Waller factor. In the sample it is not only an increase in vibrational contributions observed that manifests itself in the increase of the Debye level. Moreover, quasielastic scattering contributes to the measured intensity at 1600 K represented by broad symmetric wings. The data show that an annular Pt sample holder is an ideal container for the investigation of relaxation processes in oxidic melts.

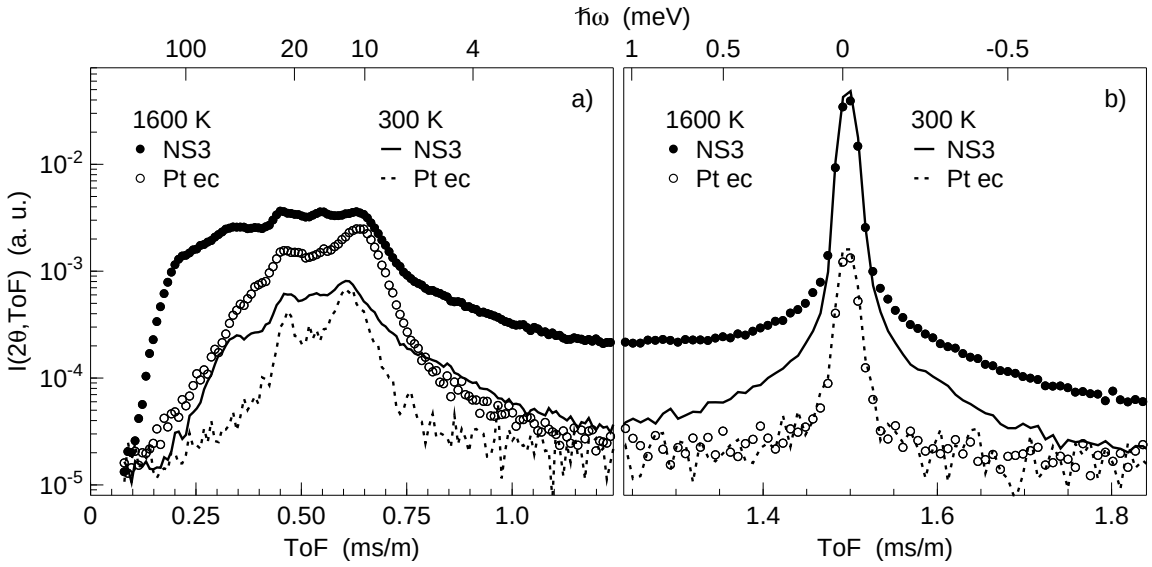

Figure 4.4: Intensity versus time-of-flight ToF measured on IN6. For clarity the data presented at a scattering angle of 74 ° was averaged over 26 ° with three time channels added. Both figures feature a comparison of the empty can (Pt ec) and a sodium silicate sample (NS3) at 300 K and in the melt. b) Enlarged region of inelastic scattering. Scattering on the empty can substantially contributes to the detected intensity. b) The region around the elastic scattering contributions is enlarged. Contributions of the empty can are almost negligible. Especially at large temperatures these contributions are still lower by one order of magnitude.

The data in figure 4.4 a) show that the assumption of a clear separation of the sample signal to the signal from the empty can is not valid in the inelastic range above 10 meV energy transfer. In this energy range scattering of the empty Pt can and scattering of the sample are of the same order of magnitude. The increase in the Debye level with increasing temperature can be directly identified in the same figure at large ToF. Consequently, for scattering experiments in the inelastic range a Pt container shall not be used. Consequently we performed no analysis of the density of states from neutron

scattering data for two reasons. The investigated systems comprises a mixture of coherent and incoherent scattering contributions. At high temperatures scattering on phonons of the Pt cylinder substantially contributes to the detected intensity. A iterative multi-phonon correction procedure [Sjo58] applied to derive the density of states of measured data is not applicable.

For the sodium borate samples similar behaviour is observed (not shown). However, there are differences in the ToF range between the elastic line and the first phonon contribution of the empty Pt can. In sodium borates not only the Debye level is observed[3]. We already find evidence for additional intensity in the glassy state compared to the silicates at room temperature. Thus it provides a hint for contributions of a Boson peak in these glasses and melts. The latter is not strongly pronounced and will be observed at energy transfers beyond 4 meV.

In the samples excitations owing to interatomic or intermolecular vibrations are experimentally observed at energies beyond 5 meV. Due to the low incident neutron energy of 2.4 meV the observed energy transfer range is restricted to the side at which the neutron gains in energy. Analysis of the data in terms of relaxation processes is thus performed exclusively on the Anti-Stokes side of the scattering law.

We used a standard ILL furnace as sample environment during the experiments providing a temperature stability better than $\sim 2\,^{\circ}$C. The sample was measured under vacuum. The furnace is operated by means of a Nb heat element and Nb shielding. Nb is only a weak neutron absorber and incoherent scatterer. An experiment performed in our group on metallic melts revealed an offset of of 55 °C between the temperature measured inside of the furnace and the temperature shown on the furnace display [MaMK04]. The latter was verified by means of measuring the crystalline to liquid transition in Ni and NiP. The melting point in these metallic melts is well known from macroscopic measurements and was used for an in situ calibration. In a neutron scattering experiment a sudden change of the scattering law from the solid state to the melt is observed. The width of the elastic line broadens owing to diffusing atoms. Additionally, a furnace calibration was performed at ILL revealing the same deviation down to $\sim 300\,^{\circ}$C.

The low temperature measurements on the iron containing glasses were performed at IN6 using an incident neutron wavelength of $\lambda = 4.1$ Å. Thus the first Bragg peak of Al around 2θ of 122.5° was excited. In addition to elastic scattering on the empty cryostat two distinct peaks are observed at slightly longer time-of-flights as the elastic peak. Assuming that neutrons contributing to this signal were also elastically scattered the extra flight path neutrons had to cover is estimated to be 12.7 cm for the first and 22.2 cm for the second peak. The measured intensity of the empty cryostat summed over all scattering angles is shown in figure 4.5. The region around the elastic line is enlarged. The first and second spurious peak are marked by vertical arrows. Elastic scattering at small angles is mainly incoherent. For $30^{\circ} \leq 2\theta \leq 60^{\circ}$ most of the elastic scattering is blocked, whereas at larger scattering angles elastic scattering intensity recovers. It slightly shifts to

[3]Reduced to the scattering law $S(q,\omega)$ and calculating the phonon density of states the Debye level will correspond to an ω^2 increase for small energy transfers. The latter is expected from the Debye approximation.

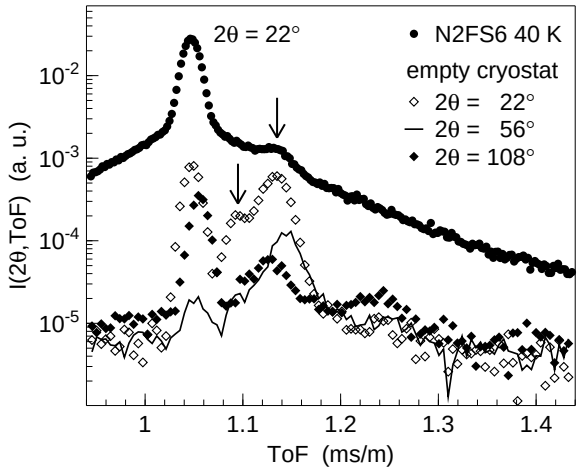

Figure 4.5: Normalised measured intensity versus ToF for N2FS6 at 40 K and $2\theta = 22°$ and the empty cryostat at room temperature. The vanishing elastic peak arising from scattering on the inner cryostat tube shows the radial collimator to be most effective at intermediate scattering angles. The dip in the sample curve is caused by one of the spurious peaks whose position are indicated by vertical arrows. However, it is still 40% lower than the sample intensity.

longer time-of-flights corresponding to about 2.5 cm extra distance. It arises from Bragg scattering and incoherent scattering on the inner cryostat tube. The intensity is about one order of magnitude lower than the intensity of the sample allowing for an easy subtraction. Furthermore, only the energy loss side is affected by the spurious peaks. The extra signal from the cryostat only becomes an issue for the 2 K measurement where the magnetic signal has to be analysed on the neutron energy loss side.

4.3 Reduction of neutron data

In the following section the raw data reduction for inelastic neutron scattering is discussed.

Despite differences in the details of the measurement procedure the reduction of time-of-flight and backscattering data is very similar. Thus no distinction is made for the different techniques. For the analysis of the data the IDA program developed by Joachim Wuttke was used. A recent version of the program was thoroughly tested prior to analysis of the data.

In general, raw data reduction consists of normalisation to a vanadium standard, correction for detector efficiency (only time-of-flight), correction for self absorption and container scattering and interpolation to constant wavenumbers q (only time-of-flight).

In a time-of-flight experiment the number of neutrons scattered to an angle 2θ in an angular interval $\Delta\theta$ arriving within a time interval Δt at the detectors are counted with a probability P_λ. The latter depends on the wavelength of the neutron and the incident neutron flux Φ_i approaching the sample in a given time interval $\Delta\tau$ for a defined area A. The incident flux is measured by a monitor which detects the neutrons of incident energy E_i with probability P_m. The total number of neutrons counted by the monitor during this time interval is

$$N_m = A_m \, P_m \, \Phi_i \, \Delta\tau \, , \tag{4.10}$$

whereas the number of neutrons detected under a solid angle $\Delta\Omega$ in a time interval Δt is given by

$$N_{SC} = P_\lambda \, P_j \, A_s \, \Phi_i \, I_{SC}(2\theta, ToF) \, \Delta t \, \Delta\Omega \, . \tag{4.11}$$

Dividing N_{SC} by N_m yields independence of the incoming neutron flux. To obtain the scattered neutron intensity versus scattering angle and energy transfer on an absolute scale and independent of the time interval and detection probabilities, the number of neutrons normalised to the monitor has to be normalised to an incoherent standard scatterer. Typically, Vanadium which scatters almost exclusively incoherent is used. For this material the Debye-Waller factor can be calculated in the Debye approximation for neither to high nor to low temperatures. Thus by division of the scattering intensity of Vanadium corrected for the Debye-Waller factor one obtains the scattering intensity

$$I_{SC}(2\theta, ToF) = \frac{N_{SC}}{N_V}\frac{A_V}{A_{SC}}\frac{I_V(2\theta)}{\Delta t}\,. \tag{4.12}$$

The measured intensity $I(2\theta, ToF)$ depends on the time-of-flight rather than on the energy transfer $\hbar\omega$. To calculate the double differential cross section and further the scattering law which is related to the detected neutron intensity the following equation relating $\hbar\omega$ and ToF is applied

$$\hbar\omega = \frac{1}{2}m_{\mathrm{N}}(1/ToF_{\,\mathrm{el.}})^2 - \frac{1}{2}m_{\mathrm{N}}(1/ToF)^2\,. \tag{4.13}$$

$ToF_{\mathrm{el.}}$ denotes the time-of-flight for incoming neutrons. This equation and its derivative have to be taken into account for recalculating the scattering law from the measured data. The measured intensity is proportional to the double differential cross section and the scattering law

$$I(2\theta, ToF) \propto \frac{\partial^2\sigma}{\partial\Omega\,\partial ToF}\frac{\partial ToF}{\partial\omega} \propto A\,\frac{k_f}{k_i}S(q,\omega)\,. \tag{4.14}$$

k_f also depends on the ToF by combining (4.1), (4.5) and (4.13). Hence, the calculation of $S(2\theta,\omega)$ based on $I(2\theta, ToF)$ yields a ToF^4-dependence that becomes more pronounced upon approaching the energy loss side of the spectrum

$$S(2\theta,\omega) \propto \frac{k_i}{k_f}\cdot\frac{\partial^2\sigma}{\partial\Omega\,\partial ToF}\cdot\frac{\partial ToF}{\partial\omega} \propto \frac{\partial^2\sigma}{\partial\Omega\,\partial\omega}\cdot ToF^4\,. \tag{4.15}$$

The counted neutron intensity is related to the double differential cross section which is the number of neutrons scattered in a solid angle $d\Omega$ and an energy interval dE

$$I_{SC}(2\theta,\omega) = n_{SC}z_{SC}\int d\omega'\,\frac{d^2\sigma}{d\Omega\;d\omega'}R(2\theta,\omega-\omega')\,. \tag{4.16}$$

n_{SC} denotes the combined density of scatterers of the sample and the container. z_{SC} the typical pathlength in this combined system. The detected intensity corresponds to the double differential cross section convoluted with the instrumental energy resolution function. The double differential cross section is related to the scattering law $S(q,\omega)$ via the prefactor A

$$\frac{d^2\sigma}{d\Omega\,d\omega} = A\,\frac{k_f}{k_i}S(q,\omega)\,. \tag{4.17}$$

This prefactor contains the different scattering cross sections of the different atoms weighted with their relative abundance. The scattering law can be written as a sum of an incoherent and a coherent part

$$S(q,\omega) = \frac{\sigma_{inc}}{4\pi} S_{inc}(q,\omega) + \frac{\sigma_{coh}}{4\pi} S_{coh}(q,\omega)\,. \tag{4.18}$$

Combining (4.17) and (4.18) one has to keep in mind that the incoherent part of the scattering law is weighted by the incoherent cross section, whereas the coherent part is weighted by the coherent cross section, respectively.

The measured intensity and thus also $S(q,\omega)$ comprises scattering contributions of the sample (I_S) and of the container (I_C), which are not additive. A simple subtraction of the scattering signal of the container from the combined scattering I_{SC} measured in a neutron scattering experiment is not possible. For a cylindrical sample geometry Paalman and Pings provided solutions of the the necessary correction factors [PaPi62]. Assuming, no interaction between the sample and the container affects the scattering in the vicinity of the boundary between both, one can apply

$$I_S(2\theta,\omega) = I_{SC}(2\theta,\omega)\frac{1}{A_{S,SC}} - I_C(2\theta,\omega)\frac{A_{C,SC}}{A_{C,C}A_{S,SC}}\,. \tag{4.19}$$

to calculate the scattering of the sample. The correction factors A_i depend on the scattering angle and the energy transfer. $A_{S,SC}$ corrects for neutrons scattered in the sample and absorbed either by the can or the sample. It is noted that absorption includes both the loss in intensity due to real absorption and also due to scattering events. Consequently, $A_{C,SC}$ corrects for processes involving scattering on the can and absorption in either the sample or the can. $A_{C,C}$ corrects for scattering and absorption of the neutrons scattered exclusively in the can. The correction factors are calculated by summation of a product of exponential functions with an exponent consisting of the absorption length and an optical path length of the incoming and scattered neutron beam. The summation is done over the whole cylinder area. Pt is only a weak scatterer and a rather strong absorber. Thus in first approximation the factors $A_{C,SC}$ and $A_{C,C}$ are set to unity. For calculating the factor $A_{S,SC}$ a combined scattering and absorption cross section for the sample and the Pt can is used. The intensity of the empty Pt container is subtracted of the combined scattering intensity of the sample and the can weighted with the factor $A_{S,SC}$.

The correction factors are shown versus scattering angle 2θ in the left graph of figure 4.6 for two different sample geometries. The solid line representing a cylindrical sample features only minor angular dependence, whereas the dashed line representing corrections for a flat plate geometry depends on scattering angle in a non negligible way. The calculation was performed for a plate orientation of 135° to the incoming neutron beam as used in our experiments on the iron bearing silicate samples. According to the correction factor the intensity measured at zero energy transfer is by 40 % lower compared to its expected value. The main reduction arises owing to the rather strong absorber Pt. For the flat glass plate it is only a 8 % effect. In the right graph of figure 4.6 the correction factor is depicted versus energy transfer for an intermediate scattering angle. For the flat plate the correction factor features only a minor energy dependence. For the hollow cylindrical sample already around zero energy transfer in the range of ± 1 meV a 10%

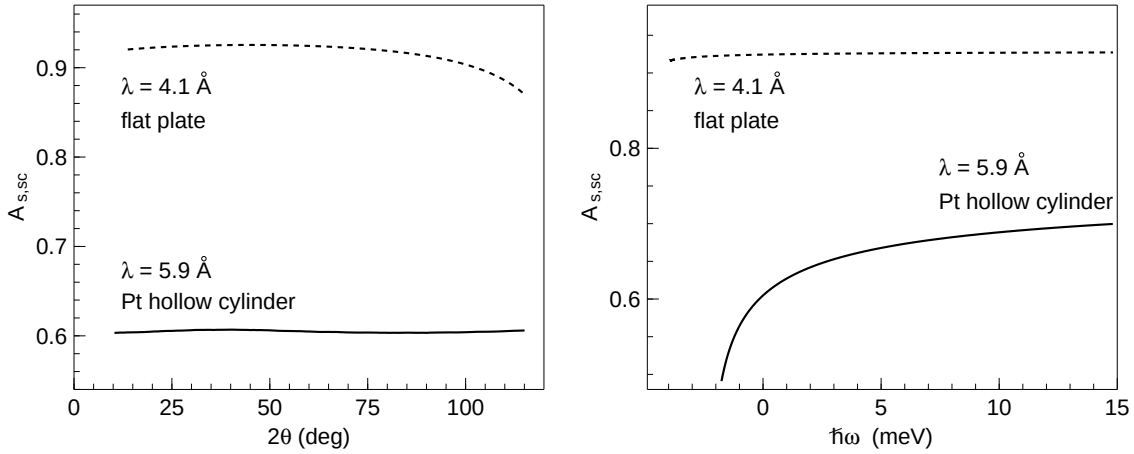

Figure 4.6: Correction factor $A_{S,SC}$ calculated according to Paalman and Pings for a flat glass plate (dashed lines) and a glass contained in a Pt hollow cylinder (solid line). Data were calculated for 4.1 Å and 5.9 Å incoming wavelength, respectively. The left graph exhibits the correction factor for zero energy transfer versus scattering angle 2θ. The right graph shows its energy transfer dependence for an intermediate scattering angle of 60 °.

change in the correction factor is observed. It strongly decreases in the negative energy transfer range. We note that the slower the neutrons are the higher is the probability for absorption which leads to a reduction of the measured intensity.

Multiple scattering can be neglected since typical scattering powers of the sample investigated did not exceed the 8% mark [Wut00]. If multiple scattering contributes significantly to the scattering signal the linewidth of the elastic peak is affected. It is comparable to a quasielastic signal. However, the linewidth of a suggested quasielastic signal due to multiple scattering exhibits a characteristic dependence of the linewidth with q. Moreover it effectively spoils the data only at small wavenumbers.

The focus of our work is directed to the analysis of the elastic and quasielastic part of the scattering signal. The investigation of the latter was the main intention of the work presented here. Multi-phonon contributions are more pronounced at larger energy transfers. Thus despite of a horizontal background no significant contributions to the scattering law is expected in the energy range analysed in this study.

Finally, $S(q,\omega)$ is calculated from the corrected $S(2\theta,\omega)$ by interpolation of the latter to constant wavenumbers q. At low temperatures the detailed balance factor (3.5) has substantial influence on the scattering law. At high temperatures the detailed balance factor imposes only minor corrections on the scattering law.

After these corrections the scattering law $S(q,\omega)$ is still convoluted with the instrumental energy resolution function.

There are two possibilities to analyse the data. Both have been shown to be equivalent with respect to the obtained results. They were rigorously tested using functions allowing for an analytic solution. Neutron backscattering data presented in this work were analysed by means of the first method, whereas time-of-flight data were analysed by

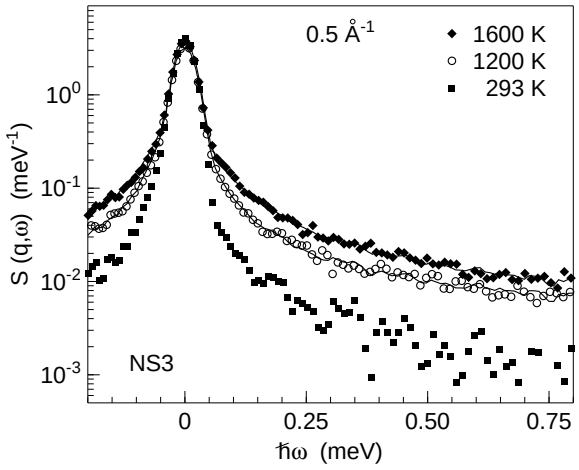

Figure 4.7: Scattering law $S(q,\omega)$ of NS3 measured at IN6. The measured data are represented by points. The solid line represents a fit with the sum of the Fourier transform of a stretched exponential function and a delta function. Both were convoluted with the instrumental energy resolution function $S(q,\omega)(293\,\mathrm{K})$. Energy gain is contrary to the conventional rule assigned with a positive sign.

means of the other method.

The measured $S(q,\omega)$ can be directly analysed by performing a fit with a theoretical formula convoluted with the measured instrumental energy resolution function. Using this method the fit parameters have to be chosen relatively close to the global minimum. A possible source of error is the convolution performed on a finite energy range.

The second possibility is to analyse the data in the time regime. An overview of the different correlation functions calculated obtained from the experiments is shown in figure 4.8.

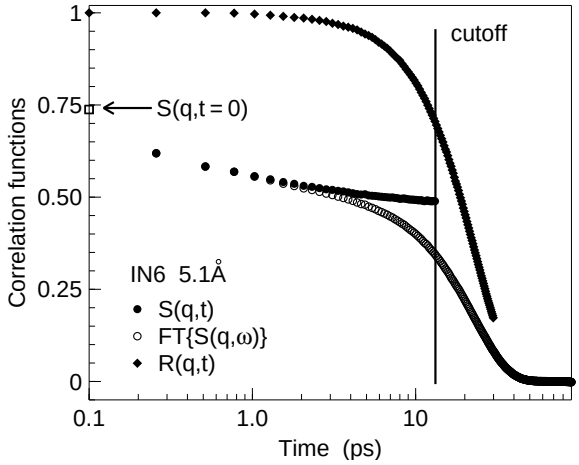

Figure 4.8: Correlation functions calculated from experimental data obtained on IN6 at 5.1 Å incoming neutron wavelength at $q = 1.3$ Å^{-1}. The solid line gives the cutoff based on a decay of the measured resolution function $R(q,t)$ to 70 %. $FT\{(S(q,\omega)\}$ is the Fourier transform of the scattering law. $S(q,t)$ is the density correlation function obtained by simple division of $FT\{(S(q,\omega)\}$ by $R(q,t)$. The open square denotes $S(q,t=0)$.

Fourier transformation of the scattering law and simple division by the Fourier transform of the measured resolution function results in the density correlation function $S(q,t)$. Owing to a fast Fourier transformation on a finite energy range the $S(q,t)$ cannot be properly normalised to unity in the limit $t = 0$. The data are accurate over roughly up to two orders of magnitude. The largest accessible time is determined by the chosen energy resolution. The minimal accessible time is given by the largest energy transfer given by $S(q,\omega)$ for a fixed q value. The Fourier transformation is performed on a finite energy range. Hence, the experimental $S(q,t=0)$ do not exactly correspond to the static structure factor $S(q)$. The cutoff at large times depends on the instrumental energy resolution function. For the spectrometer IN6 using a crystal monochromator for selecting a peculiar

wavelength the resolution function features broad wings around a Gaussian centered at zero energy transfer. A decay of the density correlator in the range of 70% to 75% of its initial value determining the large time cutoff is feasible. Beyond this value the instrumental resolution function dominates the spectra. Division of the Fourier transformed data by means of the resolution function results in oscillations in the data. Chopper monochromated instruments as IN5 provide an almost Gaussian energy resolution. A cutoff is feasible at the point, where the resolution function decays to 50 % of its initial value. Beyond this values as discussed previously the data are dominated by the resolution function.

Chapter 5

Boron oxide based melts

This chapter is devoted to investigations of relaxation processes in B_2O_3 and sodium diborate. A fast relaxation process is observed in the density correlation function. It is consistently described with the universal scaling laws of the mode coupling theory. The fits on the data provide evidence that the structural relaxation of Na is prepared by this fast relaxation process.
The outline of this chapter is as follows. The first section comments on properties of boron oxide based melts. Furthermore, neutron backscattering results on pure B_2O_3, Na_2O-2 B_2O_3 and Na_2O-4 B_2O_3 are presented and compared to viscosity data. The last section focuses on structure and dynamics in sodium borate melts. Changes in the elastic structure factor on intermediate range scale are discussed depending on the Na_2O content.

5.1 General properties and structure

Pure B_2O_3 glass comprises triangular B-O units forming boroxol rings. The boroxol rings are irregularly arranged[1]. The fraction of rings and its temperature dependence is still debated in literature [WrFH96].

The addition of alkali oxides to B_2O_3 leads to a formation of BO_4 units. The network becomes more stable, what is reflected in the increase of viscosity or the calorimetric glass transition temperature. The latter is shown in figure 5.1. Although the formation of tetragonal BO_4 units increases the network strength, it can only partially explain the increase in viscosity. The maximum of the BO_4 content is reached in the vicinity of the diborate composition around 35 mol% sodium oxide content shown by Stebbins in [WrFH96]. Further addition leads to a formation of non bridging oxygen atoms. The latter are shown to be not linked to two B atoms. They have only one network neighbour resulting in a free bond. The extra charge related to this free bond is compensated by an alkali ion. In analogy to non bridging oxygens, the BO_4 units also have an extra charge balanced by an alkali ion.

Borate melts containing alkali oxides feature a wealth of anomalies concerning the be-

[1] A schematic picture taken from literature was already provided in the introduction of this thesis work.

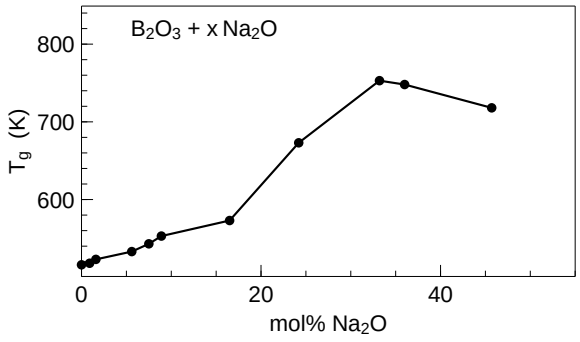

Figure 5.1: Calorimetric glass transition temperature T_g taken from literature data [MaSS85]. T_g is increasing towards a maximum in x Na_2O-B_2O_3 with increasing amount of Na_2O.

haviour of macroscopic properties on control parameters like temperature and composition. Adding alkali oxides to pure boron oxide at a fixed temperature yields an increase in viscosity towards a maximum. This effect can directly be observed in glass transition temperatures on raising the alkali content. The anomalous behaviour is most pronounced at lower temperatures close above the glass transition temperature. It becomes less pronounced with increasing temperature and it vanishes in the melt. The maximum in the viscosity versus concentration diagram does not coincide with the maximum of BO_4 units. Moreover, the maximum in viscosity shifts with increasing temperature to lower concentrations. At sufficiently high temperatures in the melt the addition of Na_2O to B_2O_3 generally yields a decrease in viscosity. The equivalent behaviour holds for the density. In the melt the density first increases to a maximal density due to the addition of alkali oxide to boron oxide. The overall density in the melt is lower compared to the glass. The larger the modifier ion is, the more pronounced is the increase in density and its non linear behaviour.

The anomalous behaviour is not observed in the conductivity which reflects the motion of the charge carrying Na ions. The latter is discussed later in comparison to tracer diffusion data and our quasielastic neutron time of flight investigations.

Immiscibility is only reported for Li_2O–B_2O_3 melts for certain temperatures and Li_2O content by Porai-Koshits in [WrFH96].

In literature alkali bearing boron oxide glasses are reported to comprise more complicated arrangements of the basic network forming units BO_3 and BO_4 [WrFH96]. Different vibrational bands were attributed to the different structures related to these basic building blocks. However, data analysis was not unambiguously identifying the origin of the different vibrational bands which may indeed overlap. Changes in the intermediate range order of the glass are reported to become visible by large differences in the BO_4 stretching modes.

This thesis work focused on the investigation of relaxation processes and elastic structure factors. Energy transfers in μeV to several meV energy range were investigated. We thus probe by means of quasielastic neutron scattering the structural relaxation of the network and of the alkali ions and secondary relaxation processes.

5.2 Structural relaxation in B_2O_3 based melts

The structural relaxation of pure B_2O_3, NB2 and NB4 was investigated by means of neutron backscattering. The experiments were performed on the HFBS (NIST). We investigated the α relaxation in the melt in the temperature range of 1100 K to 1600 K depending on the sample. In pure B_2O_3 the structural relaxation is already to slow at 1100 K to be resolved by a backscattering experiment. We obtained relaxation times for the B-O network at $q = 1.4$ Å^{-1} close to the first sharp diffraction peak (FSDP). According to diffraction experiments the FSDP in the glass is shown at 1.6 Å^{-1} [SwBo98]. The latter work revealed that scattering around the FSDP was dominated by coherent scattering on O.

The scattering law $S(q,\omega)$ obtained by the experiments was fitted with the sum of a Fourier transformed single stretched exponential function reflecting the α relaxation process and a constant reflecting the background. In the background relaxation processes on shorter timescales yielding a linewidth in the several 10 μeV to some meV range are contained as well. During fitting the function was convoluted with the measured instrumental energy resolution function. For B_2O_3 the measured data (points) and the fit curves (solid lines) are shown in figure 5.2. For NB2 the measured data and the fit curves are presented in figure 5.3. For clarity the measured $S(q,\omega)$ are normalized to unity for energy transfer $\hbar\omega = 0$. Oscillations in the fit curve that are visible at larger energy transfers result from the convolution with the measured resolution function reflecting the statistical fluctuations of the data. The latter has no impact on the result as evidenced by using a smooth instrumental energy resolution function. A smooth instrumental energy resolution function was obtained by a fit with the sum of a Gaussian and a constant to the scattering law of the glass. The data was best described with a temperature independent stretching exponent of 0.89 ± 0.08.

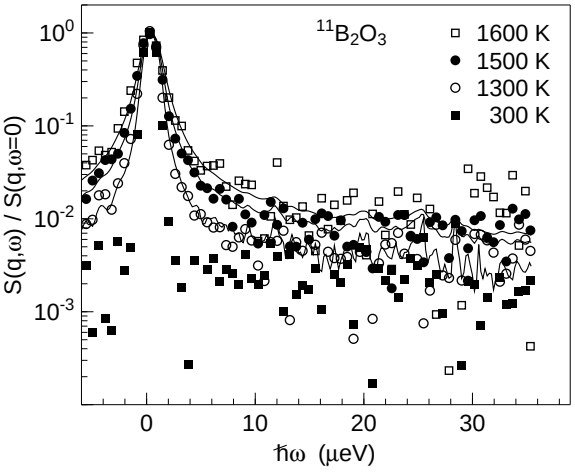

Figure 5.2: Scattering law for molten $^{11}B_2O_3$ obtained on HFBS (NIST). For clarity the measured scattering law was normalized to $S(q,\omega = 0)$. The 300 K spectrum (solid squares) serves as resolution function. The solid lines represent fits with a Kohlrausch function using a stretching exponent β of 0.89.

The fit results in relaxation times in the range of 400 ps up to 10 ns. The latter timescale represents the upper limit of the spectrometer. The relaxation times for NB2, NB4 and B_2O_3 are listed in table 5.1.

A similar analysis was performed on data measured for NB2 and NB4. The inverse

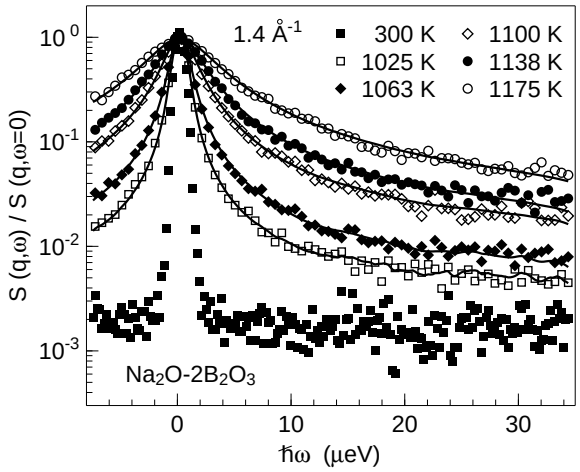

Figure 5.3: Scattering law for NB2 measured on HFBS (NIST). For clarity the scattering law was normalized to unity for energy transfer zero. The solid lines represent fits with the Fourier transform of a stretched exponential function and a constant background convoluted with the measured instrumental energy resolution function (300 K). The fit on the data gives a temperature independent stretching exponent of β equal to 0.78 ± 0.05.

T [K]	1025	1050	1063	1100	1138	1150
B_2O_3	–	–	–	–	–	–
NB2	2.5(3)	–	1.2(3)	0.52(5)	0.34(5)	–
NB4	–	5.3(4)	–	2.0(3)	–	0.95(5)

T [K]	1175	1200	1300	1500	1600
B_2O_3	–	–	6.4(5)	2.5(3)	1.6(3)
NB2	0.21(5)	–	–	–	–
NB4	–	0.50(5)	0.22(5)	–	–

Table 5.1: The relaxation times are given in unities of nanoseconds. They were obtained from a fit to the HFBS data at $q = 1.4$ Å^{-1}. The details of the fit are discussed in the text. The errors are noted in brackets.

temperature dependence of the relaxation rate[2] for pure $^{11}B_2O_3$, NB4 and NB2 are shown in figure 5.4 a). The relaxation rate of $^{11}B_2O_3$ seems to follow an Arrhenius law in the investigated temperature range. Due to signal strength the measurements were restricted to temperatures equal to and above 1300 K. Usually, a non Arrhenian behaviour cannot be distinguished from Arrhenian behaviour deep in the equilibrium melt. The data has to be measured over a larger temperature range covering the equilibrium melt, the supercooled liquid and the glassy state. The latter can only be achieved by viscosity measurements. Data presented in literature clearly features a non Arrhenian behaviour [MaSS85] (see figure 5.4 b)).

The relaxation rates of the sodium borates feature non Arrhenian behaviour on approaching the supercooled liquid region. The solid lines represent fits with the critical scaling law of the mode coupling theory for the relaxation time (see equation (3.24)). The data were obtained at 1.4 Å^{-1} in the first structure factor maximum. We assumed the Kohlrausch exponent β of the fit to be equal to the line shape parameter λ of the critical scaling law of the mode coupling theory. Within error bars we are able to show that this is a fairly good assumption. λ is related to the critical exponents a and b via

[2]The relaxation rate is the inverse of the relaxation time.

equation (3.23). Based on the obtained critical exponents we calculated the scaling factor $\gamma = 1/2a + 1/2b$ entering the α relaxation scaling law. For the fit (solid lines) $\gamma = 2.48$ for NB4 and $\gamma = 2.54$ for NB2 were used as fixed parameters. The fit resulted in a critical temperature of 956 ± 20 K for NB4 and 939 ± 20 K for NB2, respectively. The uncertainties in temperature were estimated by varying λ within the error bars. We have to note that the critical temperature for NB4 is also higher than for NB2 for a fit with γ and T_c as free parameters. The latter fit gives similar parameters for γ and T_c as used for the fit with only one free parameter.

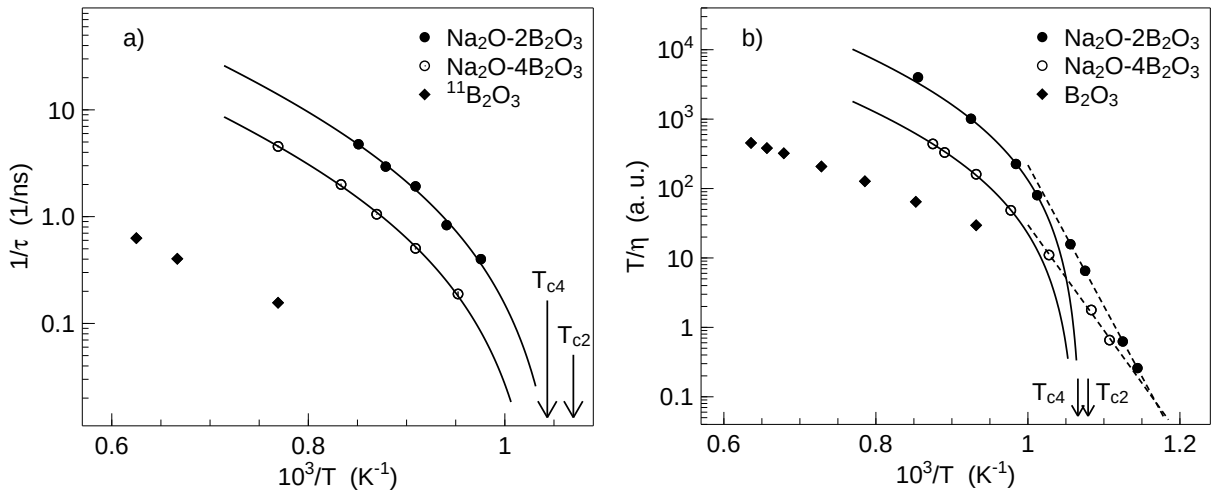

Figure 5.4: a) Relaxation rate $1/\tau$ for $^{11}B_2O_3$, NB4 and NB2 obtained from the fit to the backscattering data. The relaxation rates of the sodium borates behave non Arrhenius like. The relaxation rate is proportional to the diffusion coefficient. b) Viscosity taken from literature data rescaled with temperature. The dashed lines represent fits with an Arrhenius law. In both figures the solid lines represent fits with the critical scaling law of the mode coupling theory for the structural relaxation times (for details see the text). The arrows indicate the critical temperatures obtained from the fit. T_{c2} denotes the critical temperature for NB2 and T_{c4} the critical temperature for NB4, respectively.

Figure 5.4 b) illustrates the inverse of the viscosity η rescaled with temperature. According to the Stokes Einstein relation or to the Eyring equation[3] the diffusion coefficient of a viscous liquid shall be proportional to T/η. The rescaled viscosity features similar behaviour on temperature as the relaxation rate does. The solid lines represent fits with the scaling law of the mode coupling theory. A free fit results in similar lineshape parameters compared to the relaxation rate measured by means of neutron scattering. The critical temperatures determined by viscosity data are within the error bars equal to the critical temperatures obtained from the neutron scattering data.

The correct scaling of viscosity η to an absolute value of the relaxation time is obtained by a constant prefactor comprising the typical lengthscale of the moving subunit and the constraints imposed by the environment. Since in a complex systems this prefactor cannot

[3]Both equations were applied to calculate diffusion coefficients from viscosity data for oxidic melts.

be determined with high accuracy, we present the data in arbitrary units. The overall behaviour on temperature is independent of the prefactor.

Moreover, the difference in the relaxation rate and the rescaled viscosity for different samples at the same temperature are equal within their error bars. This finding corroborates that the applied microscopic technique (neutron scattering) measures the same process as the macroscopic method when determining the viscosity. Neutron scattering on O yields the main contribution to the scattering law. We conclude that breaking of oxygen bonds (B-O) is mainly responsible for viscous flow.

5.3 Structure and dynamics in molten sodium borates

In the following paragraphs we focus on the investigation of sodium borates. Neutron time of flight spectroscopy shall provide access to the structural relaxation of the network modifying alkali ions. According to macroscopic measurements the self motion of the network modifier ions and the network is also in the melt decoupled [MaSS85, ScMe00] Besides structural relaxation, the investigations also look for a fast β relaxation process.

Extensive nuclear magnetic resonance (NMR) studies were performed on alkali borate glasses and melts [GeSt97, InMY93, RaJE98, SeSt97]. In particular, spin lattice relaxation in sodium borates over a wide temperature and concentration range was investigated [SeSt97]. Both the Na relaxation by means of ^{23}Na NMR and the network relaxation by means of ^{11}B NMR were observed. The decoupling of network and modifier spin lattice relaxation times is reported to be more pronounced at larger Na concentrations. At Na_2O contents roughly exceeding 15 mol% the decoupling is already present below the calorimetric glass transition temperature. The main result of their study was the fact, that Na transport features two relaxation scenarios. Below the percolation threshold, predicted to be in the range of 15 mol% to 22 mol% Na_2O content, network and modifier dynamics are strongly coupled. Ion diffusion demands for a reorientation of the network. Beyond the percolation threshold Na transport is more decoupled of the network. A continuous percolation cluster for Na is supposed to exist.

Relaxational spectroscopy performed on borates suggested that modifier cations and network mobilities in the melt are rather similar [KiMR95]. The measurements suggested that a large number of processes involving both the network and the alkali ions are contributing to structural relaxation on slightly different timescales. This reported behaviour contrasts data extrapolated of tracer diffusion measurements performed on Na borates [ScMe00].

According to the NMR experiments sodium diborate investigated in our study is expected to belong to the regime featuring a percolation cluster. The sodium self motion shall thus be clearly separated of the network. However, we expect the decay of the different coherent correlators to be distributed over a large time range with the B-O and O-O relaxation as limiting process. Thus a separation of relaxation processes of Na and the network units will become a difficult task at high temperatures and large wavenumbers.

5.3.1 Intermediate range scale structure in alkali borate melts

Time of flight experiments on sodium borate melts were performed on the spectrometers IN6, IN5 and DCS. The elastic structure factor for NB2 shown in figure 5.5 was obtained by an IN6 experiment. The scattering law was integrated over the instrumental energy resolution function in the range of -0.3 meV to 0.3 meV. The presented data are on an absolute scale and compare well to the static structure factors presented in [SwBH98].

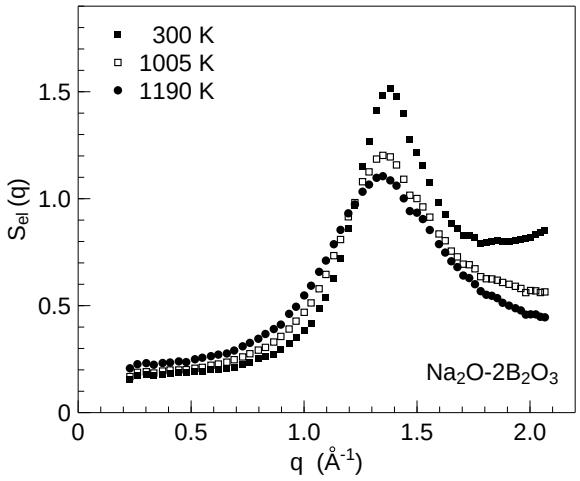

Figure 5.5: Elastic structure factor of NB2 measured on IN6 using an incoming wavelength of 5.1 Å. The first sharp diffraction peak around 1.4 Å^{-1} decreases on the Debye-Waller factor when increasing temperature. The broadening of the peak with increasing temperature reflects growing disorder and thermal fluctuations of the structure.

We reproduce in the elastic structure factor a first sharp diffraction peak (FSDP) around 1.4 Å^{-1}. With increasing temperature the elastic structure factor decreases on the Debye-Waller factor. The FSDP broadens with increasing temperature. In addition, its position slightly shifts to smaller momentum transfers reflecting changes in the density. The broadening mirrors a more pronounced disorder with increasing temperature.

In sodium borates the main contribution to the coherent signal is given by B and O. Averaged with their relative abundance in the sample the ratio of coherent cross sections Na < B < O behaves $\sim 1 : 7 : 9$. At small wavenumbers an almost flat background is observed in $S_{el}(q)$ (see figures 5.5 and 5.6). The different scattering processes contributing to the scattering in this momentum transfer region were already discussed in section 3.1.3. We shortly note that besides reflecting the compressibility κ_T of the sample in the limit $q \to 0$, a flat background in the structure factor indicates incoherent scattering. The ratio of the incoherent cross sections of NB2 for Na and B is approximately four. The incoherent cross section of O is negligible. Contributions of the compressibility were estimated below 0.1 on an absolute scale. Thus incoherent scattering on sodium dominates the scattering law at small momentum transfers, whereas at large momentum transfers coherent scattering on O dominates.

For NB4 the behaviour of the elastic structure factor is substantially different (see figure 5.6). NB4 measured on DCS (NIST) features a double peak structure of the first sharp diffraction peak in the glass vanishing in the equilibrium melt. The behaviour is reproduced upon cooling from the melt to the glass. Room temperature data was only measured for six hours compared to the 12 hour measurements for the melt. This explains the slightly worse statistics for the 300 K data. At present no answer on the

origin of this double peak in the elastic structure factor can be provided. However, we can rule out a phase separation, since to the best of our knowledge no indication for such a process was found in literature by means of other investigations on sodium borate samples [HaKK99, MaCC03].

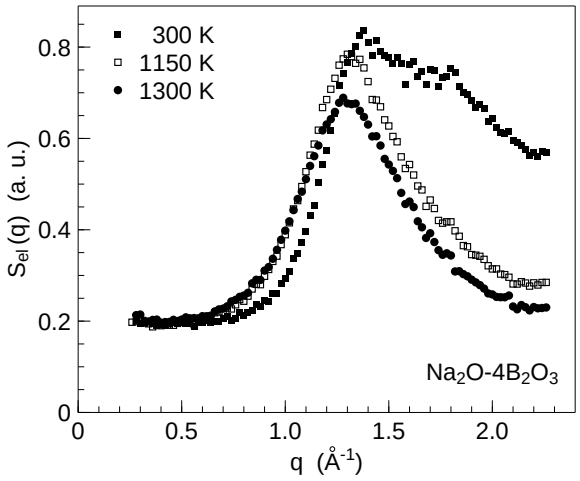

Figure 5.6: Elastic structure factor of NB4 measured on the instrument DCS (NIST). For the measurement an incoming wavelength of 5.0 Å was used. NB4 features a double peak at ambient temperatures in the glass. Besides the decrease with increasing temperature due to the Debye-Waller factor the double peak vanishes.

5.3.2 Mode coupling scenario in Na_2O-2B_2O_3

The main attention of our investigations on sodium borate melts was devoted to the microscopic dynamics. Already the neutron backscattering and viscosity data provided a hint for a mode coupling scenario in these network glass formers. The central issue deals with the possibility of observing in $S(q,t)$ a fast β relaxation process preparing the structural relaxation upon approaching the supercooled liquid region. Moreover, interest is drawn to the question whether such a process is consistently described within the framework of the mode coupling theory of the liquid to glass transition by applying the universal scaling law.

Liquids that exhibit a similar dependence of viscosity upon temperature like the sodium borates and pure boron oxide usually feature a pronounced Boson peak. Typically the Boson peak is located in the range of 1 THz in light scattering experiments corresponding to roughly 4 meV. If present in a neutron scattering experiment this distinct peak will lead to oscillations in the density correlation function that can not be properly corrected for.

Recent light scattering experiments on a number of sodium borate glasses showed the Boson peak intensity to decrease on increasing Na_2O content [BaPP00]. Comparison of neutron and depolarized light scattering data feature no significant shift in the Boson peak position by varying the method of investigation [BrBE96, EnWB98]. In the light scattering experiments the Boson peak in NB2 is shown to be located around 7.5 meV with an estimated HWHM of 2 meV. Thus it is far enough separated from any quasielastic scattering contribution observed in our experiments. In contrast depolarized light scattering experiments on pure B_2O_3 showed that the Boson peak makes the analysis of the susceptibility in the framework of the mode coupling theory a difficult task [BrBE96]. In our experiment on NB2 we observe no distinct feature in $S(q,\omega)$ in this energy transfer

range that can be attributed to a Boson peak. Thus data analysis in terms of Fourier deconvolution can be readily applied.

As already mentioned the scaling laws of the mode coupling theory were applied to systems that feature one single structural relaxation time for the different components in the melt. In sodium borate melts the structural relaxation times of the network and the Na atoms in the temperature range of our investigations shall be still separated by one to two orders of magnitude. The separation naturally depends on the particular wavevector and the particular temperature, respectively. An overview of different relaxation processes and how the density correlation functions evolves with wavenumber is shown in the schematic representation of measured data and theoretical curves in figure 5.7.

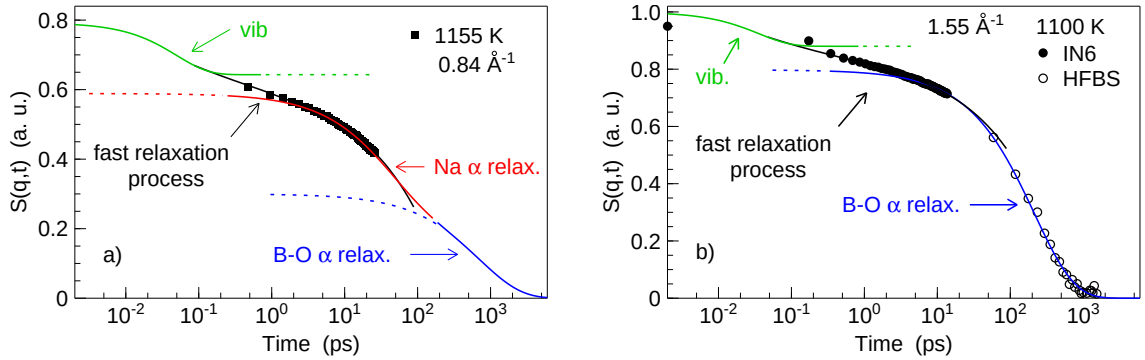

Figure 5.7: Density correlation function for NB2. The solid symbols (filled squares and circles) represent data obtained on IN6 for two temperatures. The open circles represent data obtained on HFBS. Different processes are illustrated by solid lines presented in different colours. The decay of the density correlation function due to vibrations is sketched by the green line. We note that it gives not an accurate description. The solid black lines represent a fit with the universal scaling function of the MCT. It is discussed in detail later in this chapter. a) Data is shown for 1155 K and 0.84 Å^{-1}. The timescale of the network α relaxation was estimated based on viscosity data. b) The density correlation function is shown at 1100 K and at 1.55 Å^{-1}. The α relaxation is described by fit to the experimental data. Here scattering on O mainly contributes to the signal.

For clarity the density correlation function is shown in figure 5.7 a) at 1155 K. At this temperature the Na relaxation is fast enough to be clearly visible in the experimentally accessible time window on IN6. The data is presented at an intermediate wavenumber of 0.84 Å^{-1}. Consequently, it comprises coherent and incoherent scattering contributions. We note that the amplitude of the blue line may vary by up to 30%. The timescale of the relaxation was estimated from our neutron backscattering experiments and is properly defined.

Relaxation times expected for Na in NB4 and NB2 can be estimated on the basis of macroscopic measurements. Sodium tracer diffusion measurements that directly probe the self diffusivity of Na were presented in [ScMe00, ImVM02]. Extrapolation to temperatures in the range of 1000 K to 1200 K results in diffusivities in the range of $10^{-10}\,\text{m}^2\,\text{s}^{-1}$ to $10^{-9}\,\text{m}^2\,\text{s}^{-1}$. These values are comparable to Na diffusivities D_σ calculated from conductivity data using the Nernst-Einstein relation. The values for the conductivity and

densities that are necessary to calculate the self diffusivities were taken from the work of Kostanya (1958) and Nagel (1973) [MaSS85], respectively. We note that in the melt diffusivities calculated from conductivity data do not exactly correspond to the real value of self diffusion. A correction factor, the so-called Haven ratio, has to be applied to D_σ. The latter factor is constant in the glass and not necessarily constant in the melt. However, considering a Haven ratio slightly smaller than unity, the calculated values agree well with tracer diffusion data.

Typical relaxation times for Na in the melt can be derived from diffusivities. Assuming a q^2 scaling of the relaxation rate for the smallest wavenumbers, we calculate a relaxation time of the order of ten picoseconds for $q = 0.5\,\text{Å}^{-1}$. For this wavevector incoherent scattering dominantly contributes to the signal. Thus such a relaxation process shall be clearly visible in a neutron time of flight experiment on NB2.

As stated earlier, the ratio of the incoherent scattering contributions on Na and B in NB2 compare like four to one. We estimated on an absolute scale the contribution of the compressibility to the scattering law as 0.1 or less. Considering the measured elastic structure factor of NB2 (figure 5.5) incoherent scattering on Na contributes in the range of roughly 20% to 25% to the total relaxation amplitude in the density correlation function. Based on the latter estimation a fit can be performed on the measured density correlation

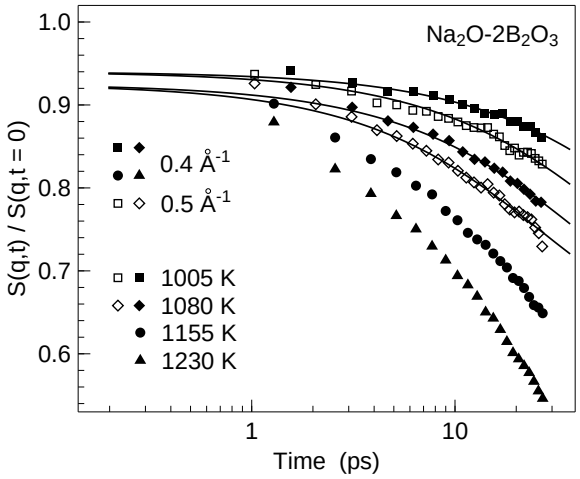

Figure 5.8: Density correlation function measured on IN6 with 5.9 Å incident neutron wavelength. Data are presented for 0.4 Å^{-1} (solid symbols) and 0.5 Å^{-1} (open symbols). The data is shown for four different temperatures. Solid lines are fits with $b + a\exp -(t/\tau)^\beta$. For the fit the amplitudes a and b were fixed as explained in the text.

function at around 0.5 Å^{-1}. The fit was performed with a constant relaxation amplitude a and a fixed Debye level for the α relaxation decay of the Na self correlator. We assume other relaxation processes (coherent and incoherent) to contribute on longer timescales well separated of the decay of the incoherent Na correlator. The obtained relaxation times are accurate within an error of 30%.

The fit yields $\tau = 122\,\text{ps}$ and $\tau = 45\,\text{ps}$ at 0.4 Å^{-1}, $\tau = 68\,\text{ps}$ and $\tau = 30\,\text{ps}$ at 0.5 Å^{-1} for 1005 K and 1080 K, respectively. The stretching exponent can be varied by ~ 0.08 around a mean value of 0.82.

The fit procedure can only be applied on density correlation functions measured at temperatures below 1100 K. Above coherent processes and incoherent scattering on B must already contribute to the density correlation function measured in our experiments

as evidenced in figure 5.8. Based on the obtained relaxation times diffusivities D_{Na} were calculated applying the q^2 law for simple diffusive behaviour. The diffusivities D_{Na} coincide within error bars with D_σ.

At larger wavenumbers no clear distinction of the different relaxation process (coherent and incoherent) can be made. As already shown in figure 5.7 two, in time not clearly separated processes, cannot be distinguished from a single relaxation process. Moreover, in figure 5.7 a fast relaxation process evidenced by a power law behaviour is observed. This process will be discussed in the following paragraphs. It is shown that this process can consistently be described in the framework of the mode coupling theory.

The density correlation functions of NB2 for different wavenumbers and temperatures are presented in figure 5.9. The investigations were performed over a large wavenumber range for six different temperatures. In order to probe instrumental artifacts and artifacts related to the Fourier deconvolution procedure two different incident neutron wavelength were used. The data analysis was performed independently yielding the same result.

The data set roughly comprises 100 measured density correlation curves that shall allow to probe for the scaling laws of the mode coupling theory and their constraints on the fit parameters.

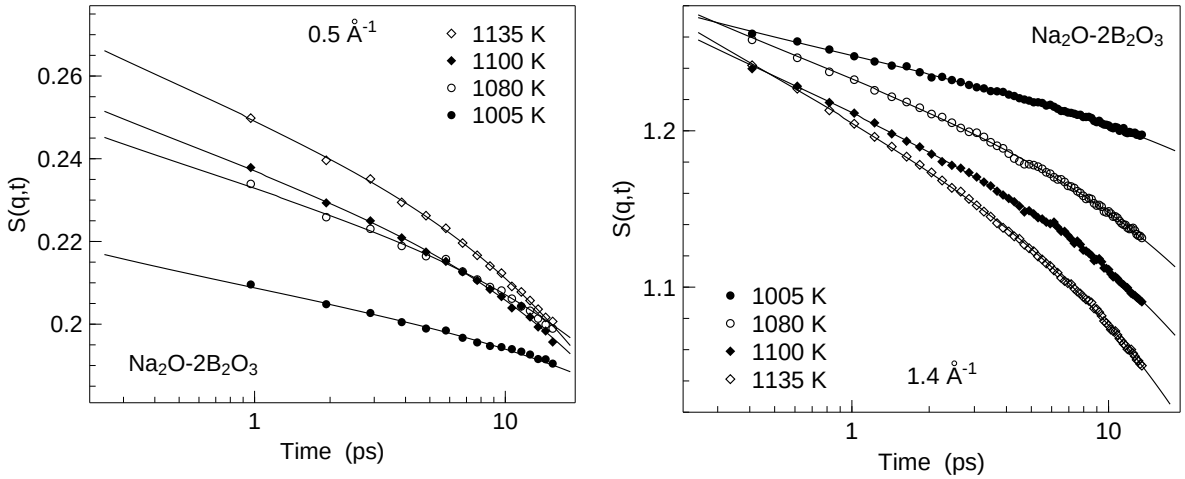

Figure 5.9: Density correlation function for NB2 measured on IN6 using the incoming neutron wavelength 5.1 Å. The data are shown for four different temperatures in the melt approaching the supercooled liquid range. The solid lines represent fits with the MCT scaling law (see equation (3.17)). A fast β relaxation process that prepares the structural relaxation is observed. The process is increasing in magnitude with increasing temperature and wavenumber.

In figure 5.9 the measured $S(q,t)$ is shown for 5.1 Å incident neutron wavelength. The solid lines represent fits with the β scaling law of the mode coupling theory

$$S(q,t) = f_q + h_q \cdot g_\lambda(t/t_\sigma) \tag{5.1}$$

discussed already in the theoretical part of this thesis. A completely free fit yields four parameters for the fit function. However, mode coupling theory makes detailed predictions for the temperature and wavenumber dependence of the fit parameters. Fitting of the

measured $S(q,t)$ with the universal scaling functions of the MCT yields a consistent description of the large experimental data set.

At the beginning of the fit procedure we estimate a reasonable lineshape parameter λ as start value. The Debye-Waller factor f_q used as start value is derived from the elastic structure factor. The start value of the transition time t_σ is estimated based on the measured density correlation function. $S(q,t)$ at intermediate wavenumbers yields the start value for h_q. In a first run the fit is performed with four free parameters over a constant time range. Since the fit parameter λ featured no clear dependence on wavenumber, we estimated a mean lineshape parameter λ. For this purpose the mean value of λ was taken from the fit on different temperatures. For further fitting λ is kept constant. The assumption of a temperature and wavevector independent lineshape parameter λ that describes the measured scattering law is based on the strong coupling of the different components contributing to the structural relaxation processes in the density correlation function. Strong coupling is a necessary condition of mode coupling theory to be applicable.

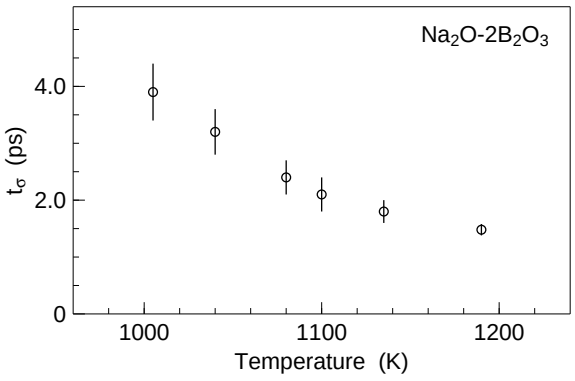

Figure 5.10: Transition time t_σ obtained from the fit on the density correlation function with λ fixed to 0.78. The crossover from the fast β relaxation process to the process of structural relaxation is observed on a picosecond timescale. The transition times are to short to reflect the network relaxation. Na transport is also prepared by this fast relaxation process.

Further fitting yields the transition time t_σ for each temperature. Fitting the data with a fixed λ no pronounced dependence of the transition time t_σ on the wavevector q was found for a particular temperature. We can thus limit the number of free fit parameters to only two, the Debye-Waller factor f_q and the critical amplitude h_q. The fixed t_σ used for further fitting of the data are shown in figure 5.10.

The data is described by using a wavenumber and temperature independent lineshape parameter $\lambda = 0.78 \pm 0.04$. The transition time t_σ for a given temperature was fixed independent of the wavenumber q. Values of t_σ used for the fit are shown in figure 5.10. The error bars were estimated by performing fits on $S(q,t)$ by varying t_σ. The two free fit parameters are the critical amplitude h_q and the non ergodicity parameter f_q. The wavenumber dependence of f_q obtained from the fit is shown for two different temperatures in figure 5.11. For comparison the elastic structure factors are plotted as solid lines. The difference in the absolute value of both data is given by the fact that f_q is obtained for the time t^* that is slightly larger than the transition time t_σ for the chosen λ. The integration over the elastic line does not take into account part of the fast relaxation as the fit on $S(q,t)$ does. However, the q dependences of f_q and $S_{el}(q)$ coincide.

The critical amplitude h_q that is a measure, how strongly pronounced this fast β relaxation process is, is shown in figure 5.12. The critical amplitude increases with raising

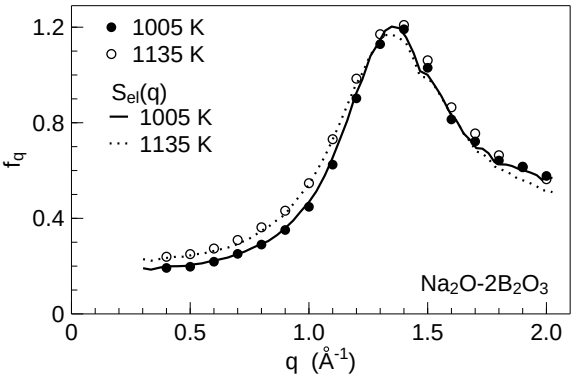

Figure 5.11: Non ergodicity parameter f_q determined by fitting $S(q,t)$ with the MCT scaling law of equation (3.17). It is represented by the open and closed circles for two different temperatures. The solid and dashed line represent the corresponding elastic structure factors calculated from the measured $S(q,\omega)$. f_q is reflects the behaviour of the elastic structure factor $S_{el}(q)$. Error bars are not exceeding the symbols size.

wavenumber, as it is expected for a fit to a not normalized density correlation function. Moreover, it features the expected in-phase behaviour with the structure factor of NB2. However, we can not provide an accurate answer whether the additional intensity due to the in-phase behaviour with the structure factor is either dominated by coherent Na contributions or network contributions. It is worth noting that the critical amplitude decays more slowly towards zero in the limit of small wavenumbers as it is expected for a β relaxation process, to that only the B-O network contributes. The data indicate that at least partly if not entirely the α relaxation of Na is prepared by this fast relaxation process.

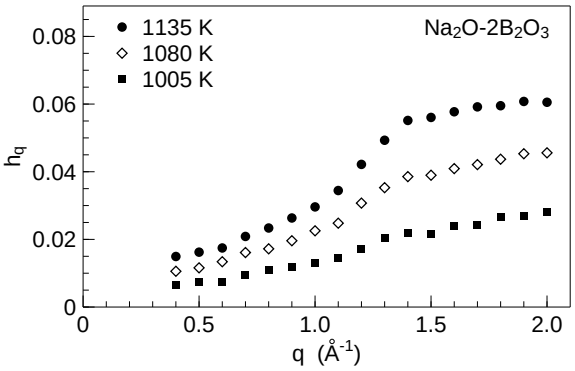

Figure 5.12: Critical amplitude h_q depending on the wavevector q and the temperature T. The amplitude was obtained by fits with the critical scaling law of the mode coupling theory. The amplitude is increasing with increasing temperature and wavenumber. It features a oscillation in phase with the structure factor. Also for h_q the error bars of the fit do not exceed the symbol size.

Additionally, the critical amplitude is increasing with increasing temperature. The temperature dependence of the squared critical amplitude shall follow a critical scaling law. The latter quantity is shown for three different wavenumbers in figure 5.13. h_q^2 features a linear behaviour with increasing temperature. We observe deviations for the highest temperatures, that can be attributed to the fact that the measurement is quite far away from the critical temperature $T_c = 980 \pm 20\,\mathrm{K}$. The latter is determined by a linear fit that is represented by the straight lines. Götze gave a estimation for the validity of the scaling equations up to ~ 100 K above the transition. Thus for the highest measured temperatures deviations are already expected to occur. At different wavenumbers the scattering is dominated by different components. At 0.5 $\mathrm{Å}^{-1}$ incoherent scattering on Na contributes mainly to the scattering law. At intermediate wavenumbers around 0.9 $\mathrm{Å}^{-1}$ we have both coherent and incoherent contributions of Na and coherent contributions of B-O with approximately similar strength. At 1.4 $\mathrm{Å}^{-1}$ that corresponds to the position of the first sharp diffraction peak, the signal mainly results from coherent scattering on O.

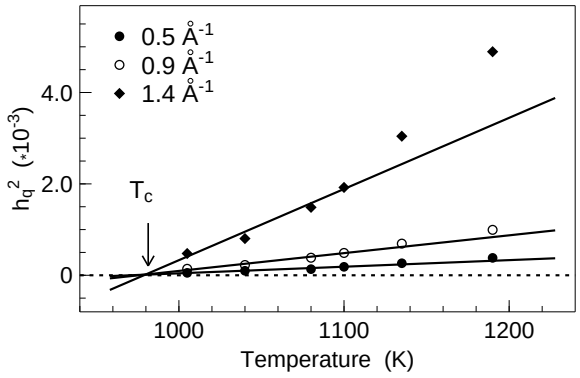

Figure 5.13: Following the mode coupling approach the squared critical amplitude h_q of the fast β relaxation is shown here. The solid lines represent fits with a straight line. The intersection with the T-axis marked by the vertical arrow gives the critical temperature T_c of 980±20 K.

However, we observe h_q^2 extrapolating to the same critical temperature T_c independent of q.

The data indicate that the structural relaxation of the more mobile Na ions is prepared by a fast β relaxation process. A more pronounced coupling of the Na on the network motion in the melt suggested in literature is corroborated by our experimental findings on the relaxation timescales.

The experiments clearly show a fast β relaxation process in molten sodium diborate. A consistent description of this process was given by applying the universal scaling laws of the mode coupling theory. A critical temperature was derived that is about 100 K below the melting temperature and about 250 K above the calorimetric glass transition temperature. It does not coincide with the critical temperature derived by applying the critical scaling law on the α relaxation times of the network. This can be taken as further hint that only the structural relaxation of Na is prepared by the fast β relaxation process observed in the time of flight experiments.

Chapter 6

Silicate glasses and melts

This chapter is devoted to mixtures of the network former silica and alkali oxides. We show that binary alkali silicates comprise a network of channels for fast ion conduction. Adding a second network forming component yields ternary compositions that are discussed in the last two sections of this chapter. In section 6.1 binary alkali silicates are presented. The investigation of their structure and dynamical behaviour is extended to mixed sodium potassium silicate melts in 6.2. In section 6.3 the impact of Al_2O_3 on melt structure is discussed. Changes in the melt structure lead to a slowing down in the alkali dynamics owing to a disruption of the channel structure. In the last section first experiments on iron bearing sodium silicate glasses and an iron bearing sodium silicate melt are discussed. Neutron scattering is shown to provide access to correlations of Fe atoms by studying the spin dynamics and spin correlations of Fe^{3+} contained in these glasses.

6.1 Alkali silicates

We start the discussion of binary alkali silicate melts by providing an overview of literature data about their properties. Afterwards, we focus on the investigations of the relaxation dynamics in these melts. Finally, the structure factors for different compositions - sodium, lithium and potassium silicate melts - are discussed. Experimental evidence is provided for a network of alkali rich channels in the static structure.

6.1.1 Properties of molten alkali silicates

Alkali silicates consist of two components, the network former silica and the network modifying alkali oxide. Pure amorphous silica forms a disordered network made of tetrahedral SiO_4 units. Si atoms are covalently bound via oxygen. These bonds are rather strong, what is reflected in various properties like its large viscosity at ambient temperatures, its high melting point and a rather high glass transition temperature T_g of 1500 K. Moreover, the thermal expansion coefficients of SiO_2 is about two orders of magnitude smaller compared to pure B_2O_3 and about one order compared to GeO_2, respectively. The latter also holds for the corresponding melts comprising alkali ions.

Adding alkali oxide to pure SiO_2 leads to a huge decrease in viscosity for a given temperature. Consequently, the calorimetric glass transition temperature for binary alkali

silicates is in the range of 2.5 mol% to 40 mol% reduced by a factor of ~ 2 compared to that of pure SiO_2. The viscosity at typical melt temperatures of 1200 K to 1600 K is by about eight orders of magnitude smaller compared to pure silica (see figure 6.1). The viscosity of sodium silicate melts, representative for all other binary alkali silicate melts, is shown in this figure. The viscosity varies within a large range of sodium concentration (from about 5 mol% to 40 mol% Na_2O content) only within one order of magnitude. The modifier ion motion is substantially faster as evidenced by means of tracer diffusion and conductivity measurements discussed later in this section.

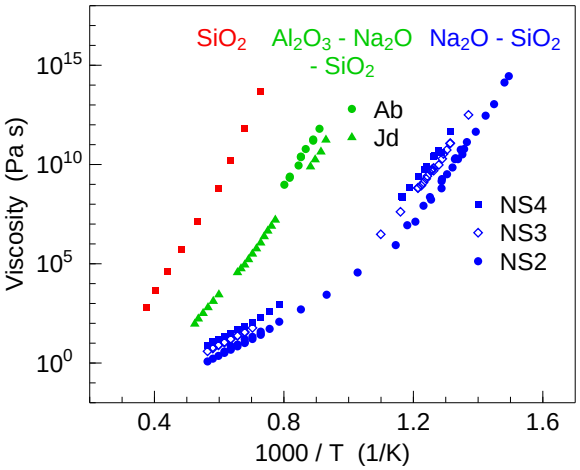

Figure 6.1: Arrhenius diagram illustrating the viscosity of pure SiO_2 (red), three different sodium silicate melts (blue) being subject to investigation and two ternary sodium aluminosilicate compositions (green) discussed in section 6.3. The viscosity exhibits a huge decrease upon adding Na_2O. Furthermore, it increases by orders of magnitude upon adding Al_2O_3 to the binary alkali silicates.

The observed macroscopic properties that crucially depend on the alkali oxide content were not explained by a first model. It assumed a rather homogeneous distribution of alkali atoms in the remaining silica matrix [Zac31]. Based on EXAFS measurements and computer simulations ideas of an inhomogeneous distribution of alkali atoms in pathways were proposed [AnCT82, Gre85]. Recent molecular dynamics simulations corroborated the latter ideas [HoKo99, HoKB02]. Moreover, they provided strong hints for an alkali rich network of channels embedded in the SiO_2 matrix. In contrast to other MD simulations [OvSa98, JuKJ01, JuKJ02, LaKH03], Horbach and coworkers provide evidence that this network of channels is not only a dynamical feature, but it is present in the glass as well. This can also explain the fast alkali ion conduction in these glasses. Horbach and coworkers also point out that a prepeak in the elastic structure factor at values below the FSDP in pure silica of 1.6 $Å^{-1}$ reflects typical interchannel distances. This prepeak was not reflected in experimentally measured static structure factors [WaSu77, MiPS80]. Recently, a neutron time of flight experiment performed on sodium disilicate yielded a prepeak emerging with increasing temperature in the elastic structure factor [MeDS02]. However, the temperature dependence and the absolute value of the prepeak did not coincide with the result of the simulations. We demonstrate in the present work, that the difference between the data and the simulation results from the fact that the latter were performed at constant density conditions. Performing a simulation at experimental densities, Horbach and coworkers showed recently that the prepeak behaviour on temperature found in our neutron scattering experiments can be matched by the simulation [MeHK04].

The main aim of the work on alkali silicate melts is to provide experimental evidence of the proposed network of alkali rich channels. Moreover, a comparison with sodium

borates features inherently different dynamics in the alkali silicates. The latter can be attributed to the channel structure and the alkali modifier atoms that are weaker bound to the network in alkali silicates. Both are the basis of a more pronounced decoupling between network and modifier ion relaxation in alkali silicates compared to alkali borates. Alkali ions in alkali silicates feature no fast β relaxation at melt temperatures up to 1600 K preparing their α relaxation.

6.1.2 Microscopic dynamics and mass transport

Investigations of mass transport performed so far were based on two techniques, the radio-tracer technique and conductivity measurements. In the melt many investigations were performed on the diffusion of the alkali modifier ions and only few tracer diffusion measurements on oxygen diffusion. The latter is discussed later on.

Calculated diffusion coefficients from conductivity data [Tic67] and tracer data [GuKi67] are shown in the following table.

	D_0 [m^2/s]	E_a [eV]	sample	temp. range [K]
Gupta	$2.29\pm 0.22 \cdot 10^{-7}$	0.54 ± 0.02	NS2	1123 - 1773
	$4.67\pm 0.72 \cdot 10^{-7}$	0.70 ± 0.03	NS3	1123 - 1773
Tickle	$4.49 \cdot 10^{-7}$	0.49	LS2	1323 - 1573
	$3.80 \cdot 10^{-7}$	0.48	NS2	1173 - 1673
	$2.14 \cdot 10^{-7}$	0.44	KS2	1373 - 1673
	$5.90 \cdot 10^{-7}$	0.65	KS3	1173 - 1473

Table 6.1: Tracer diffusion experiments on alkali silicate melts were performed by Gupta[GuKi67]. Tickle measured the conductivity of numerous silicate melts [Tic67]. The temperature range indicates the range of validity of the data.

Tracer diffusivity investigations on two compositions were presented in [GuKi67]. The obtained diffusion coefficients follow an Arrhenius behaviour within the experimental error

$$D = D_0 \exp\left(-\frac{E_a}{k_B T}\right) , \tag{6.1}$$

with the activation energy E_a and the Arrhenius amplitude D_0. The data of Tickle was obtained for similar temperatures like the tracer data by Gupta. Data of Gupta compares to data of Frischat and coworkers [BrFr88]. Performing also experiments under microgravity conditions these authors showed that Na diffusivities in sodium silicates melts are not greatly influenced by convection. Their experiment results in $D_0 = 9.2 \pm 5.0 \times 10^{-7}\,\mathrm{m^2\,s^{-1}}$ and $E_a = 0.74 \pm 0.03\,\mathrm{eV}$ for NS3 above 973 K.

Assuming a q^2 dependence of the relaxation rate expected for long range diffusion relaxation times in the range of 10 ps are expected at typical wavenumbers of 0.5 $Å^{-1}$ to 1.0 $Å^{-1}$. A relaxation process on these timescales shall become visible in a time of flight experiment.

Tracer diffusion experiments directly reveal the macroscopic self diffusion coefficient D_t of a tracer ion. Additionally, a self diffusion coefficient can be calculated from conductivity data via the Nernst-Einstein relation

$$D_\sigma = \frac{RT}{CZ^2F^2\rho_{dc}}\,. \tag{6.2}$$

The charge of the mobile ion contributing to the conductivity is denoted by Z (unity for Na^+ ions). R is the molar gas constant, F the Faraday constant, C the concentration of charge carriers in $[\mathrm{mol\,m^{-3}}]$ and $\rho_{dc} = 1/\sigma_{dc}$ the specific resistivity in the dc limit. For the calculation the dc conductivity σ_{dc} that is the low frequency limit of ac conductivity measurements is used. The Nernst-Einstein relation can be directly applied in case of only one kind of ion participating in the conduction process. This holds in binary sodium silicate melts. Diffusion coefficients obtained from conductivity data compare well to tracer diffusivities except the Haven ratio. It is defined as D_σ/D_t and is smaller than unity in case of the binary silicates. For glasses the Haven ratio is temperature independent, whereas in the melt a slight variation is observed. Macroscopically, it is only determined by a comparison of tracer and conductivity data. At present, there is no model available that allows for its estimation. Diffusion coefficients calculated based on conductivity data only allow for an estimation of the timescales of the relaxation process. Only tracer diffusion data that directly measures the self diffusivity can be compared with our microscopic measurements.

In order to estimate the timescale of the slowest relaxation process, i. e. its diffusion coefficient, one can apply the Stokes Einstein relation to viscosity data. The slowest relaxation process in the investigated network glass forming melts clearly is the relaxation of the Si-O network owing to the strong covalent bonds between adjacent SiO tetrahedra. Using the Stokes Einstein relation the diffusion coefficient reads

$$D = k_B T/(6\pi\eta r)\,, \tag{6.3}$$

where η denotes the viscosity and r a typical radius of the relaxing particle. Using the ionic radius of oxygen of 1.2 Å, we obtain diffusion coefficients in the range of $1{\cdot}10^{-12}\,\mathrm{m^2/s}$. The latter corresponds within the same order of magnitude to diffusion coefficients obtained by means of oxygen tracer diffusion [OiTU75]. A naive calculation of relaxation timescales that uses the q^2 approximation and neglects coherence effects yields values in the 10 nanosecond range at $q \simeq 1.6\,\mathrm{Å^{-1}}$ and 1600 K. This relaxation process shall thus become experimentally visible in a neutron backscattering experiments at a temperature of 1600 K. This was already proved in an earlier measurement on NS2 on the backscattering spectrometer HFBS [MeDS02].

Figure 6.2 provides an overview of the different relaxation processes in alkali silicate melts. The density correlation function is shown over four decades in time. It was obtained by matching backscattering and neutron time of flight data measured on HFBS and IN5 at 1600 K. The backscattering data is taken from a recently performed experiment[1], whereas

[1]We Fourier deconvoluted the backscattering data presented in [MeDS02]. We note that Fourier transformation of a data set that is strongly restricted in energy results in substantial errors for $S(q, t = 0)$. However, the latter only minor affects the schematic representation.

the IN5 experiment was performed during this thesis. The solid line represents a fit with a sum of two stretched exponential function with β equal to 0.78.

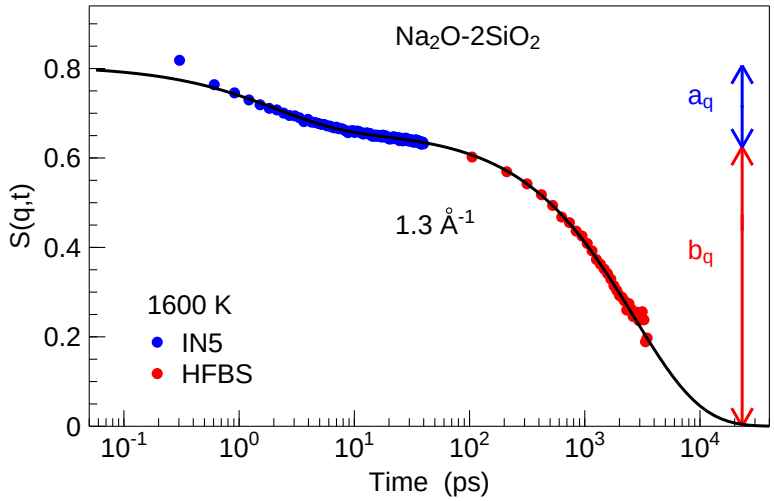

Figure 6.2: Schematic representation of the intermediate scattering function $S(q,t)$ based on experiments of NS2. The data of a neutron backscattering experiment (red) and a neutron time of flight experiment (blue) were matched together. Two distinct relaxation processes are observed. The solid line represents a fit with two stretched exponential functions. The fast relaxation process on a 10 ps timescale reflects the decay of the Na-Na self correlator, whereas the slower process on a 10 ns timescale comprises the decay of the remaining coherent correlation functions (Na-Na, Si-O, O-O and Si-Si).

In the following the discussion is restricted to time of flight data. The error on the data on an absolute scale as already discussed earlier is of the order of 10 %. The lineshape in the range of 1 ps to 10 ps is not subject to this error. Equation (6.4) is used to fit the time of flight data. With increasing q the amplitudes of the fit are in addition to the statistical error imposed on the data affected by two further error sources. One is the vibrational contribution raising with increasing q that leads to additional intensity roughly below 0.8 ps. At larger q the onset of the network relaxation approaching now a 100 ps timescale shifts in the time window accessed by time of flight spectroscopy. Both processes are overlapping with the Na relaxation process and consequently lead to an overestimation of the amplitude of relaxation of up to 20 %.

MD simulations also revealed a decoupling of the decay of the coherent correlators from the decay of the incoherent Na correlator [HoKB02] (see figure 1.3 presented in the introduction chapter) and the incoherent O and Si correlator from the sodium correlator [HoKo02]. Typical relaxation times for the self motion of Na are over the entire q range at least two orders of magnitude smaller. Such a behaviour shall also become visible in our experiments. We note that the absolute scale of the relaxation times presented in the simulation does not correspond to relaxation times observed by our experiments. The latter are smaller by approximately one order of magnitude. It results from the fact that $\langle\tau\rangle$ was taken for a fixed value $S(q,t) = 0.1$. Depending on β the latter overestimates relaxation times by up to a factor of 5. Evidenced by the simulation coherent Na-Na correlators decouple of the coherent network correlators close below the first sharp diffraction

peak. However, this behaviour can be probed neither by neutron backscattering nor by time of flight spectroscopy.

The density correlation functions at $q = 0.35\,\text{Å}^{-1}$ and $q = 1.3\,\text{Å}^{-1}$ for sodium disilicate are shown in figure 6.3. The solid lines represent fits with a stretched exponential function and a constant parameter b_q

$$S(q,t) = b_q + a_q \cdot \exp\{-(t/\langle\tau_q\rangle)^{\beta}\}\,. \tag{6.4}$$

In the accessible temperature range the data are described with a within error bars

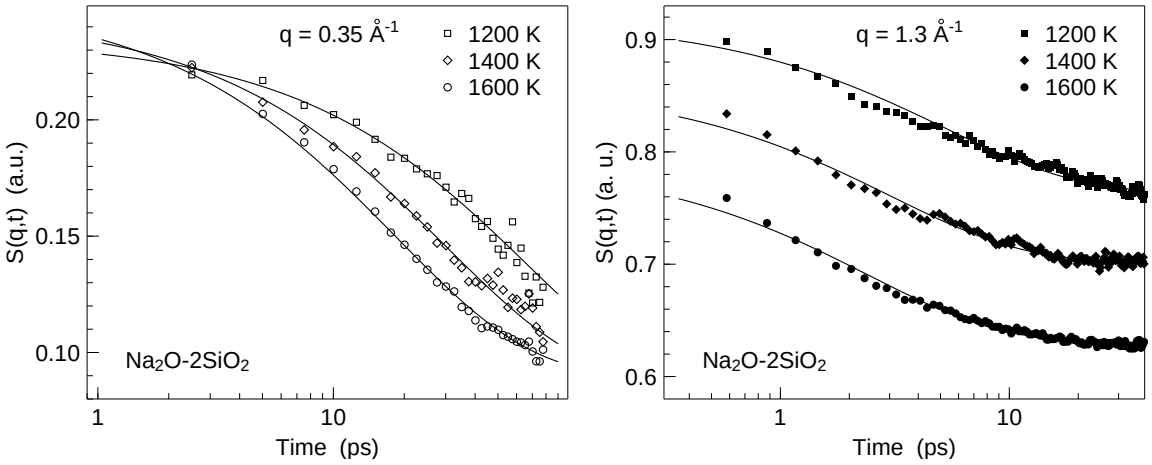

Figure 6.3: Density correlation function measured on IN5. Data are shown for three different temperatures and two different momentum transfer values. The solid line represent fits with a stretched exponential function using a stretching exponent β of 0.75. The deviations for $q = 1.3\,\text{Å}^{-1}$ in the range of 1 to 10 picosecond are more pronounced with decreasing temperature. We attribute this effect to the missing radial collimator that imposes characteristic oscillations on the Fourier transformed data (mostly at large q and low T).

q independent stretching exponent of $\beta = 0.75 \pm 0.04$. Therefore β was kept constant during the fitting procedure. The constant b_q reflects elastic contributions to the density correlation function[2]. They partly result from scattering on the Si-O network, that leads to a decay of the density correlation function on a nanosecond timescale. The decay in the density correlation function described by the stretched exponential function reflects the relaxation of Na. The contribution of the self correlation of Na is given by the relaxation amplitude a_q. Experimental proof for the latter finding will be provided by the discussion of the q dependence of this amplitude. For a better comparison of the relaxation timescales and the dependence of the relaxation amplitude a_q on q, the elastic contribution b_q as obtained of the fit was subtracted from $S(q,t)$ (see figure 6.4). The data is only shown for a single temperature and three different momentum transfer values for comparison. The relaxation amplitude a_q is almost q independent (see figure 6.5). This indicates

[2]Scattering processes which involve a decay of the density correlation function that is not observable owing to the instrumental energy resolution function contribute to elastic scattering.

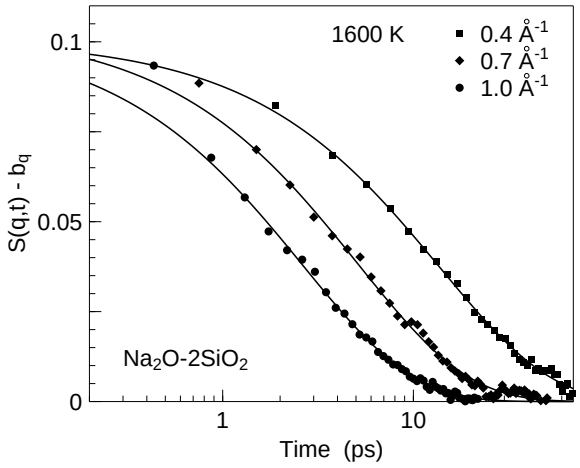

Figure 6.4: $S(q,t)$ of NS2 at 1600 K in the melt. The elastic amplitude b_q obtained by a fit with equation 6.4 to the measured data was subtracted. Hence, the relaxation amplitudes a_q can be directly compared. The density correlation functions exhibit relaxation times $\langle\tau_q\rangle$ decreasing with increasing q.

that only incoherent scattering contributes to the relaxation. A significant change in the relaxation amplitude with q is expected if the coherent Na-Na correlator decays on similar timescales. For Na the coherent cross section almost equals the incoherent cross section. Around a maximum of the coherent correlator that corresponds to 0.9 Å^{-1} and 1.7 Å^{-1} one thus expects an increase in the relaxation amplitude by up to a factor of two if coherent processes were contributing.

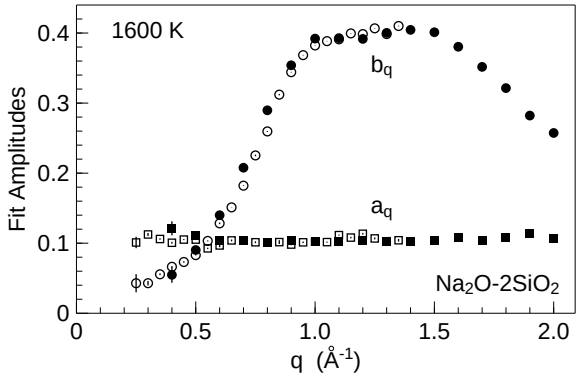

Figure 6.5: Elastic amplitude b_q and quasielastic amplitude a_q obtained by means of fitting the measured density correlation function of NS2. The open symbols represent IN5 and the closed symbols IN6 data, respectively. The elastic amplitude is proportional to the elastic structure factor. The quasielastic amplitude is almost q independent.

For purely incoherent scattering the relaxation amplitude shall feature a decrease with increasing wavevector, what is at odds with the data. We already discussed that the amplitude at large wavenumbers is subject to an overestimation of up to 20%. The approximation of relaxation processes on longer timescales by a constant b_q is no longer strictly valid for larger wavenumbers. The overestimation of the amplitude a_q effectively leads to an overestimation of the relaxation times at large q.

The q dependence of the relaxation times derived from the fit of NS2 data and data from an earlier measurement [MeDS02] are shown in figure 6.6. The relaxation times decrease with increasing wavenumber towards a plateau around 1 ps. Assuming that coherent correlators also contribute to $S(q,t)$ on the 1 ps to 100 ps range, we will expect pronounced oscillations in phase with the structure factor[3]. We thus conclude that only incoherent scattering contributes to the signal in the 1 ps to 100 ps range. Comparing the relaxation times to MD simulation data for NS2 at 2100 K in the melt (see figure 1.3),

[3]The effect of coherent scattering on the relaxation time was observed for liquid Ar [SkRO72].

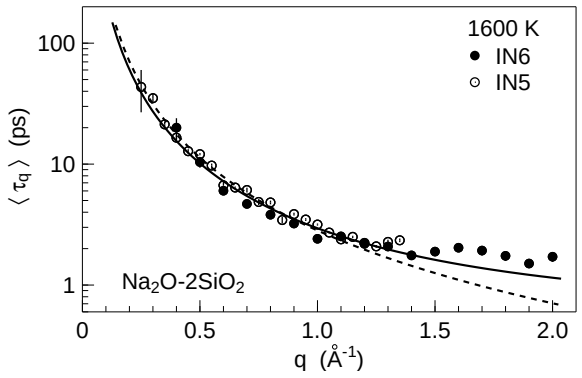

Figure 6.6: Mean relaxation time derived from the fit to the density correlation function measured for sodium disilicate at 1600 K. The IN5 data was measured for this thesis work. The IN6 data already measured in an earlier study [MeDS02] was reanalyzed in terms of Fourier deconvoluting the data to $S(q,t)$. Fit to Dq^2 law (dashed line) and jump diffusion model (solid line).

our data qualitatively agree. The experimentally observed timescale is about one order of magnitude lower. Investigating the decrease of the relaxation time for $q > 2$ Å^{-1} was not possible due to instrumental constraints.

A slight increase in the relaxation time around 1.7 Å^{-1} is explained by the result of the MD simulation. Close below the first sharp diffraction peak a decrease of the relaxation time of the coherent Na-Na correlator is observed approaching the relaxation time of the incoherent correlator. In our experiment we are not able, as already discussed for the borates, to separate with high accuracy two processes that are within only one order of magnitude. Our fitting procedure reflects this partial overlapping with a slightly increased timescale of relaxation.

We performed also an analysis of the data in the framework of the simplest form of the hopping model discussed in the chapter 3.3. A fit to the relaxation rate represented by the solid line in figure 6.6 results in a hopping length l of 0.5 ± 0.2 Å and a hopping time τ_0 of 0.6 ± 0.2 ps. These values yield a diffusion constant D for hopping transport of $4.1 \pm 0.5 \cdot 10^{-9}$ m^2 s^{-1} that compares well to tracer diffusion data discussed earlier in this section. In a complex structure like for the sodium silicates with a random network of diffusion pathways the simplest form of the hopping model is not expected to give an accurate description. In particular it can not explain the further decrease of the relaxation times on increasing q observed in the simulations. However, assuming that at least the basic concept of motion in restricted space is reflected one can discuss the fit values. The hopping length is slightly larger than half a sodium ionic radius. The characteristic hopping time is rather short and close to the regime of vibrational motions. One can thus speculate, whether the motion on interatomic lengthscales which is the limit of the hopping model fit at large q values reflects the restriction of motion to one dimension via this lengthscale l which roughly corresponds to the channel radius. Finally, we note that for $q \lesssim 0.7$ Å^{-1} the hopping model fit reflects not the dependence of the relaxation rate on q with high accuracy. A fit assuming a q^2 dependence performs better (see dashed line in figure 6.6). Results obtained on fitting a q^2 law are discussed below.

Replacing the alkali modifier ion Na by Li results in density correlation functions shown in Figure 6.7. The elastic contribution obtained from the fit is already subtracted. The density correlator of LS2 is shown for two different wavenumbers in comparison with the density correlator of NS2. We observe a smaller relaxation time for LS2. A reduced relaxation time is also suggested by conductivity measurements featuring a slightly increased

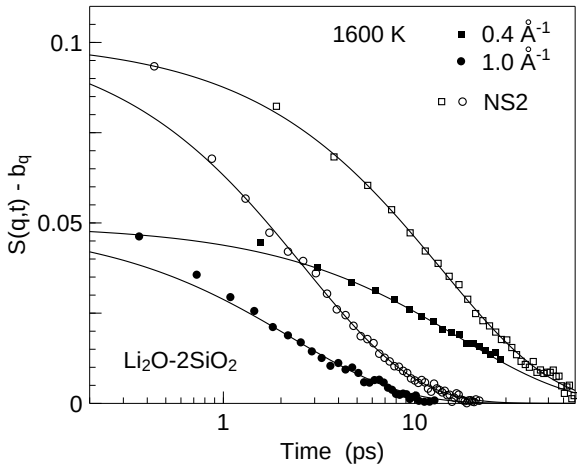

Figure 6.7: $S(q,t)$ of LS2 (closed symbols) measured on IN6 with an incoming wavelength of 5.9 Å. Open symbols represent the NS2 data already shown in figure 6.4 measured on IN5 ($\lambda = 8$ Å). The elastic amplitude b_q obtained by a fit with equation (6.4) to the measured data was subtracted. Hence, the relaxation amplitude can be compared on an absolute scale. For LS2 the amplitude a_q is half the value of that for NS2.

conductivity for lithium silicates compared to sodium silicates.

The relaxation amplitude a_q is reduced by a factor of two. We note that the incoherent cross sections of ^{7}Li is reduced by a factor of two compared to Na. The coherent cross sections for ^{7}Li and Na differ by almost a factor of three. The data are shown at $0.4\,\text{Å}^{-1}$ with only incoherent scattering on the alkali atoms contributing to $S(q,t)$. The second q value 1 Å^{-1} corresponds to the prepeak position. At this position the partial alkali-alkali structure factor was shown in the MD simulations to contribute equally as incoherent scattering to $S(q,t)$. If coherent alkali-alkali correlators relax on the same timescale as the incoherent alkali correlators the ratio of the relaxation amplitudes of LS2 and NS2 shall be different for the two q values shown, which is at odds to our data. This finding corroborates the conclusion that only incoherent scattering contributes to the relaxation on a 10 picosecond timescale.

The relaxation rates obtained from the fits on the sodium silicate samples feature a q^2 dependence for wavenumbers below 0.7 Å^{-1}. From the q^2 dependence we derived self diffusion coefficients for Na. For NS2 a comparison with data taken from literature is shown in figure 6.8. Self diffusion coefficients obtained in our measurements and tracer diffusivities from literature [GuKi67] compare well. If substantial amounts of Na relax on the longer timescales of the network relaxation, we may clearly expect a difference with lower diffusivities measured by means of tracer diffusion experiments. We note that tracer diffusion macroscopically measures the self diffusivity of Na averaged over all Na atoms. By means of neutron time of flight spectroscopy we observe only the fast Na α relaxation.

Electrical conductivity data [Tic67] shown in table 6.1 exhibit similar diffusivities for K in potassium silicates at 1600 K compared to sodium or lithium silicates. No substantial slowing down of the relaxation time is expected for the modifier ion K yielding still a relaxation on a 10 picosecond timescale in the melt. We note that for K the incoherent cross section is reduced by a factor of six compared to Na. This is clearly below the resolution of present day spectrometers. Obviously we shall not observe any clear indication for a relaxation process in potassium disilicate over the entire q range.

The density correlation of potassium disilicate for five different wavenumbers is shown in Figure 6.9. The data are normalized by $S(q, t = 0)$ taken from the Fourier deconvoluted

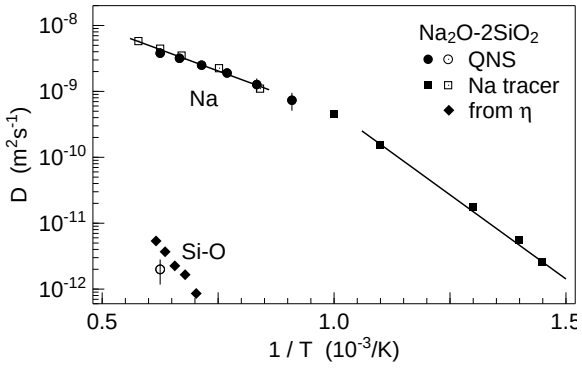

Figure 6.8: Comparison of Na self diffusivities and network diffusivities. Na tracer diffusivities were taken from [GuKi67] for the melt and [JoBB51] for the glass. Network diffusivities were calculated from viscosity data [KnDS94] using the Stokes Einstein relation. Network diffusivities are compared to neutron backscattering data. Na self diffusion constants obtained by means of time of flight spectroscopy are compared to data of [GuKi67].

spectra. The error imposed on the absolute scale is larger for smaller wavenumbers due to the finite energy range of the Fourier transformation. However, this has no impact on the result.

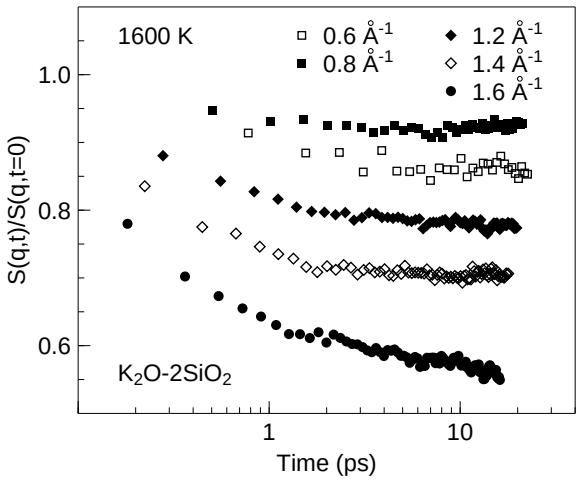

Figure 6.9: $S(q,t)$ normalized to unity in the limit $t \to 0$. The data are measured at 1600 K in the melt. Over the entire q range no α relaxation process is observed. At the largest wavenumber (1.6 Å^{-1}) the onset of a structural relaxation is observed. At large wavenumbers a decay at short timescales might partially reflect a secondary relaxation process.

At momentum transfers of $q = 0.6\,\text{Å}^{-1}$ and $0.8\,\text{Å}^{-1}$ in sodium and lithium silicates a relaxation process reflecting incoherent scattering on the alkali is clearly visible. Such a α relaxation process of K in KS2 is not resolved by the experiment. Only for the largest wavenumber $q = 1.6\,\text{Å}^{-1}$ the onset of a structural relaxation process becomes visible in the accessible time window. This is evidenced by deviations from the plateau at larger times. This process can be attributed to the relaxation of the network and coherent K-K correlators.

The difference between the plateau value and unity can be ascribed to the Debye-Waller factor. However, this behaviour can not be distinguished from an underlying secondary relaxation process as it is a fast β relaxation process of the MCT. In KS3 the overall behaviour of the density correlation function is similar (see figure 6.10). The decay of unity at short times is slightly less pronounced. This reflects the fact that KS3 has a higher viscosity at 1600 K compared to KS2 and thus at the same temperature the overall mobility in KS3 is smaller.

If present, the secondary relaxation process contributes only a minor amplitude to the density correlation in potassium silicates. With respect to a mode coupling scenario in binary alkali silicate melts we note the following: An ergodic to non ergodic transition

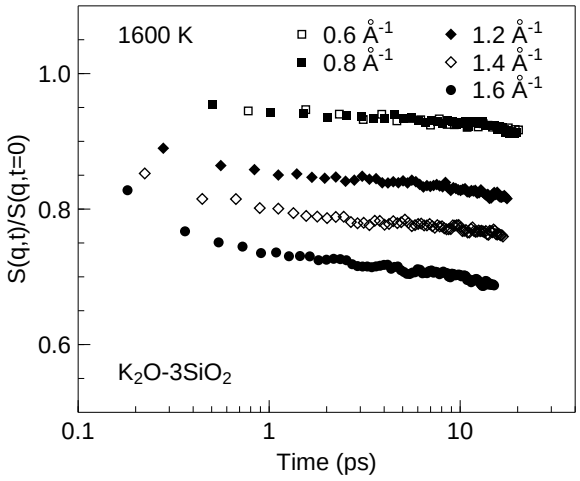

Figure 6.10: $S(q,t)$ normalized to unity in the limit $t \to 0$. The data are measured at 1600 K in the melt. No decay is observed that can be attributed to the relaxation of the incoherent K correlator. At 1.6 Å^{-1}) the onset of a structural relaxation is observed at large timescales. The short time decay of the density correlation function is less pronounced in KS3 compared to KS2.

temperature T_c was proposed by MD simulations on sodium silicates to be in the range of 2000 K [HoKB02] comparing to an experimental temperature of $T_{exp} \approx 1700\,\text{K}$, what is still above any experimentally accessed temperature. An unambiguous explanation of the decay in the density correlation function at short timescales in potassium silicate melts was not obtained during the thesis work.

However, the investigations on sodium, lithium and potassium silicate melts consistently provide evidence that only the incoherent correlations decay on a 10 ps timescale in the melt. This experimental result shows that the alkali ions are not homogeneously distributed in the structure. Moreover, the results also exclude that the ions are distributed among inhomogeneously arranged alkali rich clusters in the SiO_4 matrix. Otherwise the coherent alkali alkali correlators shall decay on a similar timescale compared the self correlator which is then observed by time of flight spectroscopy.

6.1.3 Structure on intermediate range scale

In the following paragraph we focus on the discussion of the elastic structure factors. Intermediate range scale denotes momentum transfers characterised by real space lengthscales beyond the nearest neighbour distance. Our discussion is restricted by the experiment to $0.2\,\text{Å}^{-1} < q < 2.2\,\text{Å}^{-1}$.

The first sharp diffraction peak (FSDP) around 1.7 Å^{-1} in the structure factor of silica based glasses represents typical SiO_4 tetrahedra distances. This has been experimentally evidenced for pure SiO_2 [Ell91]. When adding alkali modifier ions, the FSDP shifts to larger q values, decreases in height and broadens (see figure 6.11). It reflects the disruption of the rather ordered SiO_2 network leading to an increase in binding angles and a more pronounced distribution of nearest SiO_4 tetrahedra distances. This effect has already been shown about thirty years ago on sodium, potassium and lithium silicate glasses and melts by neutron and X-ray diffraction [WaSu77]. However, the instrumental constraints did not allow for measurements of high enough accuracy at small momentum transfer values below 1 Å^{-1}.

A motion of the sodium atoms in channels shall clearly impose additional correlations on the intermediate range scale. Typical interchannel distances which may in the investigated concentration range be rather regularly distributed shall lead to distinct features

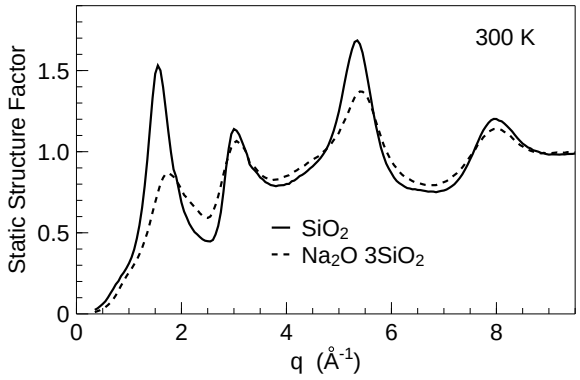

Figure 6.11: Static structure factor for pure SiO_2 and NS3 taken from [Poh05]. The data was measured at ambient temperatures by means of neutron diffraction on D20 ILL.

in the structure factor. MD simulations proposed such a correlation peak in the structure factor around 0.9 $Å^{-1}$, what was experimentally evidenced by a first neutron time of flight experiment on NS2 [MeDS02].

The elastic structure factor of the sodium silicates features a prepeak around 0.9 $Å^{-1}$. Recent molecular dynamics simulations [HoKB02, MeHK04] showed that the prepeak reflects typical distances of Na rich microchannels that are embedded in the static structure. The simulation also explains the absence of the prepeak in the glass in terms of a change in melt density leading to a shift in the partial structure factors (see figure 6.12). The total structure is based on the sum of six partial structure factors weighted with their neutron scattering length. The partial structure factors do no longer cancel each other at the position of the prepeak in the melt. Except the Si-Si partial structure factor a prepeak can be observed in all other partial structure factors.

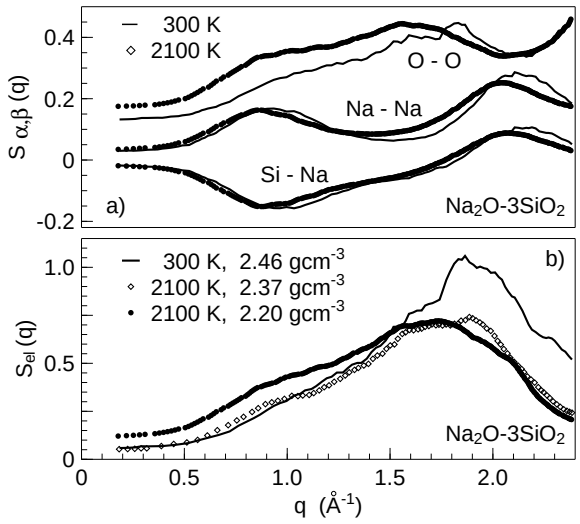

Figure 6.12: Figure a) exhibits three different partial structure factors of NS3 in the glass (solid line) and in the melt (circles). The O-O structure factor was shifted for clarity reasons. Figure b) shows the elastic structure factor calculated by summation of the partial structure factors weighted with the neutron scattering length. The circles represent data for different densities in the melt. Only at the experimental density a prepeak is observed. Note that all partial structure factors feature a prepeak. $S_{Si\,Na}(q)$ is negative indicating avoidance of this lengthscale.

During this thesis, we extended the compositional range to lithium and potassium silicate melts and investigated the elastic structure factor on intermediate range scale. We aimed to prove, whether this prepeak already reported for binary sodium silicates reflects typical interchannel distances for all binary alkali silicates within an alkali concentration range of 20 mol% to 33 mol%. Changing the size of the modifier ions shall lead to a shift in the position of the prepeak for smaller q values with increasing size of the

modifier ion. However, the change in alkali modifier content shall not significantly affect the prepeak position. The latter was already experimentally verified for sodium silicates [Kar02, MeHK04]. Data is shown in figure 6.13.

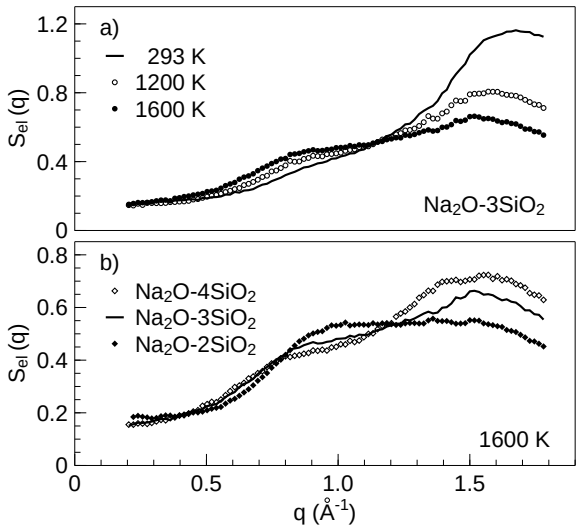

Figure 6.13: Elastic structure factors of NS3 in the glass and in the melt (see figure a)). A prepeak is emerging with increasing temperature in the melt. The lower graph (b)) features the elastic structure factor at 1600 K in the melt for NS2, NS3 and NS4. The prepeak is increasing with increasing Na content. The prepeak changes its position neither with temperature nor with composition.

In lithium disilicate we observe only a shoulder in the elastic structure factor. Assuming two Gaussian-like contributions for the first sharp diffraction peak around 1.6 Å^{-1} and for the prepeak, the prepeak position occurs around 1.0 Å^{-1}. The fit is represented by the solid line in figure 6.14. The two Gaussian lines represented by dashed lines are shifted on the y-axis for clarity reasons. Even with increasing temperature the height of this preshoulder remains almost constant. Effectively the latter corresponds to an increase with increasing temperature since increasing temperature usually will lead to a decrease owing to the Debye-Waller factor. Considering the Debye-Waller factor a 10% effect on the amplitude of the elastic structure factor at the prepeak position between 1300 K and 1600 K is expected. Within the error bar the prepeak position remains unchanged with increasing temperature. Thus the picture obtained of a network of alkali rich microchannels embedded in the static structure is further approved.

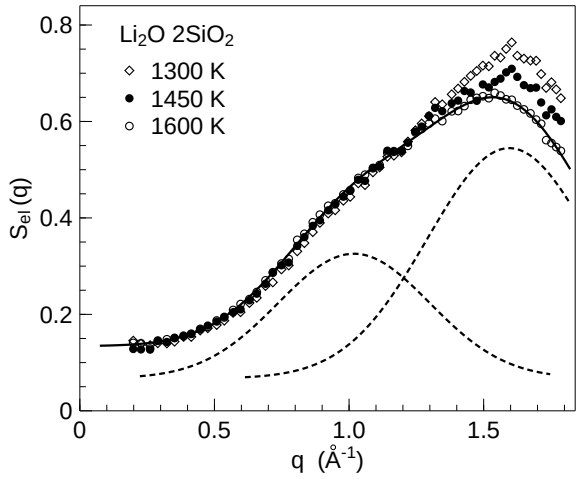

Figure 6.14: Elastic structure factor of lithium disilicate. Data are shown for three temperatures in the melt. No emerging prepeak is observed with increasing temperature. A preshoulder with a center location around 1.0 Å^{-1} is visible. The preshoulder position was determined by means of fitting two Gaussian lines on the data (dashed and solid lines). Due to partial crystallisation or phase separation on cooling the data are not compared to a room temperature structure factor.

For potassium disilicate a prepeak was reported by a recent neutron diffraction study [MaCC04] in the static structure factor. The position of the prepeak compared to sodium disilicate is at smaller wavenumbers. Its height is drastically increased exceeding already at room temperature the structure factor around 1.7 Å^{-1}. At the latter position no clearly pronounced peak is observed in KS2. The latter may be attributed to the fact that the larger modifier ion K rather strongly disrupts the SiO_2 network structure as speculated in [MaCC04]. However, on has to keep in mind that in potassium silicates the density is different. The MD simulations on sodium silicates show, that small changes in density severely affect the structure factor. Consequently, it cannot be ruled out that the density change in potassium silicates compared to sodium silicates dominates the change in peak intensities. Our investigations revealed similar behaviour for the elastic structure factor of KS2 shown in the left graph of figure 6.15.

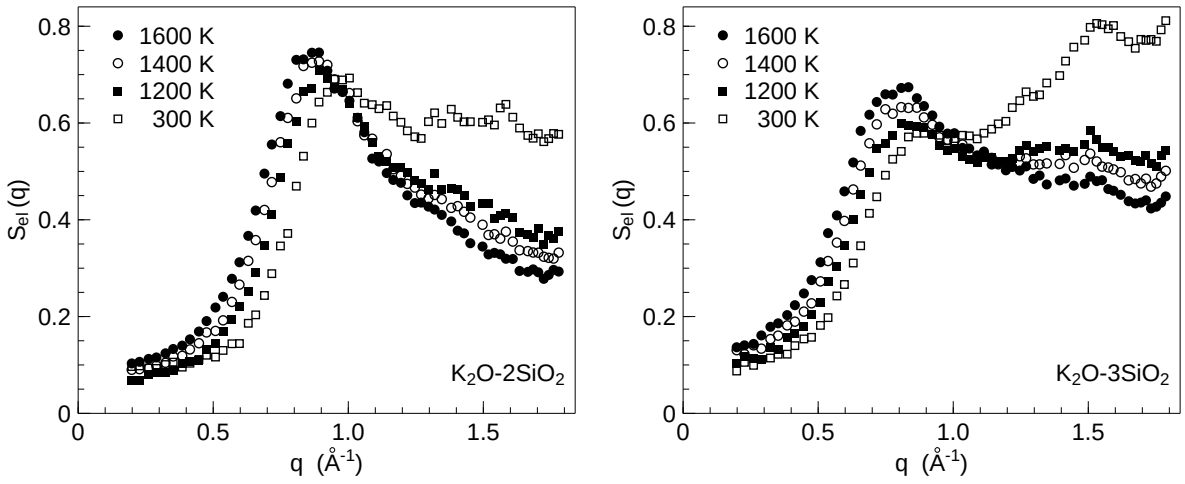

Figure 6.15: Elastic structure factor measured on IN6 for KS2 (left) and KS3 (right). Data are shown in the glass and at three different temperatures in the melt. A pronounced prepeak is revealed around 0.8 Å^{-1} independent of the composition. Its intensity increases similar to sodium silicates with increasing alkali content.

Moreover we investigated a potassium trisilicate melt (see right figure in 6.15). The prepeak position is unchanged upon a change in potassium concentration. The height of the prepeak is increasing similar to sodium silicates with increasing alkali content. The first sharp diffraction peak reflecting SiO_4 tetrahedra distances is still observable around 1.7 Å^{-1} in KS3 and almost vanishes in KS2.

Figure 6.16 features a comparison of the elastic structure factors of LS2, NS2 and KS2 at 1600 K. Data are presented on an absolute scale. We note that the LS2 data is due to the lack of a room temperature structure factor subject to an error of 20%. The comparison yields the results of a prepeak shift with increasing size of the modifier ion to smaller wavenumbers as expected for an increasing interchannel distance.

The observed behaviour of the elastic structure factors suggests that also K and Li ions diffuse along a network of channels embedded in the static structure. For Li silicates MD simulations also revealed the existence of preferential sites for ion diffusion [LaKH03].

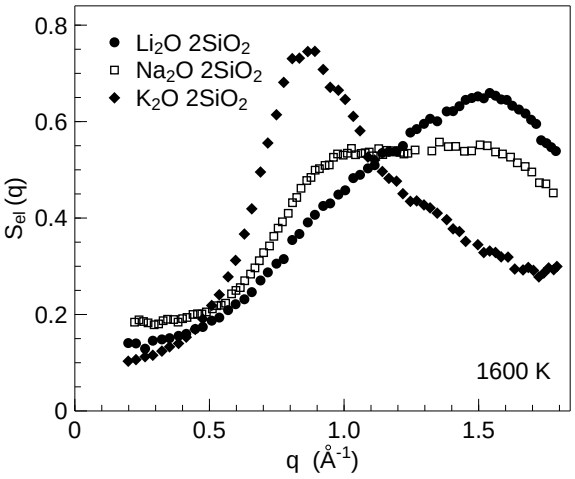

Figure 6.16: Elastic structure factor of LS2, NS2 and KS2 measured on IN6. The prepeak is most pronounced in KS2 and decreases with the size of the alkali atoms. The prepeak position shifts to smaller wavenumbers as LS2>NS2>KS2.

The preferential sites are named clusters in this study. However, the clusters are shown to comprise only one Na ion and are linked together in the sense that for a Na ion to move no Si-O bond has to be broken. Thus it is only the naming that is different and clusters in this study can also be recognized as diffusion channels. We conclude that all binary alkali silicates being subject to investigation feature the same underlying microscopic mechanism for fast alkali ion diffusion. The mechanism clearly differs from the results obtained for the sodium borates. Ion transport in the network of channels is rather free. The network of channels provides a structure of percolation pathways for fast ion diffusion. Breaking of covalent SiO bonds is not a necessary condition for the fast diffusion of the modifier ions.

6.2 Mixed alkali silicates

Further we investigated the influence of mixing different alkali modifiers on the network of channels and the microscopic dynamics. We investigated mixed alkali silicates that are ternary mixtures comprising SiO_2 and two different alkali modifier ions, e. g. Na and K. Na and K were chosen since we performed investigations on various binary endmembers NS2, NS3, KS2 and KS3 comprising only one modifier species.

Macroscopic measurements (e. g. ion conductivity [Tic67]) reveal a non linear behaviour of the self diffusivity on the alkali concentration ratio at fixed total alkali content. The dependence of the electrical conductivity scaled with temperature according to the Nernst-Einstein relation on K/(Na + K) concentration is shown in figure 6.17. The ion diffusivity is clearly reduced for K/(Na + K) = 0.5. This so called mixed alkali effect is less pronounced, the higher the temperature is. It depends also on the total alkali concentration in a non linear way [Kie99]. We note that in the mixed alkali systems the conductivity comprises contributions of both modifier ions.

Until now, the origin of this effect that is observed for numerous different ion conducting systems is still debated in literature [Hun99, Kie99, Maa99]. To explain the non linear dependence of conductivity or modifier ion diffusivity different scenarios have been discussed for the glassy state. Recent reverse Monte Carlo simulations on sodium phosphates postulate a random distribution of the alkali ions in percolation pathways

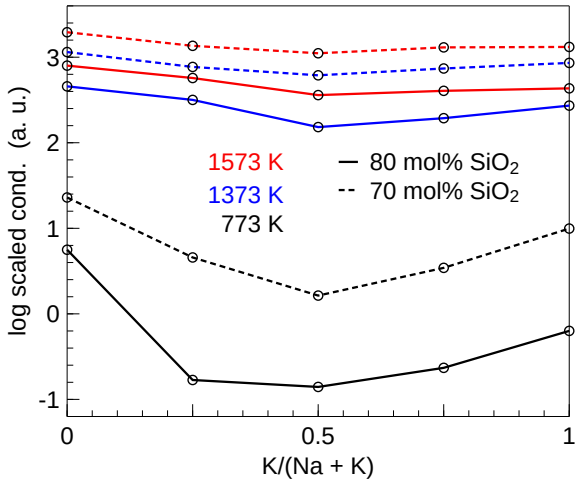

Figure 6.17: Logarithm of conductivity data scaled according to the Nernst-Einstein relation with temperature. Measured data ([Tic67]) are represented by open circles, the lines are guide to the eyes. The mixed alkali effect is more pronounced at lower temperatures and at higher SiO_2 concentration.

[SwAd03, SwMK01]. The ion transport is reduced in mixed-alkali glasses compared to the binary glasses due to blockage of the site incompatible alkalis.

In the binary alkali silicates we provided evidence for a network of alkali rich ion conduction channels in the static structure. One can now ask the question whether in the mixed Na-K silicates two independent but interpenetrating channel network structures for the different alkali ions exist or whether Na and K are simply statistically distributed within one common network as suggested for the mixed alkali phosphates.

Na_2O-K_2O-4SiO_2 (NKS4) and Na_2O-K_2O-6SiO_2 (NKS6) were investigated by means of time of flight spectroscopy. NKS4 is based on the sodium and potassium disilicate endmembers respectively. NKS6 is based on the trisilicate counterparts. The evolution of the elastic structure factor from the glass to the melt and the alkali relaxation on a picosecond timescale in the melt is discussed.

6.2.1 Structure in sodium potassium silicates

The elastic structure factor for the trisilicate and for the disilicate composition exhibit a prepeak. The prepeak gradually changes its intensity and position with increasing temperature as shown in 6.18. In NKS4 (left graph) a clearly pronounced prepeak at q values larger than $1\,\text{Å}^{-1}$ is observed in the glass. In the melt at 1600 K the position of the prepeak is between the value for pure KS2 and pure NS2. On increasing temperature the prepeak position shifts to smaller wavenumbers ($\approx 0.9\,\text{Å}^{-1}$ at 1600 K). It broadens with increasing temperature. The height of the prepeak first slightly decrease with the Debye-Waller factor. Similar to the sodium silicates the increase of the peak between 1200 K and 1600 K might be explained by a shift in the partial structure factors. We note that we can not determine the partial structure factors. Further $S_{el}(q)$ of NKS4 yields a small peak at the position of the first sharp diffraction peak in NS2. In contrast to NS2 the structure factor further increases beyond $q = 1.6\,\text{Å}^{-1}$. We note that NKS4 compared to NS2 and KS2 comprises additional contributions to the scattering law e. g. the coherent Na-K scattering contributions. At larger q values in the elastic structure factor the Debye-Waller factor dominates the decrease of the signal.

In contrast to NKS4 in NKS6 only a preshoulder on top of a broad intensity distri-

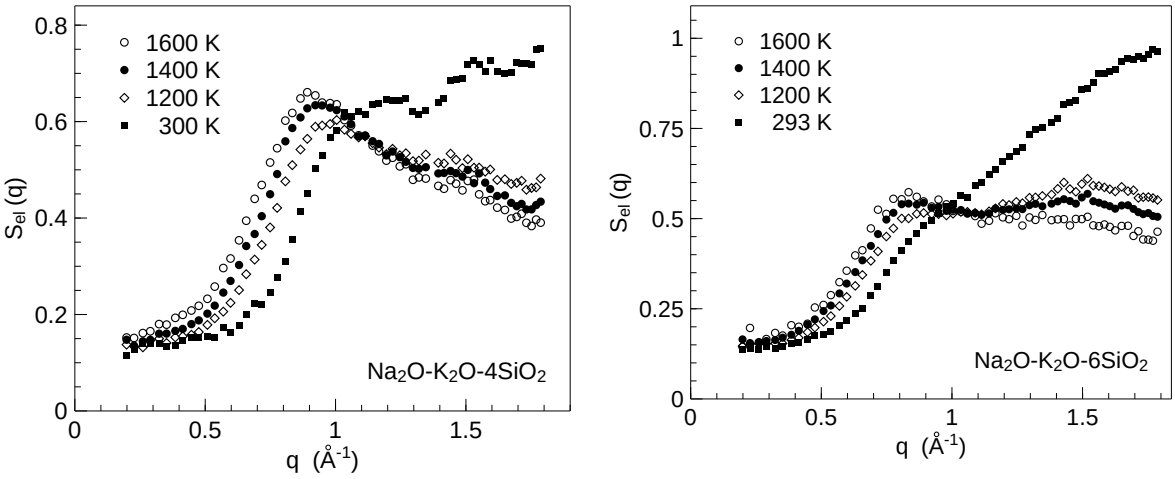

Figure 6.18: Elastic structure factor of NKS4 and NKS6 measured at IN6 in the glass (300 K) and in the melt. In NKS4 a prepeak is present already in the glass around. The prepeak emerges with increasing temperature. In NKS6 only a preshoulder is visible that becomes more pronounced with increasing temperature. A comparable behaviour is found in NS3 (see figure 6.13 a)).

bution is observed in the glass. The rather broad peak almost extends over the whole measured momentum transfer range. The intensity of the broad peak decreases with increasing temperature with the Debye-Waller factor with a maximum around 1.5 $Å^{-1}$ in the melt. A prepeak clearly emerges of the shoulder. The center of the peak shifts to smaller wavenumbers with increasing temperature and increases in height. A rather broad FSDP around 1.5 $Å^{-1}$ becomes visible in the melt.

Also in the mixed alkali silicates the prepeak and its dependence on composition and temperature reflects the non homogeneous distribution of the alkali ion in the SiO_2 matrix. The measured temperature and composition dependencies of the elastic structure factors allow for a comparison of MD simulations. However, at present no suitable potential and consequently no simulation reflecting the exact behaviour on a mixed alkali system can be found in literature.

We compare the elastic structure factors of NS2, NKS4 and KS2, and the elastic structure factors of NS3, NKS6 and KS3 at room temperature and at 1600 K (see figures 6.19 and 6.20).

Solid lines presented in the figures were obtained by means of a calculation based on $S_{el}(q)$ of the binary silicates at the same temperature. For that purpose we assumed a linear superposition of the two binary structure factors based on the assumption that the additional partial structure factor that reflects Na-K correlations gives only a minor contribution. We further assumed that the molar volume of Na and K silicates is not strongly different and is also a linear superposition of the molar volume of the binary silicates. The calculated structure factor is then obtained by

$$S_{el}^{calc}(q) = 0.5 \left(S_{el}^{NSx}(q) + S_{el}^{KSx}(q) \right) . \tag{6.5}$$

NSx and KSx denote the composition of the binary melts with x equal to two or three.

The measured elastic structure factor for NKS4 at room temperature and a structure factor represented by the solid line that was calculated from NS2 and KS2 data agree qualitatively. The first sharp diffraction peak and the plateau at small q dominated by incoherent scattering on Na are reproduced. Only the prepeak intensity of the measured curve exceeds the calculated curve. We note that the mixed alkali system comprises also coherent Na-K correlations which are not reflected in the calculation. At 1600 K the calculated and the measured curve agree qualitatively with the measured intensity that exceeds the calculated intensity around the prepeak position.

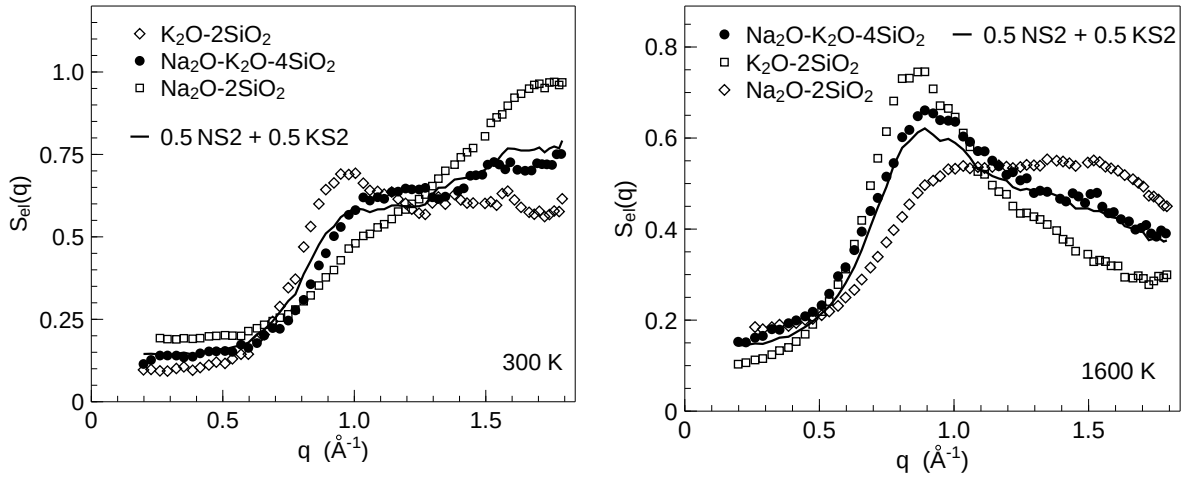

Figure 6.19: Elastic structure factor of NS2, NKS4 and KS2: (left) elastic structure factor at room temperature. (right) elastic structure factor at 1600 K in the melt. The prepeak in the structure factor is continuously emerging and shifts to smaller q values with replacing Na for K. The first sharp diffraction peak around 1.6 Å^{-1} is continuously decreasing.

For NKS6 in the glass the calculated curve that features distinct oscillations and the measured curve that shows only a broad intensity distribution over the entire wavenumber range do not coincide. Neither the intensity nor the q dependence of the measured curve are reflected by the calculated curve. In the melt the prepeak intensity and shape is reproduced by the calculated curve. A peak around 1.5 Å^{-1} in the calculated curve is not shown by the measured curve. The latter essentially reflects the differences in intensity around this position present already at room temperature and can not be attributed to the Debye-Waller factor. The measured data suggests that KS3 and NKS6 at 1600 K are not distinguished in intensity at this peak position. Two possibilities, a larger impact of the Debye-Waller factor or substantial shifts of the partial structure factors between the glass and the melt, can be the origin of this effect.

In the following we propose one possible explanation for the differences between the calculated and the measured curve. We note that the assumption for using the calculation of a combined structure factor was that two different percolation pathways and no random distribution of the alkali ions in a common network of channels exists. Consequently the different partial structure factors of the binary systems shall respect with only minor changes their positions and intensities of the binary silicate counterparts. In both mixed

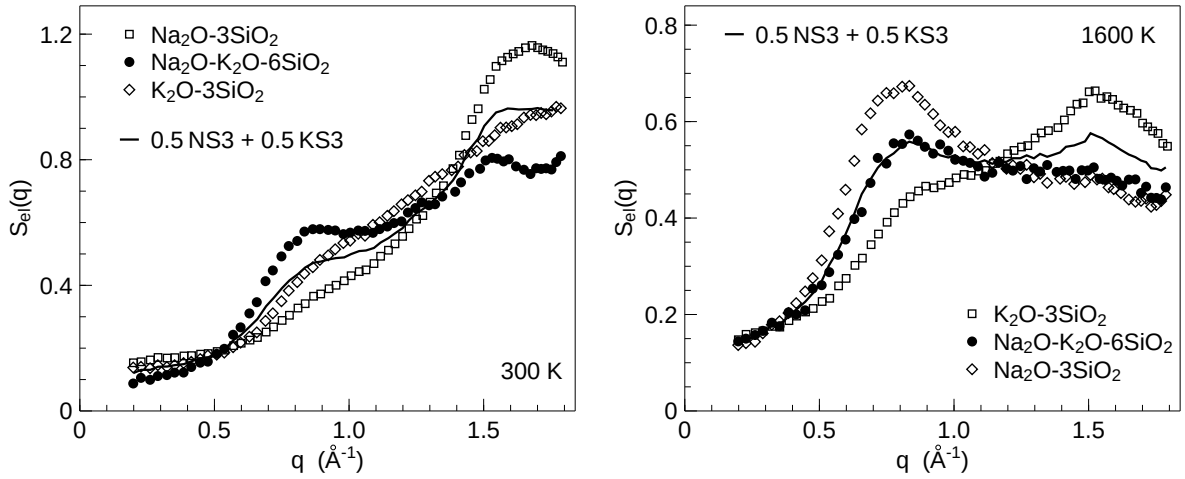

Figure 6.20: Elastic structure factor of NS3, NKS6 and KS3: (left) elastic structure factor at room temperature. (right) elastic structure factor at 1600 K in the melt. The prepeak in the structure factor emerges and shifts to smaller q values with replacing Na for K. The first sharp diffraction peak around 1.6 Å^{-1} continuously decreases with increasing K content. The solid line represents the sum of the elastic structure factors of NS3 and KS3 divided by two.

system one additional correlation, Na-K, contributes to the signal compared to the sum of the binary systems. In NKS4 the total number of modifier ions matches the number of Si atoms, whereas in NKS6 the total number of alkali atoms is only two third the number of Si atoms. In the binary silicates it was observed that the intensity of the FSDP decreases with increasing alkali content, but that the positions of the prepeak and the FSDP are unchanged. Only replacing the modifier ion species leads to a pronounced change of the prepeak. In both samples we observe the intensity around 1.6 Å^{-1} overestimated in the calculation compared to the measured data. We also observe additional intensity roughly around 1.2 Å^{-1}. It is less in the system containing more alkali atoms. The findings are in agreement with our proposed explanation. That will enhance lengthscales reflecting inter alkali alkali channel distances.

6.2.2 Impact of alkali mixing on Na diffusion.

Further investigating the dynamics on a 10 picosecond scale one can probe whether over the entire q range only the incoherent Na-Na correlator decays on this timescale or whether also coherent Na-K correlations will contribute to the signal. We note that in the mixed-alkali silicate glasses at small wavenumbers incoherent scattering on Na mostly contributes to a decay in the density correlation function. The contributions of different processes to the total scattering at small wavenumbers was discussed in detail in section 3.1.3. With the number of Na ions in NKS4 reduced by a factor of two compared to NS2 and in NKS6 by almost a factor of three compared to NS2 and relaxation times expected to be up to a factor of two larger in the mixed system an analysis of the data with respect to relaxation processes becomes a difficult task. At larger wavenumbers additional intensity for the relaxation amplitude is expected if Na-K correlations decay on similar timescales

The relaxation amplitude and relaxation timescales of the measured $S(q,t)$ shall oscillate in phase with the structure factor. Figure 6.21 exhibits the density correlation function of NKS4 and NKS6 for different wavevectors at 1400 K in the melt. The data was normalised by $S(q,t=0)$ for a better comparability of data at different q. The measured data allows not for a conclusive interpretation concerning coherent contributions. However, data at 0.5 Å^{-1} at which only incoherent scattering on Na contributes to the decay in the density correlation function on this 10 ps timescale suggests a faster relaxation of Na in NKS4 compared to NKS6. Moreover, in both systems Na relaxation times are larger compared to the binary equivalents NS2 and NS3.

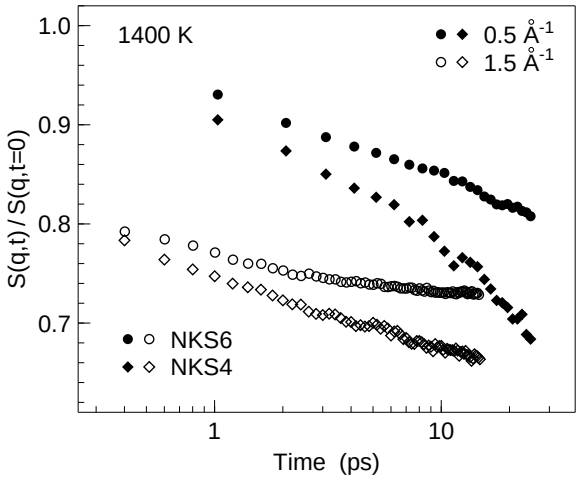

Figure 6.21: S(q,t) for NKS4 (circles) and NKS6 (diamonds). The data are shown normalised by $S(q,t=0)$ for two different wavenumbers with the two upper curves at $q = 0.5\,\text{Å}^{-1}$ and the lower curves at $q = 1.5\,\text{AA}^{-1}$. Below 0.8 ps vibrations contribute also to the signal. The decay at 0.5 Å^{-1} reflects the Na self correlator.

Assuming that a q^2 scaling holds to a first approximation in the mixed alkali silicates at 1.5 Å^{-1} we expect the sodium relaxation with a relaxation time $\langle\tau_q\rangle$ of approximately 2 ps. We note that at this wavenumber already coherent scattering dominates the total scattering signal. In NKS4 we observe the onset of a second structural relaxation process at times of 5 ps, whereas in NKS6 only a single decay is observed. The onset of this second relaxation process can be a signature for the decay of the coherent Na-K correlator, since the network relaxation according to viscosity data is on a nanosecond timescale. To analyse the data in terms of the determination of relaxation amplitudes and relaxation times over the entire wavenumber range demands for measurements that yield density correlation functions up to 60 ps in time.

The measurements on the mixed alkali silicates show that the elastic structure factors follow the overall expected behaviour. A prepeak was shown to emerge in the melt with increasing temperature. Owing to K which already has been shown to lead to a more pronounced prepeak at shorter wavenumbers compared to the binary silicates the prepeak in NKS4 is present already in the glass. In NKS6 it clearly emerges in the melt. In both samples the positions of the prepeak are between the positions of the prepeak of the corresponding binary alkali silicates. The Na self motion is still decoupled of the network in the mixed alkali systems by orders of magnitude. The measurements allow not for a determination of the relaxation amplitudes of the structural relaxation of the alkali ions. Consequently, the interpretation of the dependence of the prepeak on the alkali ratio as formation of two interpenetrating alkali networks is only one possibility to explain the

data. However, the results on the elastic structure factor and the relaxation dynamics in the mixed alkali silicates provide further evidence for an inhomogeneous distribution of the alkali ions in percolation pathways.

6.3 Sodium aluminosilicates

In the following we study the influence of a second network forming component on transport properties and structure of sodium silicate melts. Sodium aluminosilicates contain a number of geological important minerals like albite, jadeite and nepheline. These ternary compositions serve as simple model systems for lava. The outline of this section is as follows: First we describe the effect of adding alumina to binary sodium silicate mixtures that drastically changes the macroscopic properties. (see chapter 6.3.1). Afterwards a model trying to explain the viscosity–temperature and viscosity–composition relationship is briefly discussed. Chapter 6.3.2 is devoted to our neutron scattering investigations. Adding Al_2O_3 to a binary sodium silicate melt disrupts the channel structure. This is evidenced by a decreasing prepeak and increasing relaxation time for Na diffusion.

6.3.1 Macroscopic properties

The presentation of macroscopic properties is related to the Na_2O-Al_2O_3-SiO_2 concentration diagram (see figure 6.22).

Adding alumina to a binary sodium silicate melt leads at a given temperature to an increase in viscosity by several orders of magnitude depending on the total amount of Al_2O_3. In contrast, adding SiO_2 to the same binary melt has only minor consequences on the viscosity as it is shown in figure 6.1. In this case only an increase within about one order of magnitude over a large variation of SiO_2 content is observed.

Furthermore, a highly non linear dependence of the viscosity on composition at a given temperature in the melt is reported for sodium aluminosilicates [ToDH97, ToDL97, Rie66]. The viscosity of a sodium aluminosilicate melt for fixed SiO_2 concentration is first increasing with decreasing Na_2O content. It reaches a maximum beyond the tectosilicate isoconcentration line (Na_2O:Al_2O_3 = 1:1) on the Al_2O_3 rich side. Upon further adding Al_2O_3, the viscosity decreases slowly within the same order of magnitude. A model for the explanation of this behaviour was first proposed in [Lac63], that assumes a formation of triclusters. The idea was compatibly with the viscosity measurements. Tricluster formation describes the effect that Al in tetrahedral configuration shares one oxygen with two SiO_4 tetrahedra or one SiO_4 tetrahedra shares one oxygen with two Al tetrahedra. Tricluster formation is expected to be the principal mechanism to build in Al_2O_3 at larger Al_2O_3 concentrations close to the tectosilicate join.

Aluminum bound in tetrahedral configuration has an extra charge attached, which is balanced by a network modifier ion (e. g. Na). Adding further Al_2O_3 to a binary sodium silicate melt leads to a larger fraction of Na ions closely attached to alumina. Na attached to Al is more strongly bound to the network compared to Na ions attached to non bridging oxygens as in binary alkali silicates. Attaching Na to alumina decreases the number of Na ions participating in the fast diffusion process. Moreover, the relaxation time shall

increase. In the peralkaline region substantial amounts of Na are still attached to non bridging oxygens. Thus only a moderate increase in relaxation time is expected. If the idea of tricluster formation is valid, Na motion in systems close around the tectosilicate join will require breaking of oxygen bonds. Consequently, the Na ion diffusion will significantly slow down.

Independently of any model, we expect that the addition of Al_2O_3 has an impact on the Na channel structure. Moreover, the Na ion diffusion will be affected. An influence on the channel structure shall experimentally be observed by a change in the elastic structure factor.

Neutron scattering offers the possibility of probing a decrease in the number of Na ions contributing to the fast ion diffusion. However, we will show that the decreasing signal strength owing to the decreasing total amount of Na in the melt is a limiting factor for any experiment that aims to provide relaxation amplitudes on an absolute scale. In contrast, it is easily possible to reveal the influence of Al_2O_3 on the relaxation rate.

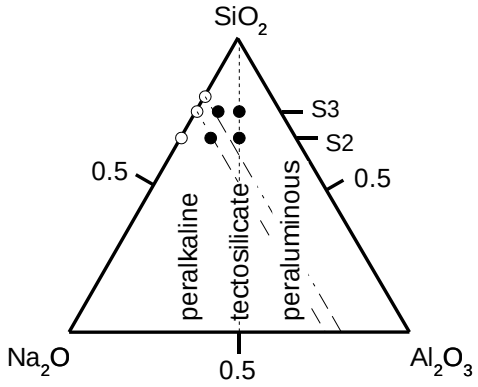

Figure 6.22: Na_2O–Al_2O_3–SiO_2 concentration diagram taken from [KaMe04]: sodium aluminosilicates (•) and sodium silicates (○). Investigations were restricted to the Na rich region (peralkaline) and the tectosilicate join. The double dashed lines indicate Na_2O isoconcentration lines.

6.3.2 Impact of Al_2O_3 on the interplay of microscopic dynamics and structure

We investigated samples on two isosilica joins. Besides melts that are based on NS2 (33 mol% SiO_2 content) we also probed melts that are based on NS3 (25 mol% SiO_2 content). The investigated aluminosilicates are represented by the filled circles in the already shown concentration diagram (see figure 6.22).

The elastic structure factors of the NS2 and the NS3 based melts are shown in Figure 6.23. For the tectosilicate compositions ($Na_2O/Al_2O_3 = 1$) the elastic structure factor at room temperature is shown as a solid line for comparison. The FSDP around 1.6 $Å^{-1}$ is increasing with increasing Al_2O_3 content, whereas the prepeak at 0.9 $Å^{-1}$ is decreasing on raising the Al_2O_3 content. No prepeak is observed in the tectosilicate compositions comprising equal amounts of Na_2O and Al_2O_3. For the Na_2O/Al_2O_3 ratio equal to three the increase of the prepeak with raising temperature is less pronounced compared to the binary sodium silicates.

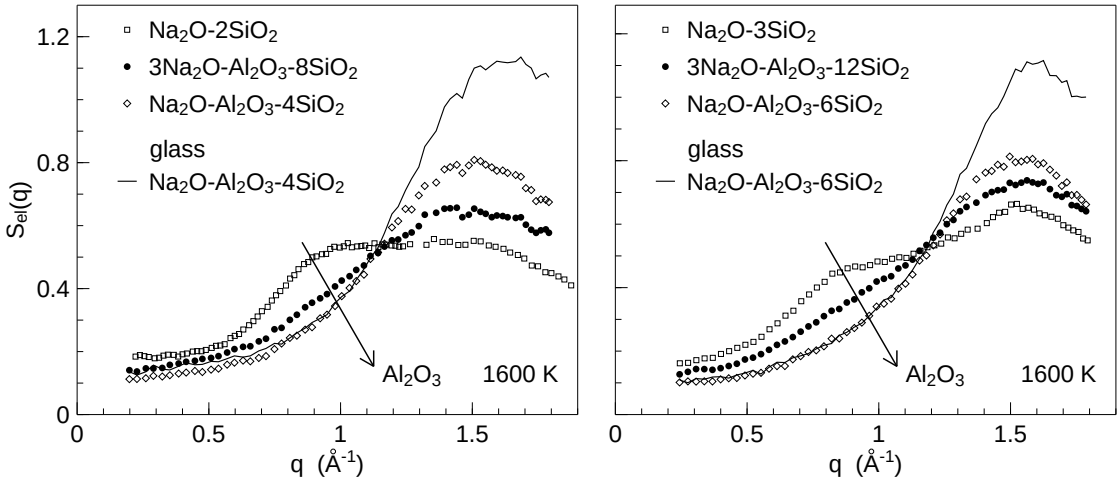

Figure 6.23: Elastic structure factors of samples containing 66 mol% (left) and 75 mol% SiO_2 (right). The data were obtained on IN6. The solid lines represent the elastic structure factors of the samples NAS4 and NAS6 at room temperature. In these samples no emerging prepeak is observed.

We conclude that adding Al_2O_3 affects the Na channels. The network of channels could either be disrupted in the sense of closing the channels by bridging non bridging oxygens with alumina or in the sense as it was suggested for the incorporation of alumina in literature [Lac63, ToDL97]. The latter addicts the disruption of channels to the fact that Na has to charge balance the Al ions. In both cases the Na transport will decrease. It shall become visible in the density correlation function by a decreasing relaxation time of the decay reflecting the diffusion of Na.

We note that the viscosity is drastically increasing upon adding alumina that leads to an even more pronounced separation of fast Na ion diffusion and network transport. Time of flight data taken on sodium aluminosilicates will not observe any contribution of the network relaxation. The network only contributes a constant to the density correlation function at large times.

Figure 6.24 shows the density correlation function of NS2, NS3, N3AS8 and N3AS12 at $q = 0.5\,\text{Å}^{-1}$ and 1600 K. The data are rescaled by means of their relaxation amplitudes a_q obtained by a fit with (6.4). For that purpose we kept $\beta = 0.75$ was kept constant for the aluminosilicates as it was for the binary silicates. Rescaling was done as follws. We plot the data with the fit parameter b_q reflecting elastic scattering contributions as lower y-scale boundary. The upper y-scale boundary shown in the figure for any curve is $a_q + b_q$. The data were rescaled to clearly show the slowing down of Na ion dynamics on addition of Al_2O_3. We aimed to show the amplitude on an absolute scale. However, owing to the increasing relaxation time the density correlation function in sodium aluminosilicates is not fully covered by the accessible time range. Moreover, the decrease of the Na_2O content leads to a decrease in the signal strength. Thus, we note that due to this experimental constraints on the signal the error bars for the value of the amplitude a_q is of the order of 30% for comparison of N3AS12 to NS3 and of the order of 20% for comparison of N3AS8 to NS2. When trying to deduce the number of Na ions that participate in the

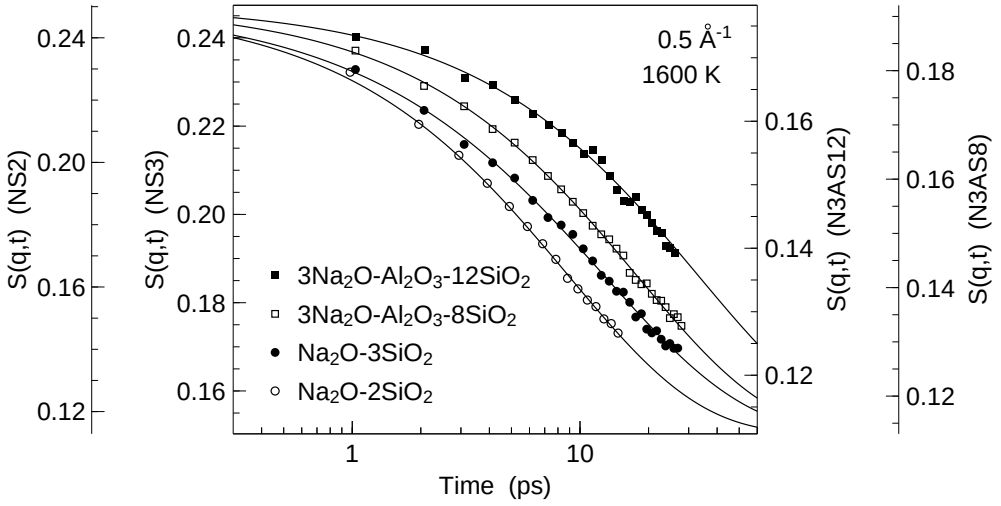

Figure 6.24: Intermediate scattering function measured on IN6 at 1600 K. The data is presented at 0.5 Å^{-1} with incoherent scattering on Na as the only contribution to the structural α relaxation observed in the experiments. The Na dynamics is slowing down upon adding Al_2O_3 to the binary melt. The data are presented as measured. The amplitudes of the aluminosilicates are subject to an error in the range of 20% - 30%.

fast diffusion process the accuracy of the desired quantity is highly affected with lower Na content.

Adding Al_2O_3 leads to an increase in relaxation time $\langle\tau_q\rangle$ for the Na ion motion. The relaxation times of the intermediate compositions N3AS8 and N3AS12 are thus reduced by a factor of two. Tectosilicate melts that contain equal amounts of Na_2O and Al_2O_3 show increasing relaxation times that exceed the experimentally accessible time window. Consequently, they are not shown in this figure. Data for NAS4 and NAS6 is separately shown in figure 6.25.

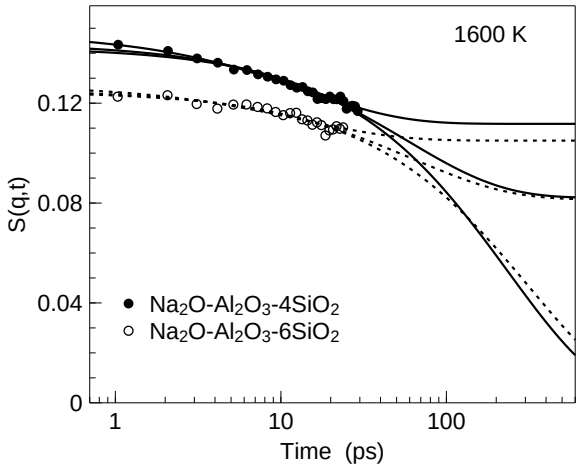

Figure 6.25: $S(q,t)$ for NAS4 and NAS6 shown at $q = 0.5\,\text{Å}^{-1}$. Different fits to the data are represented by solid lines (NAS4) and dashed lines (NAS6). The lower line was obtained with b_q fixed to zero, for the middle line a_q was estimated from NS2 and NS3 data taking the number of Na atoms into account. The upper line was obtained by a fit estimating an upper limit for b_q.

For the intermediate compostions N3AS8 and N3AS12 we derived Na diffusion coefficients assuming a q^2 dependence of the relaxation rate. This constitutes a good approximation for only incoherent scattering at small wavenumbers. Using the relaxation rate at 0.5

$Å^{-1}$ we estimate D. At this q value only incoherent scattering on Na contributes to the density correlation function. Coherent scattering on Na and scattering on the network components contributes only to the elastic amplitude b_q. We obtained as diffusion coefficients $D = 1.8 \pm 0.2 \times 10^{-9}\,m^2\,s^{-1}$ (N3AS8) and $D = 1.0 \pm 0.2 \times 10^{-9}\,m^2\,s^{-1}$ (N3AS12) at 1600 K in the melt. They compare with the diffusion coefficients obtained for the binary silicate melts $D = 3.8 \pm 0.3 \times 10^{-9}\,m^2\,s^{-1}$ (NS2) and $D = 2.1 \pm 0.3 \times 10^{-9}\,m^2\,s^{-1}$ (NS3) at 1600 K. For NAS4 and NAS6 we are only able to provide lower and upper limits for the diffusivities that are $2.5^{-9}\,m^2\,s^{-1} > D > 1 \times 10^{-10}\,m^2\,s^{-1}$ if we assume $\beta = 0.75$. An estimation based on a comparison of the amplitudes discussed at the end of this section results in $D = 6 \times 10^{-10}\,m^2\,s^{-1}$ (NAS4) and $D = 5 \times 10^{-10}\,m^2\,s^{-1}$ taking charge balancing of Al by Na not into account. Along the constant SiO_2 concentration joins the diffusivities decrease by a factor of two between the corresponding binary silicate melt and N3AS8 and N3AS12. Comparing data for constant Al_2O_3 content, the diffusivities increase with raising Na_2O content. Along the constant Na/(Na+Al) joins the diffusivities increase with decreasing Al_2O_3 content. Observing different iso-concentration lines for the different components we observe a non-linear behaviour of Na diffusivities with varying the total Al_2O_3 amount in sodium aluminosilicate melts.

A comparison of the fit amplitudes a_q yields the ratios R_a. We calculated these values for NS3/NS2, N3AS8/NS2 and N3AS12/NS3 and compare it with the ratio R_i of the pecentage of Na ions in the melt. For the sodium aluminosilicates R_i was calculated based on the assumption that all Na atoms contribute to the fast process. Moreover, we assumed that the number of the contributing Na ions is reduced by the number of ions bound to Al for charge balancing reasons R_{cb}.

	NS3/NS2	N3AS8/NS2	N3AS12/NS3
R_a	0.69 ± 0.09	0.57 ± 0.13	0.71 ± 0.23
R_i	0.75	0.71	0.72
R_{cb}	–	0.47	0.48

Table 6.2: Ratios R_a of the relaxation amplitudes a_q and ratios of the number of sodium ions R_i and R_{cb} , where R_{cb} takes complete charge balancing of Al by Na into account.

Sodium aluminosilicates show no clear distinction whether only the Na atoms attached to non bridging oxygens or also Na atoms attached to Al_2O_3 contribute to the fast Na ion diffusion. Only N3AS8 reveals a tendency that only part of the Na ions to contribute to the relaxation. Owing to the upper limit of 30 ps for the measured data in N3AS12 the amplitude a_q tends to be slightly overestimated, since only the upper half of the decay is covered by our experiment (see figure 6.24).

We deduce from the increase in viscosity, the decrease of the prepeak and the decreasing sodium mobility that the channel structure for fast ion diffusion is disrupted in binary silicate melts with adding Al_2O_3 to this melt. The structure is more disrupted in melts with constant SiO_2 content for a larger Al_2O_3 amount.

6.4 Iron bearing sodium silicates

Iron bearing silicates are important in geosciences, since most of the natural available magmas contain substantial amounts of Fe_2O_3. Fe features distinct differences compared to Al. Fe occurs in silica based melts in two different oxidation states, Fe^{2+} and Fe^{3+}. Fe^{3+} is believed to be in tetrahedral coordination similar to Al in the aluminosilicates [Bur00]. The ratio of the oxidation states depends on temperature, melt composition and synthesis atmosphere. For a chosen atmosphere and melt composition the variation with temperature in the typical range up to 1500 °C is only weakly pronounced. In contrast, a change of the oxygen content in the atmosphere has a rather huge impact on the oxidation state. A general rule is of thumb follows that the lower the oxygen content during high temperature annealing, the larger the Fe^{2+} to Fe^{3+} ratio is. More chemically interpreted this means that under reducing atmposphere Fe^{3+} transforms to Fe^{2+}.

Only recently, we started detailed experiments investigating the impact of Fe_2O_3 on the structure and dynamics of sodium silicate base melts and glasses. In the follwing paragraphs we will present the first results obtained by neutron time of flight spectroscopy.

We started our investigations on the disilicate join with $2\,Na_2O$-Fe_2O_3-$6\,SiO_2$ (N2FS6) which has a SiO_2 content of 66 mol%. Concerning its SiO_2 content this sample is comparable to the aluminosilicates $3Na_2O$-Al_2O_3-$8SiO_2$ and N_2O-Al_2O_3-$4SiO_2$. We varied the iron oxide content by reducing it by a factor of two in $5Na_2O$-Fe_2O_3-$12SiO_2$ and a factor of four in $11Na_2O$-Fe_2O_3-$24SiO_2$. In addition, $2Na_2O$-Fe_2O_3-$9SiO_2$ that exhibits the same ratio of Na_2O and Fe_2O_3 as N2FS6 and comprises 75 mol% SiO_2 was investigated.

Neutron scattering yields a structure factor of only Fe-Fe correlations in samples comprising mostly Fe^{3+}. Furthermore, a discussion of this structure factor is provided with respect to the total Fe_2O_3 content. Extracting a partial structure factor is only possible in the iron bearing silicates owing to the coupling of spins localised to Fe^{3+}.

6.4.1 Na dynamics and Fe-Fe structure factor

In section 6.3 we observed that adding alumina to binary sodium silicates leads to a disruption of the channel structure for sodium ion transport. This was evidenced by a decrease of the prepeak in the elastic structure factor and a decrease of the sodium diffusivity in the melt. In the binary silicates and in the sodium aluminosilicates we only have access to the elastic structure factor which is the weighted sum of the different partial structure factors. In iron silicates the magnetic scattering gives an additional parameter that allows to access the partial iron structure factor.

The elastic structure factors of iron silicates shown in figure 6.26 were measured using different incident neutron wavelengths. Figure 6.26 illustrates measurements performed on molten and glassy N2FS6. No prepeak emerges between room temperature and 1400 K. Only a rather broad FSDP around 1.6 $Å^{-1}$ is observed. The high temperature data is restricted to smaller momentum transfers. The shift of the FSDP to smaller q values between the glass and the melt reflects the change in the density of the sample. Its height

decreases with the Debye-Waller factor.

However, investigating iron silicates at 2 K additional intensity around the prepeak position is observed in the elastic stucture factor (see figure 6.26. The prepeak was observed to emerge with decreasing temperature below 20 K. Consequently, the measurement was performed at the lowest temperature of the standard ILL orange cryostat. At the smallest accessible q values the intensity is even decreasing compared to the room temperature structure factor.

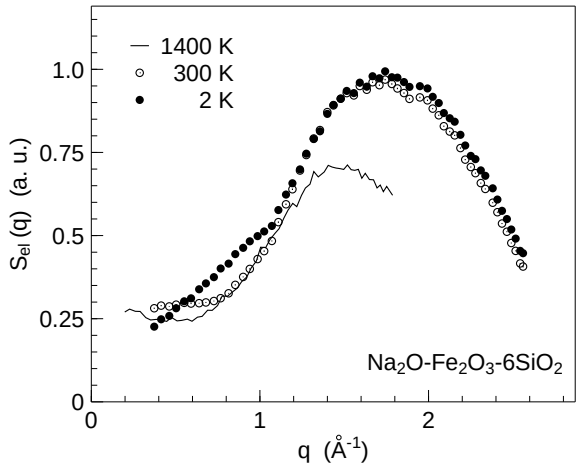

Figure 6.26: Elastic structure factor of N2FS6 measured at IN6 at two different incoming wavelengths: $\lambda = 4.1$ Å indicated by points (•, ○) and $\lambda = 5.9$ Å indicated by the solid line (–). $\lambda = 5.9$ Å was chosen to prevent Bragg scattering on the Pt container. No prepeak is emerging in N2FS6 with increasing temperature in the glassy state. At $T = 2$ K a prepeak becomes visible in the elastic structure factor.

We will comment on the particular scattering properties of iron silicates at low temperatures as it was measured on IN6. For a comparison see figure 6.27.

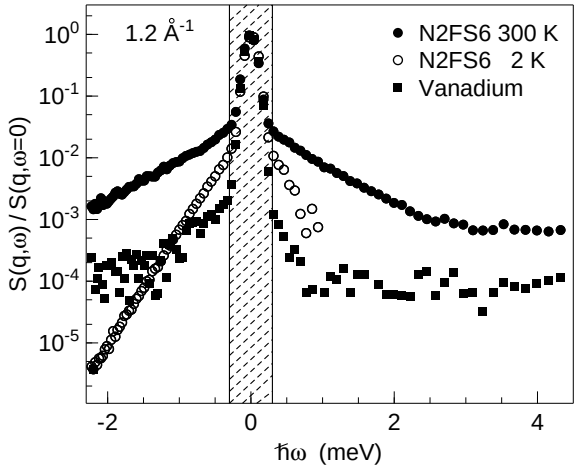

Figure 6.27: $S(q,\omega)$ of N2FS6 at room temperature and at 2 K shown in comparison to the measured instrumental energy resolution function given by Vanadium measured at room temperature. The scattering law is symmetrised by means of the detailed balance factor. For clarity no error bars are shown. The error bars of N2FS6 compare to the symbol size, whereas the error bars of Vanadium close to the background are approximately a quarter of a log unit. $S_{el}(q)$ is calculated by integrating $S(q,\omega)$ over the dashed area.

The scattering law displays a broad diffusive component that arises from magnetic scattering on unpaired iron spins of the Fe^{3+} species. The width of the diffuse magnetic component is unaffected of a temperature change between 40 K and 1400 K that characterises the paramagnetic phase. At 2 K the neutron energy loss side (negative energies) features a decreasing width of the diffuse magnetic component. This indicates a slowing down of the spin fluctuations. Data at 2 K on the energy gain side were cut around the energy transfer of 1 meV, since beyond this energy the instrumental background dominates the signal. On the energy loss side the detailed balance factor suggests a lower

background for the 2 K data leading to an intersection with the Vanadium data.

DC magnetisation of N2FS6 was measured using the physical property measurement system (PPMS, Quantum Design) of the Institute E21 (Physik Department, TU München) for N2FS6. The susceptibility follows a Curie Weiss law at temperatures above $\simeq$ 40 K. Below 40 K deviations of the Curie Weiss (CW) behaviour are observed. A fit of the data in the range of 40 K to 300 K using the CW law $\chi = (Ng^2\mu_B^2 S(S+1))/(3k_B(T-\theta_{cw}))$ yields a negative CW temperature $\theta_{CW} = -14.5 \pm 0.5\,\mathrm{K}$. N denotes the number of magnetic ions in units of the Avogadro constant. We used the gyromagnetic ratio $g = 2$ and the spin quantum number $S = 5/2$ of Fe^{3+}. Moreover, the number of spins were derived to be 0.772 ± 0.005 suggesting that $\simeq$ 77 % of the iron spins contribute to the effective magnetic moment.

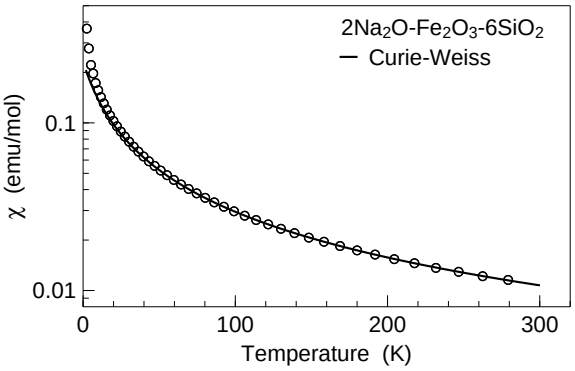

Figure 6.28: Magnetic susceptibility measured with an external magnetic field of 500 Gauß. The solid line represents the Curie Weiss fit to the experimental data (open circles). The susceptibility is shown in units according to the CGS system.

Moreover, we recently started Mößbauer investigations on these samples. Mößbauer spectroscopy enables to determine the ratio of Fe^{2+} to Fe^{3+} in the sample. The oxidation state can be continously varied by varying the atmosphere of synthesis. A Mößbauer spectrum recorded on N2FS6 synthesized under normal atmosphere is shown in figure 6.29.

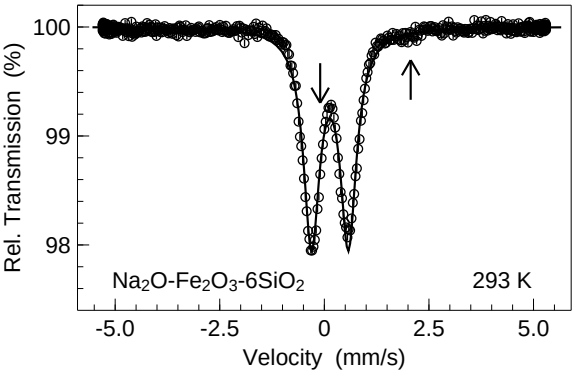

Figure 6.29: Transmission detected by means of Mößbauer spectroscopy in N2FS6 at ambient temperatures. The line represents a fit with a Lorentz doublet. The arrows indicate the positions of the Lorentz doublet lines expected for Fe^{2+}. The latter was derived by means of Mößbauer spectroscopy on a reduced sample. N2FS6 synthesized under ambient condition features no significant amount of Fe^{2+}.

Since we can rule out Fe^{2+} contributions according to the Mößbauer measurement, part of the spins have to be compensated. One can speculate whether this process is achieved by ferromagnetic exchange already at larger temperatures. Such a behaviour is in agreement with the temperature dependence of susceptibility data below 40 K. The behaviour of the susceptibility and its rather strong increase on approaching temperatures around 2 K, which is the lowest accessible temperature in the experiment, suggest

dominant ferromagnetic exchange. However, no completely ordered ferromagnetic phase is reached. The experiments were performed for different magnetic fields (100 Gauß and 500 Gauß). The measured susceptibilities scale with the external magnetic field as expected. A ferrimagnetic behaviour as it is observed for pure Fe_3O_4 cannot completely be ruled out.

The susceptibility explains the observation of a temperature independent diffuse magnetic component in the scattering law. Thus we assumed that diffuse magnetic contributions to the signal are unaffected by a further temperature change to 1400 K in the melt. We analysed the data as follows:
The scattering law separates with respect to nuclear and magnetic contributions

$$S(q,\omega) = S^{nuc}(q,\omega) + S^{mag}(q,\omega)\,. \tag{6.6}$$

The measured $S(q,\omega)$ is convoluted with the instrumental energy resolution $R(q,\omega)$. A simple Fourier deconvolution into the density correlation function does not result in only the nuclear contribution. In order to learn about the Na ion dynamics affected by Fe one can analyse the data based on two assumptions. First, the diffuse magnetic contribution is independent of temperature in the range of 300 K to 1400 K. Moreover, we assume a q dependence of the Fe-Fe spin correlation that is not affected by increasing the temperature from 300 K to 1400 K. Consequently $S(q,\omega)$ transfroms to

$$S_{300K}(q,\omega) = S^{nuc}_{300K} \otimes R(q,\omega) + S^{mag}_{300K}(q,\omega) \otimes R(q,\omega)\,. \tag{6.7}$$

We obtain the measured density correlation function by means of a Fourier transformation to be

$$S_{300K}(q,t) = S^{nuc}_{300K}(q,t) \cdot R(q,t) + S^{mag}_{300K}(q,t) \cdot R(q,t) \tag{6.8}$$

and

$$S_{1400K}(q,t) = S^{nuc}_{1400K}(q,t) \cdot R(q,t) + S^{mag}_{1400K}(q,t) \cdot R(q,t)\,. \tag{6.9}$$

Both mentioned assumptions yields

$$S^{nuc}_{1400K}(q,t) = [S_{1400K}(q,t) - S_{300K}(q,t) + S^{nuc}_{300K}(q)]/R(q,t)\,, \tag{6.10}$$

where $R(q,t)$ is obtained from the room temperature measurement of a sample with equal scattering power containing no magnetic scattering contributions.

Despite of the excellent data quality a detailed analysis of the obtained data is a difficult task, since the nuclear contribution to the scattering signal of the glass is not directly obtained. The 300 K spectra still feature a small decay at short times owing to the Debye-Waller factor. Subtraction of only a constant that represents the elastic structure factor instead of S^{nuc}_{300K} is thus not fully accurate. It will affect the data below about 4 ps that corresponds to energy transfers beyond 0.2 meV.

The density correlation function of the analysed N2FS6 data (see equation (6.10)) is shown in figure 6.30. Despite of the experimental difficulties the data indicates a slowing down of the Na dynamics. Taking into account the absence of a prepeak the data indicates that similarly to the sodium aluminosilicates Na transport is hindered by addition of Fe_2O_3. Adding Fe_2O_3 to a binary sodium silicate the viscosity increases less compared to the addition of Al_2O_3 [DiHe98]. For the tectosilicate composition containing

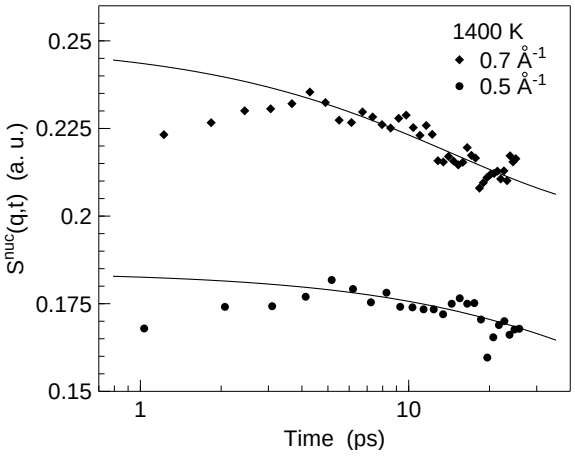

Figure 6.30: Density correlation function of N2FS6 obtained according to equation (6.10). Solid lines are guides to the eye obtained by fitting of a Kohlrausch function in a limited time range of 5 ps to 20 ps with a fixed β and a fixed amplitude a_q of Na relaxation. The latter was estimated based on the amplitude of NS2 similarly to the calculation of aluminosilicates (see table 6.2).

equal amounts of Fe_2O_3 and Na_2O the viscosity at 1600 K is lower by about 2 orders of magnitudes compared to the corresponding aluminosilicate melt [DiVi88]. The effect Fe has on the network structure is less pronounced compared to the effect of adding Al to a binary melt.

6.4.2 Spin dynamics and spin correlations

In contrast to the binary alkali silicates and sodium aluminosilicates our main interest focused on the investigation of the structure and the spin dynamics. We analysed the time of flight data with respect to the diffuse magnetic contribution of the overall scattering signal.

Magnetic scattering arises from scattering of the neutron spin on the spin of an atom. Depending on the electronic configuration it can be purely electron spin scattering or scattering on a moment resulting of spin orbit coupling. Fe^{3+} with the electronic configuration $3d^5$ yields pure spin scattering. The effective gyromagnetic ratio g equals two.

The magnetic scattering amplitude is proportional to the form factor that accounts for the electronic shell of the magnetic ions. We used tabulated values given by P. G. Brown in [Bro99]. The form factor $F(q)$ is approximated by equation

$$F(q) = \langle j_0(q) \rangle + (1 - 2/g)\langle j_2(q) \rangle \,. \tag{6.11}$$

with the spherical Bessel function $j_i(q)$. For spin only scattering $\langle j_2(q) \rangle$ vanishes. In case of $3d$ electronic systems higer order corrections can be neglected. The measured magnetic structure factor has to be divided by the squared form factor $F^2(q) = \langle j_0(q) \rangle^2$.

We derived a magnetic structure factor by subtracting the elastic structure factor measured at 40 K from the structure factor measured at 2 K[4]. We note that already in the elastic structure factor changes in intensity were observed between 300 K and 40 K. However, the effect on the structure factor in this temperature range is dominated by changes in the Debye-Waller factor for nuclear scattering. Performing temperature dependent

[4]The structure factors were obtained by means of integrating the scattering law over the energy resolution represented by the dashed area in figure 6.27.

measurements we revealed in agreement with the susceptibility behaviour a pronounced change in the elastic structure factor below 20 K. The scattering law revealed a slowing down of the spin fluctuations. We note that the elastic stucture factor is deduced by integrating the scattering law over the elastic energy resolution function. Slowing down of the fluctuations leads to increasing intensity in the elastic structure factor. If spin ordering sets in, we expect correlation peaks in the magnetic structure factor reflecting typical distances of structurally arrested spins. Furthermore, nuclear contributions to the elastic structure factor do not change in intensity between 2 K and 40 K. Consequently, the difference reflects only magnetic scattering contributions as shown in figure 6.31. Data are presented for N2FS6, N5FS12, N11FS24 (points) and N2FS9 (solid line).

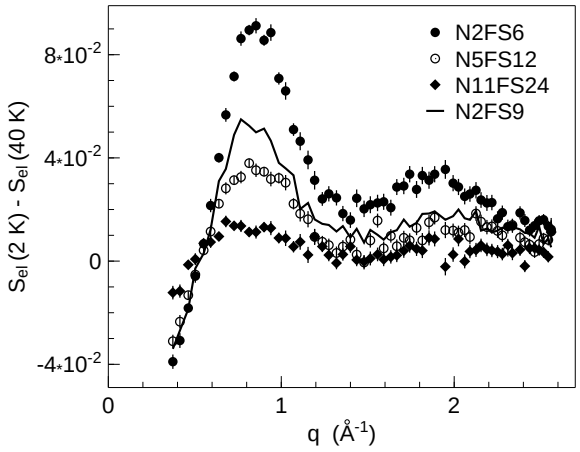

Figure 6.31: Fe-Fe correlation function obtained by subtraction of the elastic structure factors of 40 K and 2 K. Peaks are visible in the difference pattern around 0.9 $Å^{-1}$ and 2 $Å^{-1}$. The magnetic form factor for Fe^{3+} was not taken into account. The position of the peaks remains constant upon decreasing the Fe content by factor of two and four and changing the total SiO_2 content.

The magnetic structure factors feature a peak around 0.9 $Å^{-1}$ at the position of the prepeak in the binary sodium silicates. The peak position is unchanged upon decreasing the Na content by a factor of two (N5FS12) and four (N11FS24). The intensity of the peak decreases with decreasing number of Fe^{3+} atoms. It does not exactely scale with the ratio of the total iron amount. In N2FS9 the peak position is equivalent to that of N2FS6 despite changes in the total amount of SiO_2.

A first measurement at the D7 diffractometer at ILL that allows for measurments using polarisation analysis directly revealed the magnetic structure factor. 2 K data are shown in figure 6.32. Pronounced oscillations in the magnetic structure factor are only observed below 20 K. Above this temperature the magnetic structure factor compares to an incoherent nuclear structure factor (not shown) featuring no oscillations in q. The measured magnetic structure factor decreases with increasing wavenumber with the form factor. The displayed data are already corrected for the form factor.

As for the IN6 experiment we revealed during the D7 experiments a magnetic correlation peak around 0.9 $Å^{-1}$. Statistical data quality is worse due to lower neutron intensity. Moreover, we note that multiple scattering is certainly not negligible due to the rather large scattering power of the sample. This typically contributes a large relatively q independent background and might also be responsible for some artifacts on the structure factor. The observed peak around 0.9 $Å^{-1}$ is broader compared to the IN6 data. This results from the fact that D7 exhibits an elastic energy resolution in the range of some meV. We effectively probe different timescales of the spin fluctuations compared to IN6

that offers a resolution in the range of 200 μeV (FWHM). Thus on IN6 we probe with high accuracy spin fluctuations which are already slower than 10 ps, whereas D7 probes the whole magnetic contribution to the scattering signal.

Obviously, data treatment of the time of flight experiment in terms of deducing the magnetic correlations seems reasonable. It provides better statistics than the D7 experiment using polarisation analysis. However, the latter was inevitable to justify the analysis of the time of flight data.

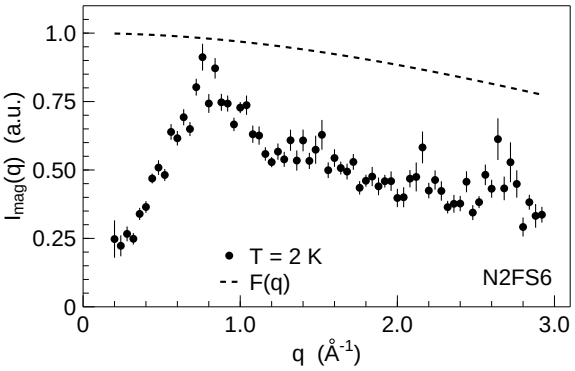

Figure 6.32: Magnetic scattering intensity obtained by polarized neutron diffraction at D7. The spectrum was obtained at 2 K. The experimental data was divided by the magnetic form factor $F(q)$ for Fe^{3+} calculated according to P. G. Brown [Bro99]. At 0.9 Å^{-1} a correlation peak is observed.

A first sample was prepared under reducing (CO, CO+CO_2) atmosphere. A test measurement of this reduced N2FS6 sample on the IN6 spectrometer revealed the diffuse magnetic contribution to be decreasing with increasing Fe^{2+} content. An accurate description of the decrease in amplitude was not obtained, since the sample that was prepared by P. Courtial, Institute of Mineralogy, Petrology and Geochemistry at the LMU, was inhomogeneous and featured a not well defined oxidation state. Nevertheless the correlation in the structure factor originating from the remaining Fe^{3+} contribution shows up at similar position compared to the fully oxidized N2FS6 sample.

Our investigations on iron bearing sodium silicate glasses clearly revealed a partial Fe-Fe structure factor by means of magnetic scattering on the electron spin attached to Fe^{3+}. In comparison to the partial structure factors of the MD simulations on NS2 the Fe-Fe structure factor also features a peak around 0.9 Å^{-1} attributed to intermediate range order and channel formation in NS2. Reducing the total iron concentration by a factor of two and four only changes the amplitude and not the position of this peak. This is clearly an indication for an inhomogeneous distribution of the Fe atoms in channels and not in clusters embedded in the SiO matrix in the sodium ironsilicates. This is further corroborated by a sample in which the total SiO_2 content was changed from 66 mol% to 75 mol%. This sample also revealed the peak position unchanged. The latter is similar to the observation in binary silicate melts. In NS2, NS3, and NS4 the prepeak position is the same independent on the total Na content.

Chapter 7

Outlook

7.1 Neutron resonant spin echo on sodium disilicate

The neutron spin echo technique first proposed by Mezei [Mez80] relies on the property of the neutron spin that can act as an intrinsic clock to measure small energy transfers to the neutron during scattering. The latter are typically in the range of several 100 neV to a few μeV. The following explanation shall only briefly comment on the basic concepts of this scattering technique without providing further details. As earlier discussed a neutron bears a magnetic moment that can interact with external magnetic field. In an unpolarized neutron beam the magnetic moments of the neutrons are randomly oriented. A particular polarisation direction, i. e. a defined orientation of all neutron magnetic moments, is achieved via inserting devices like e. g. supermirrors in the beam. Effectively, neutrons with only one spin state are transmitted. Out of the white beam neutrons with an energy resolution $\delta E/E$ of up to 5% to 20% are typically chosen by a velocity selector. The polarisation of the neutron beam is flipped perpendicular to the magnetic field before entering the magnetic coils of the spectrometer. The neutron spin undergoes Larmor precession around the magnetic field vector. The number of the Larmor precessions of a particular neutron spin depends on the time the neutron experiences the magnetic field. Therefore it is related to the neutron velocity. The spins are flipped by 180° before the sample position effectively corresponding to time reversal. After scattering on the sample the neutrons fly through a second coil. They experience a magnetic field of similar magnitude and orientation evoked by a this magnetic coil of similar length compared to the first one. In case of purely elastic coherent scattering the polarisation is restored. The polarisation of the scattered beam is analysed by means of a second insertion device, e. g. a supermirror. The transmitted neutrons are detected in a two dimensional detector covering a certain angular range.

The measured quantity during an experiment is the polarisation of the neutron beam. Based on the latter the density correlation function can be directly inferred.

The neutron spin echo technique allows for investigation of processes on timescales up to almost microseconds. The energy resolution varies with scattering angle. The best resolution that yields the largest accessible timescales is only available at sufficiently small momentum transfers. Which is well below 0.5 Å^{-1}. Thus it is achieved in a range that is dominated by incoherent scattering on Na. In the sodium silicates we are interested in

momentum transfers of the order of 1 $Å^{-1}$ or above. At these intermediate wavenumbers relevant for the measurements of oxidic melts the resolution only allows for investigation of processes on a maximal timescale of 10 ns.

Incoherent scattering and magnetic stray fields disturb the signal leading to a reduction of the neutron beam polarisation. Thus only coherent scattering processes are suited to be analysed by a conventional neutron spin echo instrument. In high temperature experiments using a furnace stray fields of the heating elements may play a significant role. Special designed heating elements have to be used for annihilation of magnetic fields that are generated by the current through it. Such a device was already successfully used in experiments at the zero field spin echo spectrometer at LLB, Paris. The latter makes use of the quantum mechanical description of the spin echo technique [GaGH96]. A lower spin polarisation due to incoherent scattering and stray fields can be partly overcome with the zero field technique [HaBG97]. A furnace is already designed for the RESEDA instrument at FRM-II. Beam time was granted to an approved proposal. A first experiment will be performed most probably within one of the next cycles when the instrument is in full operation.

The spin echo measurements shall provide an answer to the question of the decay of the coherent correlators at large momentum transfers. Especially the splitting of coherent Na-Na from the other coherent correlators shall be probed. The separation is predicted by MD simulations to be of up to 1.5 orders of magnitude [HoKB02].

7.2 Dynamic light scattering

In the following paragraph a short outlook on depolarized light scattering measurements on sodium borate samples is presented. First measurements were performed on sodium diborate, tetraborate and ikosaborate. Detailed investigations of oxidic melts by means of dynamic light scattering are subject of a recently started PhD thesis work. Thus only a short outline towards what can be learned from a comparison of dynamics light scattering and inelastic neutron scattering data is provided. It includes a short discussion of the experimental difficulties to measure liquids at high temperatures. The latter were overcome by specially designed furnace.

That a comparison of incoherent neutron scattering data and the susceptibility measured by means of depolarized light scattering gives further insight into the origin of relaxation processes was already shown for a number of molecular glass formers [WuHL94, WuSH98]. Respecting the scattering process the main difference is given by the fact that neutron scattering directly couples to the core of the nuclei, whereas light couples to the fluctuations in the dielectric tensor. The latter turn the analysis of the data in terms of the identification of the process underlying the scattering of the light into a complicated task. The lengthscales which are investigated correspond to the lengthscales of the fluctuations in the dielectric tensor and are thus comparable to the hydrodynamic limes of small wavenumbers. However, the lengthscales do not correspond to the much larger lengthscales suggested by simply taking the dispersion relation of photons. Compared to dynamics light scattering neutron scattering measures the susceptibility over a large

momentum transfer range. In typical neutron scattering experiments the hydrodynamic limes is only approximately reached for small wavenumbers. We expect to gain further insight from a comparison of depolarized light scattering and neutron data. In neutron scattering the additional information arising from the dependence of relaxation processes on the momentum transfer can be used to identify their origin. Depolarized dynamic light scattering covers up to four orders of magnitude in frequency (0.2 GHz – 2 Thz), whereas neutron scattering at best allows for a dynamical range of three orders of magnitude in time. The latter range is obtained by combining time of flight spectroscopy and neutron backscattering data.

First inelastic light scattering experiments were performed on the multipass Sandercock Tandem Fabry-Perot interferometer at the Institute E13. For the light scattering investigations an Argon ion laser providing an incident wavelength of 514.5 nm was used. Details of the instrument and discussions about its setup can be found in [Gol01]. During the experiments on oxidic melts a wire loop furnace - the details are explained in the last paragraph of this section - was used. The measurements were performed in the backscattering geometry with crossed polarisation for the incident and scattered beam. The scattered light is collected by a lens focussing on the secondary spectrometer. The Fabry-Perot principle is used for measuring energy transfers in the sub-μeV to meV range.

The Raman experiments were also performed at the Institute E13 using a Jobin-Yvon U1000 spectrometer. The energy transfer to the incoming light when scattering on the sample is measured by interference of the scattered light on a optical grating. The Raman measurements were mostly used to allow for normalisation of the Fabry-Perot data by extending the energy transfer range in the THz region. Raman scattering allows for measurements on an absolute scale. Thus the data at different temperatures can directly be compared. To compare directly the evolution of the α relaxation a normalisation to the Boson peak that occurs in these melts in the range of a few THz is used for convenience following the approach presented in [BrBE96].

For these measurements the crucial point was to find a suitable sample geometry and environment. For the inelastic light scattering measurements a multipurpose furnace was built up together with Josef Kaplonski and Cornelius Strohm (Physik Department E13). The furnace can be operated up to 1400 °C. It consists of a Pt-5%Rh heater embedded in a Al_2O_3–SiO_2 heat shield surrounded by a water cooled Al box. The sample chamber is made of a thin walled Al_2O_3 tube. A Pt wire is used as sample holder. Typical sample geometries are droplets or thin films with a diameter of about 2 mm. The temperature is constant over a horizontal area of about 2 - 3 cm in the furnace. For the measurements the furnace is horizontally operated under air. In order to avoid contamination of the signal by radiation of the furnace a infrared filter is used as entrance window. The filter also prevents from cooling due to circulating air. Additionally, the lens focussing the laser beam on the sample and collecting the scattered light can be closely put to the furnace. A future prospect to obtain an accurate temperature calibration is to build up a differential calorimeter setup for this wire loop furnace. The main advantage is that reflection of the direct beam or multiple scattering due to the reflection of the direct beam

on a sample holder wall is avoided. First measurements that revealed the temperature dependence of the α relaxation peak suggest that dynamic light scattering only measures the contributions of the B-O network.

The furnace was also successfully used in first nuclear resonant scattering experiments of synchrotron radiation at the ESRF on Fe^{57} in iron bearing silicate melts. In this context the furnace allows not only for operation under air, but also for operation under reducing or inert atmosphere. The latter is particularly important for investigations of iron bearing silicates samples. Moreover, the furnace was designed to allow for scattering under 90°. Hence, transverse sound velocities shall be measured. Furthermore, the SRPAC technique on the Fe^{57} isotope can be employed to measure iron diffusion.

Appendix A

Neutron scattering cross sections

The following table contains the incoherent (σ_i) and coherent (σ_c) neutron scattering cross sections for bound nuclei taken from reference [RaWa00]. The absorption cross section is noted for a incoming wavelength of $\simeq 1.8$ Å. Only data for nuclei used in our experiments are shown.

Atom	σ_i	σ_c	σ_a
^{7}Li	0.78(3)	0.619(11)	0.0454(3)
Na	1.62(3)	1.66(2)	0.530(5)
K	0.27(11)	1.69(2)	2.1(1)
^{11}B	0.21(7)	5.56(7)	0.0055(33)
O	0.000(8)	4.232(6)	0.00019(2)
Si	0.004(8)	2.1633(10)	0.171(3)
Al	0.0082(6)	1.495(4)	0.231(3)
Fe	0.40(11)	11.22(5)	2.56(3)
Pt	0.13(11)	11.58(2)	10.3(3)

Table A.1: Neutron scattering cross sections for selected elements. The data are given in units of barn corresponding to $10^{-24}\,\mathrm{cm}^2$.

It has to be pointed out that the incoherent cross sections of the alkali atoms Na, Li and K behave approximately with 6:3:1. The latter is crucial for the discussion of the density correlation functions of the binary alkali silicates presented in section 6.1.

Appendix B

Setups of the neutron scattering instruments

Neutron time of flight spectroscopy and neutron backscattering were performed at ILL and at the NCNR at NIST, respectively. The setups are shown in the following table.

Instrument	Type	Inc. wavelength λ [Å]	FWHM [μeV]	q [Å^{-1}]
IN5	disk chopper TOF	8.0	33 - 40	0.2 - 1.4
IN6	crystal TOF	4.1	170	0.35 - 2.6
		5.1	70	0.25 - 2.1
		5.9	50	0.20 - 1.8
DCS	disk chopper TOF	5.1	100	0.28 - 2.26
HFBS	backscattering	6.271	1.1	0.25 - 1.75

Table B.1: The table lists the instrument type and the incoming neutron wavelengths used for the experiments. Moreover, the corresponding resolution and the accessible wavenumber range are presented.

The time of flight experiments were mostly performed on IN6 using the 5.9 Å^{-1} setup. For the experiment on IN5 it has to be noted that the radial collimator was not in place. Hence, errors imposed on the data were not negligible in the momentum transfer and energy range of interest. On the DCS instrument (NIST) the incoming neutron flux at 5.1 Å is by a factor of 10 to 15 less compared to IN6 at approximately similar background level. Owing to the lack neutron intensity the density correlation function obtained from these measurements can only provide a basis for future approaches.

Appendix C

Publications of the author

I thank the Fakultät für Physik to meet with kind approval the publication of the following articles on the subject.

F. Kargl, A. Meyer, M. M. Koza, *Structure on intermediate range in* $(Na_2O)_{1-x}$–$(K_2O)_x$–$(SiO_2)_y$ *melts*, (to be published).

F. Kargl, A. Meyer, M. M. Koza, *Na* β*-relaxation prepares ion transport in* $Na_2O - 2B_2O_3$, (to be published).

F. Kargl, A. Meyer, M. M. Koza, H. Schober, *Alkali silicate melts: Formation of Channels for Fast Ion Diffusion*, (submitted).

F. Kargl, A. Meyer, *Inelastic neutron scattering on sodium aluminosilicate melts: sodium diffusion and intermediate range order*, Chem. Geol. **213**, (2004) 165.

A. Meyer, J. Horbach, W. Kob, F. Kargl, H. Schober, *Channel formation and intermediate range order in sodium silicate melts and glasses*, Phys. Rev. Lett. **93**, (2004) 027801.

Acknowledgment

I thank everybody who directly and indirectly contributed to this thesis work. In this sense I wish to express my gratitude to

- Prof. Andreas Meyer who offered me the possibility to scientifically work under his supervision. Moreover, he introduced me to this very exciting field of physics and continuously supported me during my time at the institute E13.
- Prof. Winfried Petry for giving my the opportunity to join his institute for my diploma and PhD thesis.
- Dr. Jürgen Horbach and Prof. Walter Kob for the stimulation scientific discussion on the MD simulations. I thank also for providing various figures of their simulation work.
- Dr. Marek Koza who competently and skilfully assisted all neutron scattering experiments on IN6 at the Institute Laue-Langevin. He also offered experimental time of the instrument without allocation. In particular, he contributed in this way to the investigation of borates and iron bearing silicates.
- Dr. Dan Neumann of the NIST in Gaithersburg who offered the possibility of a half year scientific exchange to the NCNR. Only this enabled neutron backscattering experiments on a number of different samples.
- Dr. Helmut Schober who joined as local contact our IN5 experiment at the Institute Laue-Langevin. I also thank him for fruitful discussions on iron bearing silicates.
- Josef Kaplonski who actively supported the installation and the maintenance of the synthesis furnaces at E13.
- Dr. Cornelius Strohm who crucially contributed besides Josef Kaplonski to the construction of the furnace of the light scattering instrument.
- Mr. Putzer, Mr. Funer and Mr. Dörbecker of the E13 mechanical workshop who accurately performed all work for sample holders and the sample environment of neutron scattering experiments.
- all PhD students and postdoctoral research fellows of E13 who welcomed me at the institute and permanently offered an agreeable working atmosphere.
- my family, in particular my wife and my parents, who continuously supported my education and my research work performed in the last years.

Bibliography

[AnCT82] C. A. Angell, P. A. Cheeseman, S. Tamaddon, J. Phys. C9 **43**, (1982) 381.

[Ang92] C. A. Angell, in *Slow dynamics in condensed matter*, edts. K. Kawasaki, T. Kawakatsu, M. Tokuyama, (1992), AIP Conf. Proc. No. 256).

[BaPP00] A. V. Baranov, T. S. Perova, V. I. Petrov, K. K. Vij, O. F. Nielsen, J. Ram. Spec. **31**, (2000) 819.

[BeGS84] U. Bengtzelius, W. Götze, A. Sjölander, J. Phys. C **17**, (1984) 5915.

[BoDR01] Y. Bottinga, D. B. Dingwell, P. Richet, edts., *6th Silicate Melt Workshop*, Chem. Geol. **174**, (2001) 1-376.

[BoDR04] Y. Bottinga, D. B. Dingwell, P. Richet, M. Toplis, edts., *7th Silicate Melt Workshop*, Chem. Geol. **213**, (2004) 1-291.

[BoTa87] J. Bosse, J. S. Thakur, Phys. Rev. Lett. **59**, (1987) 998.

[BoYi91] J. P. Boon, S. Yip, *Molecular Hydrodynamics*, 1991 (reprint), Dover.

[BrBE96] A. Brodin, L. Börjesson, D. Engberg, L. M. Torell, Phys. Rev. B **53**, (1996) 11511.

[BrFr88] M. Braedt, G. H. Frischat, Phys. Chem. Glasses **29**, (1988) 214.

[Bro99] P. G. Brown in *International Tables of Crystallography: Volume C*, edt. by A. J. C. Wilson and E. Prince, Alden Press, Oxford 1999, 450.

[Bur00] D. J. M. Burkhard, J. Non-Cryst. Sol. **275**, (2000) 175 (and references herein).

[CoLo75] J. R. D. Copley, S. W. Lovesey, Rep. Prog. Phys. **38**, (1975) 461.

[DiHe98] D. B. Dingwell, K.-U. Hess, Am. Mineral. **83**, (1998) 1016.

[Din96] D. B. Dingwell, Science **273**, (1996) 1054.

[DiVi88] D. B. Dingwell, D. Virgo, Geochim. Cosmochim. Acta **52**, (1988) 395.

[Ege92] P. A. Egelstaff, *An introduction to the liquid state*, Oxford University Press 1992.

[Ell91] S. R. Elliot, Phys. Rev. Lett. **64**, (1991) 711.

[EnWB98] D. Engberg, A. Wischnewski, U. Buchenau, L. Börjesson, A. J. Dianoux, A. P. Sokolov, L. M. Torell, Phys. Rev. B **58**, (1998) 9087.

[Fuc94] M. Fuchs, J. Non-Cryst. Sol. **172**, (1994) 241.

[FuHo90] K. Funke, R. Hoppe, Sol. St. Ion. **40**, (1990) 200.

[FuRL98] K. Funke, B. Roling, M. Lange, Solid State Ionics **105**, (1998) 195.

[GaGH96] R. Gähler, R. Golub, K. Hubert, T. Keller, J. Felber, Physica A **229**, (1996) 1.

[GeSt97] A. M. George, J. F. Stebbins, Sol. St. Nuc. Mag. Res. **10**, (1997) 9.

[Gol01] M. Goldammer, Physik Department E13, Technische Universität München, PhD thesis 2001.

[Got90a] W. Götze, J. Phys.: Condens. Matter **2**, (1990) 8485-8489.

[Got90b] W. Götze, J. Phys.: Condens. Matter **2**, (1990) SA201-SA205.

[Got91] W. Götze, in *Liquids, Freezing and the Glass Transition*, edts. J. P. Hansen, D. Levesque, and D. Zinn-Justin, Les Houches,session LI, 1991, North Holland, Amsterdam.

[Got92] W. Götze, L. Sjögren, Rep. Prog. Phys. **55**, (1992) 241.

[Got99] W. Götze, J. Phys.: Condens. Matter **11**, (1999) A1.

[Gre85] G. N. Greaves, J. Non-Cryst. Sol. **71**, (1985) 203.

[GuKi67] Y. P. Gupta, T. B. King, Trans. Met. Soc. AIME **239**, (1967) 1701.

[HaBG97] P. Hanks, W. Besenbock, R. Gähler, M. Koppe, Physica B **234**, (1997) 1130.

[HaKK99] K. Handa, Y. Kita, S. Kohara et. al., J. Phys. Chem. Sol. **60**, (1999) 1465.

[HeDi96] K.-U. Hess, D. B. Dingwell, Am. Mineral. **81**,(1996) 1297.

[HoKB02] J. Horbach, W. Kob, K. Binder, Phys. Rev. Lett. **88**, (2002) 125502.

[HoKo02] J. Horbach, W. Kob, J. Phys.:Condens. Matt. **14**, (2002) 9237.

[HoKo99] J. Horbach, W. Kob, Phil. Mag. B **79**, (1999) 1981.

[Hov54] L. v. Hove, Phys. Rev. **95**, (1954) 249-262.

[Hun99] A. G. Hunt, J. Non-Cryst. Sol. **255**, (1999) 47.

[ImVM02] A. W. Imre, S. Voss, H. Mehrer, Phys. Chem. Chem. Phys. **4**, (2002) 3219.

[InMY93] Y. Inagaki, H. Maekawa, T. Yokokawa, Phys. Rev. B **47**, (1993) 674.

[JoBB51] J. R. Johnson, R. H. Bristow, H. H. Blau, J. Am. Ceram. Soc. **34**, (1951) 165.

[JuKJ01] P. Jund, W. Kob, R. Jullien, Phys. Rev. B **64**, (2001) 134303.

[JuKJ02] P. Jund, W. Kob, R. Jullien, Phil. Mag. B **82**, (2002) 597.

[KaMe04] F. Kargl, A. Meyer, Chem. Geol. **213**, (2004) 165.

[Kar02] F. Kargl, Physik Department E13, Technische Universität München, Diploma thesis 2002.

[Kie99] J. Kieffer, J. Non-Cryst. Sol. **255**, (1999) 56.

[KiMR95] J. Kieffer, J. E. Masnik, B. J. Reardon, J. D. Bass, J. Non-Cryst. Sol. **183**, (1995) 51.

[KnDS94] R. Knoche, D. B. Dingwell, F. A. Seifert, S. L. Webb, Chem. Geol. **116**, (1994) 1.

[Kob99] W. Kob, J. Phys.:Condens. Matter **11**, (1999) R85.

[Kra05] V. Krakoviack, Phys. Rev. Lett. **94**, (2005) 065703.

[Lac63] E. D. Lacy, Phys. Chem. Glasses **4**, (1963) 234.

[LaKH03] H. Lammert, M. Kunow, A. Heuer, Phys. Rev. Lett. **90**, (2003) 215901.

[Maa99] P. Maass, J. Non-Cryst. Sol. **255**, (1999) 35.

[MaCC03] O. Majérus, L. Cormier, G. Calas, B. Beuneu, Phys. Rev. B **67**, (2003) 024210.

[MaCC04] O. Majérus, L. Cormier, G. Calas, B. Beuneu, Chem. Geol. **213**, (2004) 89.

[MaMK04] S. Mavila Chathoth, A. Meyer, M. M. Koza, F. Juranyi, Appl. Phys. Lett. **85**, (2004) 4881.

[MaMK91] H. Maekawa, T. Maekawa, K. Kawamura, T. Yokokawa, J. Non-Cryst. Sol. **127**, (1991) 53.

[MaNC04] V. Magnien, D: R. Neuville, L. Cormier, B. O. Mysen, V. Briois, S. Belin, O. Pinet, P. Richet, Chem. Geol. **213**, (2004) 253.

[MaSS83] O. V. Mazurin, M. V. Streltsina, T. P. Shvaiko-Shvaikovskaya, *Handbook of Glass Data: Part A, silica glass and binary silicate glasses*, 1983, Elsevier.

[MaSS85] O. V. Mazurin, M. V. Streltsina, T. P. Shvaiko-Shvaikovskaya, *Handbook of Glass Data: Part B, single-component and binary non-silicate oxide glasses*, 1985, Elsevier.

[MeDG03] A. Meyer, R. M. Dimeo, P. M. Gehring, D. A. Neumann, Rev. Sci. Instr. **74**, (2003) 2759.

[MeDS02] A. Meyer, D. B. Dingwell, H. Schober, Europhys. Lett. **59**, (2002) 708.

[MeHK04] A. Meyer, J. Horbach, W. Kob, F. Kargl, H. Schober, Phys. Rev. Lett. **93**, (2004) 027801.

[Mey02] A. Meyer, Phys. Rev. B **66**, (2002) 134205.

[Mez80] F. Mezei, ed., *Neutron Spin Echo*, Lecture Notes in Physics Vol. 128, 1980, Springer.

[MiPS80] M. Misawa, D. L. Price, K. Suzuki, J. Non-Cryst. Sol. **37**, (1980) 85.

[Mul03] A. Müller, Physik Department E13, Technische Universität München, Diploma thesis 2003.

[OiTU75] Y. Oishi, R. Terai, H. Ueda, in *Mat. Sci. Res.: Mass Transport Phenomena in Ceramics* , edts. , (1975).

[OvSa98] J. Oviedo, J. F. Sanz, Phys. Rev. B **58**, (1998) 9047.

[PaPi62] H. H. Paalman, C. J. Pings, J. Appl. Phys. **33**, (1962) 2635.

[Poh05] M. Pöhlmann, Physik Department E13, Technische Universität München, PhD thesis, 2005.

[PrCa87] D. L. Price, J. M. Carpenter, J. Non-Cryst. Sol. **92**, (1987) 153.

[RaJE98] E. Ratai, M. Janssen, H. Eckert, Sol. St. Ionics **105**, (1998) 25.

[RaWa00] H. Rauch, W. Waschkowski, *Landolt-Börnstein* **16A**, Chapt. 6, Springer, Berlin, 2000.

[RiBl94] R. Richert and A. Blumen, *Disorder effects on relaxational processes*, 1994, Springer.

[RiDP88] *Dynamics of Disordered Materials*, edts. D. Richter, A. J. Dinaoux, W. Petry, and J. Teixeira, 1988, Springer, Heidelberg.

[Rie66] E. F. Riebling, J. Chem. Phys. **44**, (1966) 2857.

[RoPM01] C. Romano, B. Poe, V. Mincione, K.-U. Hess, D. B. Dingwell, Chem. Geol. **174**, (2001) 115.

[ScMe00] U. Schoo, H. Mehrer, Sol. St. Ion. **130**, (2000) 243.

[SeSt97] S. Sen, J. F. Stebbins, Phys. Rev. B **55**, (1997) 3512.

[Sjo58] A. Sjölander, Arkiv för Fysik **13**, (1958) 315.

[SkRO72] K. Sköld, J. M. Rowe, G. Ostrowski, P. D. Randolph, Phys. Rev. A **6**, (1972) 1107.

[Squ96] G. L. Squires, *Introduction to the theory of thermal neutron scattering*, 1996 (reprint), Dover.

[StHI01] C. E. Stone, A. C. Hannon, T. Ishihara, N. Kitamura, Y. Shirakawa, R. N. Sinclair, N. Umesaki, A. C. Wright, J. Non-Cryst. Sol. **293**, (2001) 769.

[StMD95] J. F. Stebbins, P. F. McMillan, D. B. Dingwell, edts., *Structure, Dynamics and Properties of Silicate Melts*, Reviews in Mineralogy Vol. 32, 1995, Mineral. Soc. of Am. .

[SwAd03] J. Swenson, S. Adams, Phys. Rev. Lett. **90**, (2003) 155507.

[SwBH98] J. Swenson, L. Börjesson, W. S. Howells, Phys. Rev. B **57**, (1998) 13514.

[SwBo98] J. Swenson, L. Borjesson, J. Non-Cryst. Solids **223**, (1998) 223.

[SwMK01] J. Swenson, A. Matic, C. Karlsson, L. Börjesson, C. Meneghini, W. S. Howells, Phys. Rev. B **63**, (2001) 132202.

[Tic67] R. E. Tickle, Phys. Chem. Glasses **8**, (1967) 101.

[ToDH97] M. Toplis, D. B. Dingwell, K.-U. Hess, T. Lenci, Am. Mineral. **82**, (1997) 979.

[ToDL97] M. Toplis, D. B. Dingwell, T. Lenci, Geochim. Cosmochim. Acta **61**, (1997) 2605.

[Tol01] A. Tölle, Rep. Prog. Phys. **64**, (2001) 1473.

[vBKS90] B. W. van Beest, G. J. Kramer, R. A. van Santen, Phys. Rev. Lett. **64**, (1990) 1955.

[VoDi80] F. Volino, A. J. Dianoux, Mol. Phys. **41**, (1980) 271.

[VoHo05] Th. Voigtmann, J. Horbach, cond-mat. 0508379.

[WaBi38] B. E. Warren, J. Biscoe, J. Am. Ceram. Soc. **21**, (1938) 259.

[WaSu77] Y. Waseda, H. Suito, Trans. ISIJ **17**, (1977) 82.

[Web05] S. Webb, Eur. J. Min. **17**, (2005) 223.

[Wie03] S. Wiebel, Physik Department E13, Technische Universität München, PhD thesis 2003.

[WrFH96] A. C. Wright, S. A. Feller, A. C. Hannon, *Borate glasses, crystals & melts*, 1996, Society of Glass Technology, Alden Press.

[Wri97] A. C. Wright, Glass Phys. Chem. **24**, (1998) 148.

[WuCR96] J. Wuttke, I. Chang, O. G. Randl, F. Fujara, Phys. Rev. E **54**, (1996) 5364.

[WuHL94] J. Wuttke, J. Hernandez, G. Li, G. Coddens, H. Z. Cummins, F. Fujara, W. Petry, and H. Sillescu, Phys. Rev. Lett. **72**, (1994) 3052.

[WuPC95] J. Wuttke, W. Petry, G. Coddens, F. Fujara, Phys. Rev. E **52**, (1995) 4026.

[WuSH98] J. Wuttke, M. Seidl, G. Hinze, A. Tölle, W. Petry, G. Coddens, Eur. Phys. J. B **1**, (1998) 169.

[Wut00] J. Wuttke, Phys. Rev. E **67**, (2000) 6531.

[ZaBC99] J.-M. Zanotti, M.-C. Bellissent-Funel, S. H. Chen, Phys. Rev. E **59**, (1999) 3084.

[Zac31] W. H. Zachariasen, J. Am. Ceram. Soc. **54**, (1931) 3841.

[ZhSv03] V. A. Zhabrev, S. I. Sviridov, Glass Phys. Chem. **29**, (2003) 140.